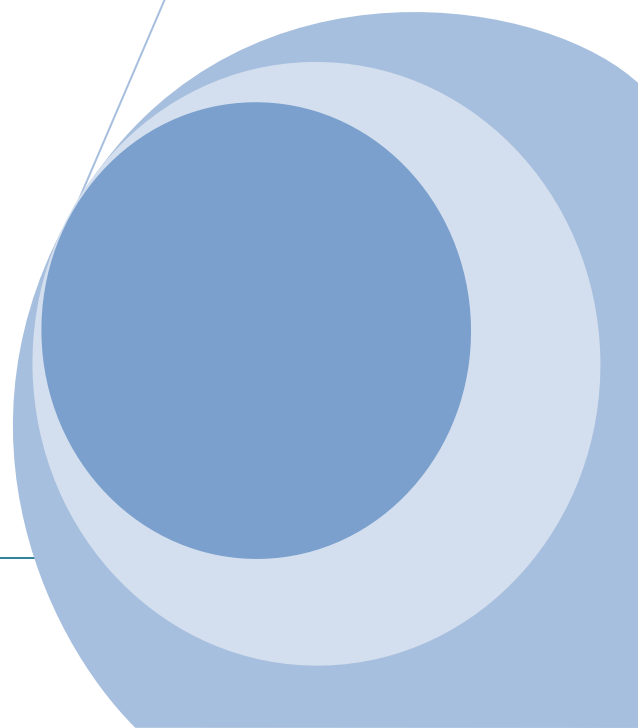
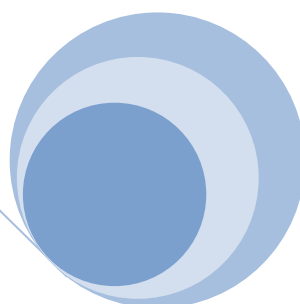
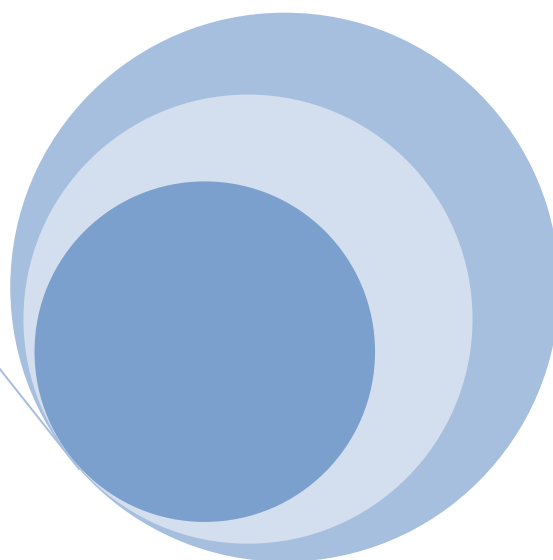




International Journal of Current Science Research

www.drbgrpublications.in



IJCSR

International Journal

Impact Factor: GIF – 0.676

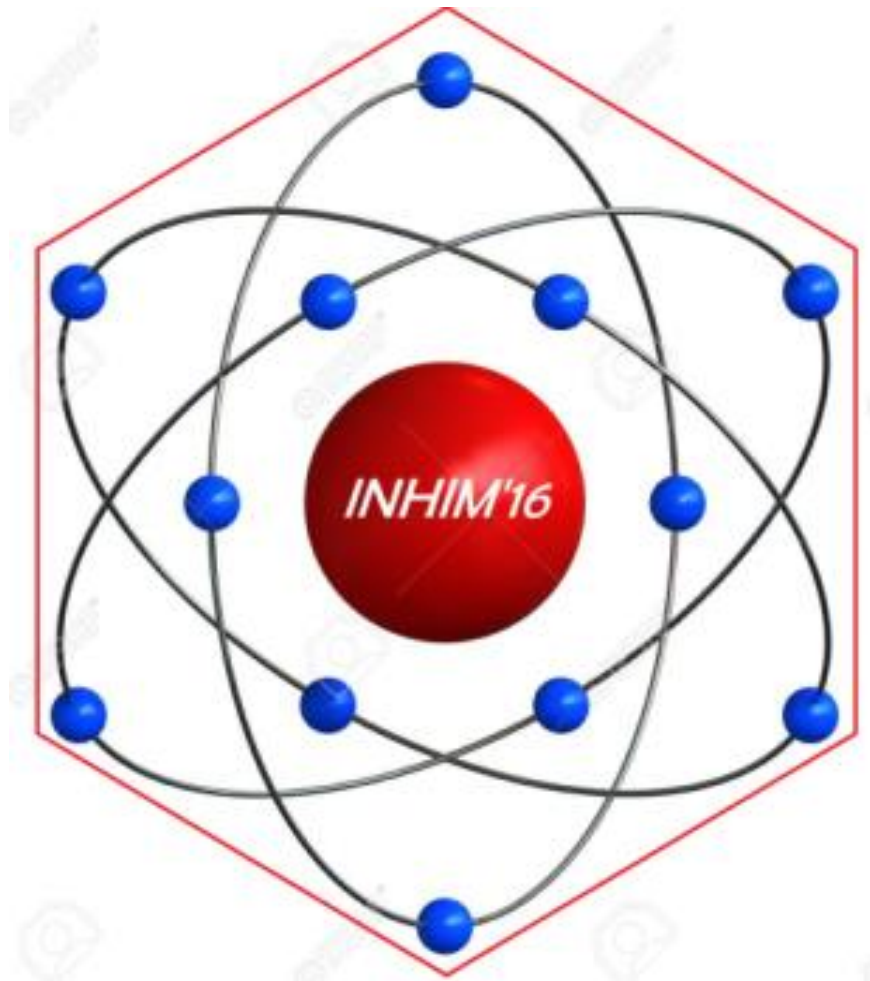
Indexed over 23 databases.

Dr.BGR Publications


3/30/2016

Volume 2; Issue 3 [Special Issue] 2016

IJCSR



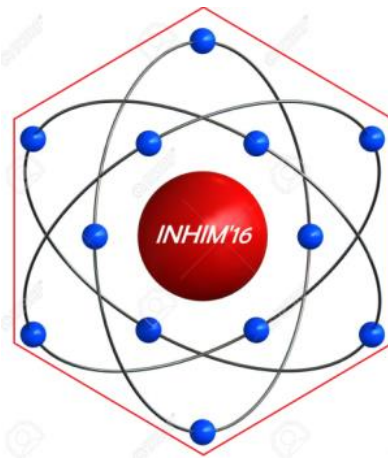
Available at: <http://www.drbgpublications.in/ijcsr.php>

Special Issue on INHIM'16  Sarah Tucker College (Autonomous), Tirunelveli.

International Conference on A New Horizon in Materials

Date

11th March, 2016



Organized by
Department of Physics



Sarah Tucker College (Autonomous), Tamilnadu, India

About Sarah Tucker College (Autonomous), Tamilnadu, India

Sarah Tucker College, founded in 1895 enjoys a heritage of 120 years as a Christian minority institution of higher education for women. It functions under the management of the Tirunelveli Diocesan Trust Association affiliated to Manonmaniam Sundaranar University. The motto of the college is "So run that ye may obtain the incorruptible crown". The mission is 'Service Through Knowledge'. The college strives towards excellence through earnest academic pursuit and aims at creative and empathetic involvement in the society. It seeks to serve along with the holistic development of its inmates. The high academic standards and its reputation were acknowledged by the NAAC and reaccredited 'with A' Grade in 5th January 2013.

About the Physics Department

Physics was introduced as a core subject at the Undergraduate level in 1968 and elevated to the Postgraduate level in 1979. Ever since its inception, the Department has been a pioneer in laying stress on teaching, in service education, interdisciplinary activities and carrier counseling. The Department is notified for its consistently good academic record with excellent results and university top ranks. Ours was the only women's college in 1979 to have had M.Sc., Physics course affiliated to M.K.U. The department has grown to its present state of excellence under the able guidance of efficient heads and dedicated members of the faculty.

Objective of the International Conference

To expose the recent developments, applications and innovations in material science to students, research scholars and faculty members of other discipline.

International Conference on “*A new horizon in materials*” Editorial Board

Editor in Chief

B.Govindarajan

Associate Editors

Mrs. A. Effie Cordelia, Assc. Prof.,

Mrs. S.G. Pushpalatha Gracelin, Asst. Prof.,

Dr. J. Juliet Latha Jeyakumari, Asst. Prof.,

Editors

Mrs. R. Jeyam Jebaraj, Assc. Prof.,

Mrs. P. Elizabeth Jeyarani, Assc. Prof.,

Mrs. D. Jegathi Jasmine, Assc. Prof.,

Dr. F. Jeyamangalam, Assc. Prof.,

Mrs. T. Varthini, Assc. Prof.,

Dr. S. Lincy Mary Ponmani, Asst. Prof.,

Dr. D. Jencylin Navarani, Asst. Prof.,

Mrs. S. Kumutha, Asst. Prof.,

Mrs. M.P. Rameela, Asst. Prof.,

Mrs. K. Sofiya Diana, Asst. Prof.,

Mrs. R. Juliet Jeyanthi, Asst. Prof.,

Mrs. P. Jeyaseeli, Asst. Prof.,

Miss. V. Bala Shunmugajothi, Asst. Prof.,

ORGANIZING COMMITTEE

Patron

Dr. Usha Godwin

Convener

Mrs. R. Suganthi Christina

Organizing Secretary

Mrs. S.G. Pushpalatha Gracelin

Members

Mrs. R. Jeyam Jebaraj

Mrs. P. Elizabeth Jeyarani

Mrs. D. Jegathi Jasmine

Mrs. A. Effie Cordelia

Dr. F. Jeyamangalam

Mrs. T. Varthini

Dr. J. Juliet Latha Jeyakumari

Dr. S. Lincy Mary Ponmani

Dr. D. Jencylin Navarani

Mrs. S. Kumutha

Mrs. M.P. Rameela

Mrs. K. Sofiya Diana

Mrs. R. Juliet Jeyanthi

Mrs P. Jeyaseeli

Miss V. Bala Shunmugajothi



Greetings



To

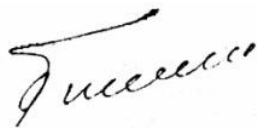
The Organisers,
Department of Physics,
Sarah Tucker College,
Tirunelveli.

I feel immensely pleased in conducting the International Conference on “**A New Horizon in Materials**” (INHIM16) by our Department of Physics.

Many of the greatest inventions are due to the power of Physics. Trees, for example, are not all made in the same way. The black Ironwood tree is so dense that it does not float on water; it just sinks! Another noteworthy tree is the red wood: the bark of a red wood tree is resistant to fire. Albert Einstein provided us with his classical theory of relativity. One area of the theory that is counterintuitive for many people is that as objects move faster they actually get larger. It may also surprise people to realize how much of the universe is made up of empty space. The composition of an atom is considered to be almost entirely empty space.

So a study on the facts of Physics is really surprising

I too appreciate to the efforts taken by the Patron, the Convener, the Organizing Secretary, Teaching & Non-teaching staff of our college to expose the recent developments, applications & innovations in material science to students research scholars and faculty member of other discipline

A handwritten signature in black ink, appearing to read 'Gunasingh Chelladurai'.

Gunasingh Chelladurai
Secretary & Correspondent.



CHURCH OF SOUTH INDIA - TIRUNELVELI DIOCESE
SARAH TUCKER COLLEGE (AUTONOMOUS), TIRUNELVELI
Tamilnadu, India - 627 007
Nationally Assessed and Re-accredited with 'A' Grade
Estd : 1895



Dr Usha Godwin
PRINCIPAL i/c

0462 - 2530946

.. - 2530597

Fax : .. - 2531023

E-mail : sarahtucker95@rediffmail.com



Foreword

Materials have undergone a revolution in the past century, but in many respects the revolution is only just beginning. Innovative materials play essential roles in clean energy, transportation, human health, and industrial productivity. Whether exploring alternative energy sources or developing stronger, lighter materials and sophisticated devices. In earlier days, the range of materials used by scientists in products and systems was very limited. The developments of the 20th century expanded greatly the number of materials and our knowledge of their properties, and brought materials science much more close to manufacturing as we sought to design the properties we wanted from engineered products. Now, in the 21st century, the ability to design new materials and to modify existing ones is still only in its infancy, and the potential is limitless and exciting.

The possibility of influencing material composition and properties at the atomic scale creates opportunities that we are only just starting to explore; the convergence of biology, physics and chemistry is breaking down barriers. Innovation in materials is transforming engineering and the world that we live in. Worldwide, materials are seen as a priority for innovation but also as a source of competition and advantage. Understanding the new horizon in materials in future, the college with the generous support of management, decided to conduct the conference to promote new innovations in material science.

I congratulate the organizing committee of the conference and the entire team of the department of Physics, Sarah Tucker College for steering the young minds. The presentations from academicians, industrialists and materials scientist expose the recent developments, applications and innovations in material science. I convey my best wishes and compliments for the successful conduct of the conference.

Principal (i/c)

Tirunelveli – 7

07.03.2016

Special Issue on INHIM'16



Sarah Tucker College (Autonomous), Tirunelveli.



Mrs. Suganthi Christina, M.Sc., M.Phil

Office:

Associate Professor and Head,
Dept. of Physics,
Sarah Tucker College,
Tirunelveli - 627007,
Tamil Nadu, India.

Residence:

B 143 N.G.O "B" Colony,
Tirunelveli - 627007.
Phone: 0462-2553320
Cell: 9442447151

PREFACE

Materials Science is an interdisciplinary subject spanning the Physics and Chemistry of matter, Engineering applications and Industrial manufacturing processes. Materials Science is very important for the development in nanotechnology, quantum computing, nuclear fusion, biomaterials and metallurgy as well as medical technologies such as bone replacement materials.

Research on materials is essential to study the relationship between the structure, properties and formation of materials. It also includes development of new materials and processes for manufacturing them. Modern society is heavily dependent on advanced materials: light weight composites for faster vehicles, optical fibres for telecommunications and silicon microchips for the information revolution which is the need of the hour.

This International Conference on "A New Horizon in Materials - INHIM'16" brings together Scientists, Research Scholars, Graduate and Post Graduate students to provide exposure to the recent developments, applications and innovations in Materials Science in the following areas:

- ❖ Nanomaterials
- ❖ Biomaterials
- ❖ Theoretical Physics
- ❖ Advanced Material Characterization
- ❖ Computational Material Science
- ❖ Applications of Materials

The call for papers evoked a good response from Faculty, Students and Research Scholars. We have received 8 papers for the oral presentation and 27 papers for the poster presentation that reveals the enthusiasm generated by the Conference. I am confident that **INHIM'16** will be a rewarding experience academically as well as scientifically to all the participants. On behalf of the organizing committee I extend a warm welcome to the Guest Speakers, Delegates and wish them a pleasing experience, an intellectually rewarding and academically refreshing interaction during the Conference.

The blessing of the Almighty God is the prime factor for this International Conference on "A New Horizon in Materials".

(Mrs. Suganthi Christina)
Convenor

Index

S.No	Articles	Page No
IJCSR 41	Low Loss Dielectric Materials for Metal and Superconducting Microwave Resonator Circuits <i>Bindu Gunupudi, Christopher Muirhead and Mark Colclough</i>	353
IJCSR 42	Synthesis and characterization of zinc oxide nano particle by sol-gel route <i>T.Athi Sakthi Grawya and S.Pushpam</i>	359
IJCSR 43	Synthesis and Characterization of SiO ₂ Doped TiO ₂ Thin Films: Influence of Coating Cycles <i>M.Sankareswari, R.Vidhya, A.Azhagu Parvathy and K.Neyvasagam</i>	366
IJCSR 44	Synthesis and characterization of Cu-TiO ₂ thin films by Sol-Gel process <i>R.Vidhya, M.Sankareswari, A. Azhagu parvathy and K.Neyvasagam</i>	379
IJCSR 45	Synthesis and characterization of L-ALANINE DOPED GLYCINE Lithium chloride CRYSTALS GROWN by solution method <i>D.Jencylin NavaRani, P.Selvarajan, S.Lincy Mary Ponmani and N.Balasundari</i>	391
IJCSR 46	Investigation on the nucleation kinetics of urea doped Bis glycine picrate <i>N.Balasundari, P.Selvarajan, S.Lincy Ponmani and D.JencylineNavarani</i>	403
IJCSR 47	Investigation on structural, spectroscopic and mechanical properties of organic non-linear optical DL-alanine oxalate single crystals <i>S.Lincy Mary Ponmani, P.Selvarajan, D.Jencylin and N.Balasundari</i>	411
IJCSR 48	Synthesis and characterization of semi organic nonlinear optical material: Ammonium Tartrate Tetra hydrate <i>S.G.Pushpalatha Gracelin, C.Krishnan and P.Selvarajan</i>	420
IJCSR 49	Studies on the Mechanical and Thermal Properties of Sulphamic Acid Doped Glycine NLO Single Crystals <i>A. Effie Cordelia and S. Perumal</i>	428
IJCSR 50	Electrical conductivity measurements of pure and nickel sulphate doped KDP crystals grown by gel medium <i>M.P.Rameela, Vinu Bharathi and T. Asaithambi</i>	439
IJCSR 51	Systematical calculation of Alpha decay half-lives of heavy nuclei from ground state to ground and excited states of daughter <i>G. M. Carmel Vigila Bai and R. Nithya Agnes</i>	447
IJCSR 52	Synthesized and Characterization of cerium dioxide (ceria) nanoparticles by using a microwave oven <i>R.Anitha, E.Kumar and D. Muthuraj</i>	455
IJCSR 53	Studies on molecular interactions of Bromoform and Ethyl bromide with Benzene at four different temperatures <i>K. Umamakeshvari and U. Sankar</i>	460
IJCSR 54	Z - Scan measurement and impedence analysis of L-alanine alaninium nitrate single crystals (LAAN) <i>R. Jothi mani, P. Selvarajan and C.Parvathiraja</i>	472
IJCSR 55	Studies on optical and mechanical properties of DL-malic acid doped ADP single crystals <i>I.Stella Jeya Christy, A. Effie Cordelia S. Perumal</i>	478
IJCSR 56	Thermal and Dielectric Properties of DL-Malic Acid Doped ADP NLO Single Crystals <i>A.Roselin, A. Sumathi, A. Effie Cordelia and S. Perumal</i>	487

IJCSR 57	Solvothermal Synthesis and Characterization of Manganese Doped Copper Oxide Flower Like Nanostructures <i>A.Suganthi, S.John Kennady Vethanathan, S.Perumal, D.Priscilla Koilpillai and S.Karpagavalli</i>	497
IJCSR 58	Optical and Structural Characterization of Cobalt Doped Manganese Oxide Nanoparticles <i>S. Karpagavalli, S .John Kennady, Vethanathan, S.Perumal, D. Priscilla Koilpillai and A. Suganthi</i>	503



Volume: 2; Issue: 3 [Special Issue]; March-2016; pp 353-358. ISSN: 2454-5422

Low Loss Dielectric Materials for Metal and Superconducting Microwave Resonator Circuits

Bindu Gunupudi^{1*}, Christopher Muirhead and Mark Colclough

School of Physics & Astronomy, University of Birmingham, Edgbaston, Birmingham, United Kingdom B15 2TT

*Corresponding Author Email Id: g.bindumalini@gmail.com

Abstract

The materials used for fabrication of microwave resonator circuits are vital in determining key resonator parameters. These microwave resonator circuits have a wide range of applications such as in the telecommunications industry, in the manufacture of non-invasive blood glucose monitoring devices, kinetic inductance detector devices and to build circuits for studies for quantum mechanical properties. Here we describe the use of a low loss dielectric substrate and a superconducting material to fabricate coupled, superconducting, microwave resonator circuits. We have used oxidized silicon substrates that have a low loss tangent and a dielectric constant of ~ 11.2 . The resonator structures were fabricated on thin film niobium which has a superconducting critical temperature of ~ 9.2 K. The resonators were found to have high quality factors $\sim 10^5$ at 1 K, which was sufficient for our experiments. The behaviour of these circuits was investigated thoroughly, both theoretically as well as experimentally. An in-situ tuning mechanism was designed, constructed and implemented successfully to tune the resonators at low temperatures. A thorough analysis was done to determine the optimum material that could be used for our tuning probe. It was ascertained that macor, an insulating material, that did not cause any interference in the electromagnetic environment could be used for this purpose. Tuning of resonators was performed without degrading the resonators' quality factors, which is a significant experimental achievement. These coupled resonator devices, when cooled to low temperatures ~ 20 mK could further be used to study quantum mechanical properties of macroscopic objects.

Keywords: Coupled Microwave Resonators, Low loss substrates, Tuning of Microwave Resonators

Introduction

The aim of the work described in this paper is to investigate the behavior of a system of coupled, superconducting, microwave resonators and to be able to tune them in-situ at low temperatures. There has been considerable research on dielectric materials that can be used as substrates for resonator circuits [1]. The most important aspect being that there should be no losses within the dielectric substrate. At temperatures $T < 1$ K, irregularities in the dielectric cause the saturation of two-level systems (TLS) and contribute to the noise in the measured signal as well as affect the permittivity ϵ of the substrate, thereby the microwave resonant frequency [2].

The second part of the work describes the design and working of a tuning mechanism that can be used in-situ to tune the microwave resonant frequencies at cryogenic temperatures. There are extensive reports in the literature about the various ways to tune a superconducting microwave resonator [3]. In this experimental project, a mechanical method was designed and implemented and tuning of resonators was successfully achieved. The details of this mechanism are explained in the subsequent sections.

Materials and Methods

The most commonly used substrate materials are silicon and sapphire. This is because of their low loss tangent at frequencies ~ 6 GHz and at temperatures ~ 1 K. In our case, we have used oxidized Silicon substrates. In order to fabricate the resonator structures, thin film (~ 200 nm) niobium which is superconducting below $T_C \sim 9.2$ K was sputter deposited on the substrates. The coupled resonator structures were fabricated using conventional photolithography on 10×5 mm² diced wafers. The samples were glued and wirebonded to a copper PCB and then enclosed in a copper cavity. Low temperature measurements were made by placing the sample enclosure in a liquid helium cryostat with a base temperature of ~ 1.3 K. A Vector

Network Analyser was used to make microwave transmission and reflection measurements on the samples.

In order to design a tuning probe that could be used to tune the system of coupled resonators, a series of tests were performed at room temperature. Both conducting as well as insulating materials, such as brass, nylon and macor were tested. The background transmission was measured it was seen that conducting materials affected the microwave modes and hence could not be used. On taking into account properties such as thermal contraction at low temperatures, it was decided that macor, an insulator would be a suitable material for our

tuning probe. A tuning disc, made of niobium on oxidized silicon substrate was glued to the bottom end of the macor rod. As it was lowered over one of the resonators on the chip, the inductance was reduced and hence there was an increase in its resonant frequency.

Results and Discussion

In our coupled resonators system, we first studied the effect on the frequencies due to a weak coupling between the resonators. Fig.1b shows a comparison between the predicted and measured transmission response from a system of coupled microwave resonators at ~ 1 K.

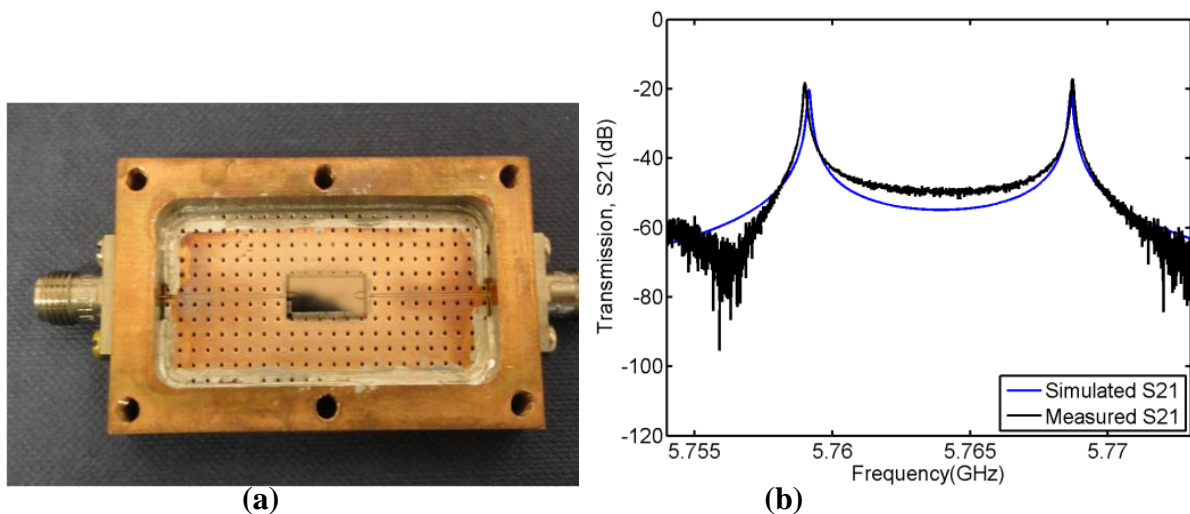


Fig. 1 (a) Shows a sample that is glued and wirebonded to a copper PCB. **(b)** Transmission from a system of coupled resonators at $T = 1.3$ K. The resonator quality factors are $\sim 6 \times 10^4$. This figure is taken from reference [4].

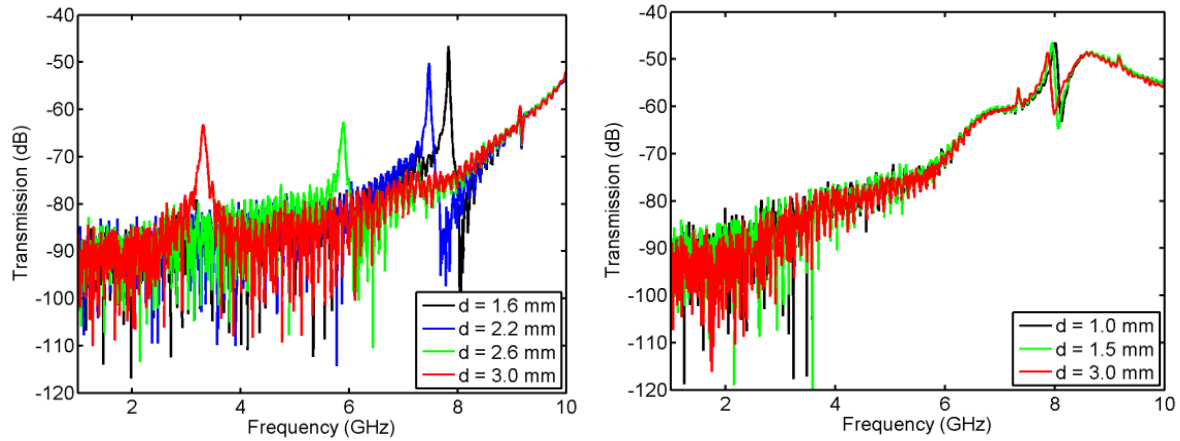


Fig. 2 (a) Shows the effect of lowering a brass (conducting) rod into the sample enclosure. **(b)** Shows the effect of lowering a nylon (insulating) rod into the sample enclosure. This figure is taken from reference [4].

The effect of coupling on the resonant frequencies of a few coupled resonator samples was thoroughly investigated. A mechanism that enabled tuning of resonators was developed. Experiments were conducted to study the effect of inserting conducting and insulating tuning probes on the microwave background transmission. As shown in Figs. 2a and 2b, a conducting and insulating probe were lowered into the sample enclosure. The conducting probe caused a shift in the background resulting in unwanted modes in the frequency range of interest. An insulating probe was preferred since it had no effect on the background whilst being lowered into the sample enclosure.

In our experiments, an insulating material called macor was used. It was chosen for the following reasons: firstly because it is rigid when cooled to temperatures of our interest, i.e., ~ 1 K; secondly, it has a relatively small coefficient of differential contraction, and thirdly, a small dielectric constant and hence, it would not significantly affect the capacitance of the microwave resonators.

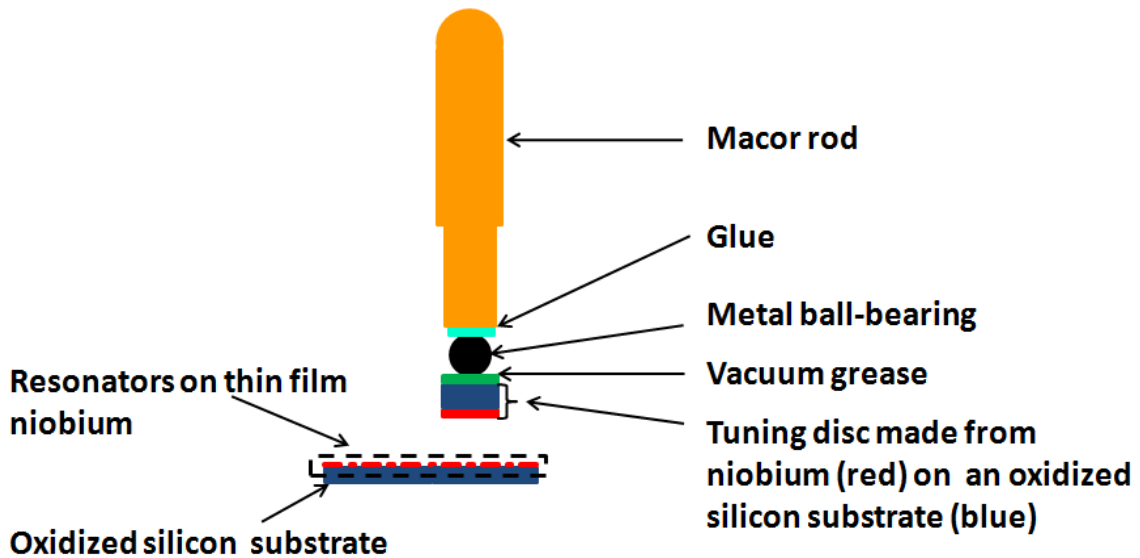
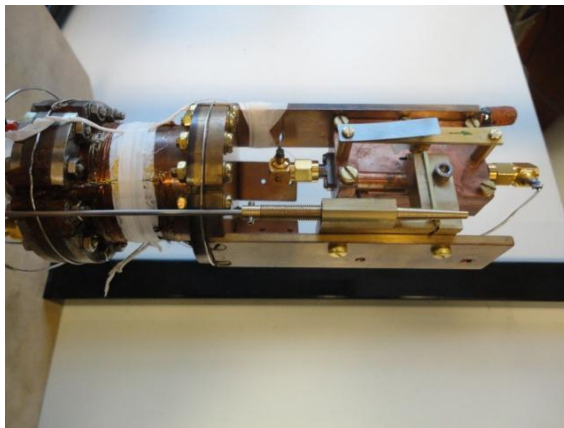
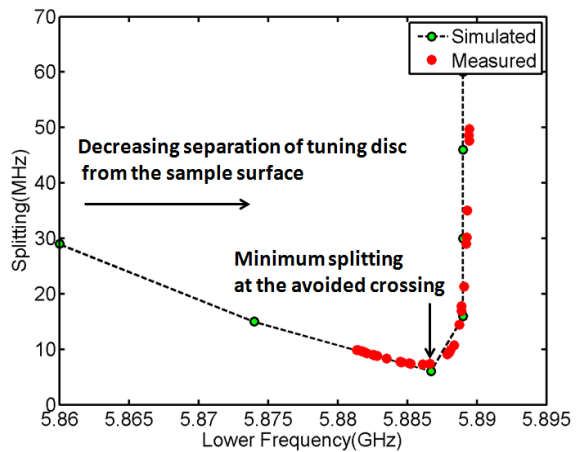


Fig. 3 A schematic of our tuning probe being lowered onto one of the resonators on the chip. This figure is taken from reference [4].

Lastly, the effect of tuning the resonators in-situ was studied. This was done by lowering the tuning probe through the lid of the sample enclosure as shown in Fig. 4a below.



(a)



(b)

Fig. 4 (a) A photograph of an assembled tuning mechanism set-up. (b) A comparison of simulated and measured change in the resonant frequency when the tuning probe is lowered over one of the resonators. This figure is taken from reference [4].

Fig. 4b shows the effect of the resonant frequency of one of the resonators over which the tuning probe was lowered. There is an excellent agreement between the predicted data in AIM Spice and measured data.

Thus we were successful in the studies of coupled superconducting microwave resonator systems as well as in tuning one of their resonant frequencies at low temperatures.

Acknowledgements

I would like to thank the University of Birmingham for the College Elite Scholarship, Gary Walsh for technical assistance and Mr. Krishnarao Gunupudi for his suggestions.

References

- [1] Hammer, G., *et al.* "Superconducting coplanar waveguide resonators for detector applications." *Superconductor Science and Technology* 20.11 (2007): S408
- [2] Barends, R. *et al.* "Contribution of dielectrics to frequency and noise of NbTiN superconducting resonators" *Applied Physics Letters*, 92, 223502 (2008)
- [3] Healey, J. E., *et al.* "Magnetic field tuning of coplanar waveguide resonators." *Applied Physics Letters* 93.4 (2008): 043513
- [4] Gunupudi, Bindu. Coupled superconducting microwave resonators for studies of electro- mechanical interaction. Diss. University of Birmingham, 2015



Synthesis and characterization of zinc oxide nano particle by sol-gel route

T.Athi Sakthi Grawya and S.Pushpam*

Assistant Professor*, Department of Physics, N.M.S.S.Vellaichamy Nadar College, Nagamalai, Madurai, India.

*Corresponding Author Email Id: grawyashree@gmail.com

Abstract

This detailed study is report about the synthesis and characterization of Zinc oxide nano particle (ZnO). ZnO is an important member of semiconducting material of II, VI group. Due to its unique properties, ZnO is the richest family of nano structure among all semiconducting materials. This paper shows that ZnO nano particle is prepared by sol-gel method. Here, ZnO nano particle is readily synthesized using zinc acetate dihydrate as a precursor and ethyl alcohol as solvent. The ZnO nano particle which is obtained from this method by drying process at 80°C in a hot air oven. And the sample were characterized by X-Ray diffraction (XRD), Fourier transform infrared spectroscopy (FTIR), UV-Visible spectroscopy. The particle size measurement which is done by XRD scherrer's formula. The average particle size of the prepared ZnO nano powder is 44.37nm. UV-Visible spectroscopy revealed the formation of ZnO nano particles. The absorption spectrum shows a sharp absorbance onset at 275nm which indicates an almost uniform size of the nano particles. After this, FTIR spectrum of the ZnO nano particles synthesized by sol-gel method which was acquired in the range of 400-4000 cm^{-1} correlated to metal oxide bond (ZnO). The FTIR spectra peak at 414.7 cm^{-1} indicates the characteristic absorption bands of ZnO nano particles. Also the UV-Visible absorption spectrum and XRD shows a typical spectrum for ZnO nano particles.

Keywords: ZnO nano particles, Sol-gel, XRD, UV, FTIR.

Introduction

Today, when the world is surrounding on the roof of technology and electronics, mostly dominated by compatible electronic equipments and thereby creating the need for materials

possessing versatile properties. After digging the pages of history for the search of such type of material a very common category of material comes out that is “semiconductor”. Since independence of India the family of semiconductors is dominated by our very known elements Germanium (Ge) and Silicon (Si). Germanium get famous due to possession of property like low melting point and lack of natural occurring germanium oxide to prevent the surface from electrical leakage where as silicon dominates the commercial market for its better fabrication technology and application to integrated circuits for different purposes.

As time passes on, the rapid growing world demands speed along with technology. This need was very well fulfilled by GaAs which ease the path for the design of high speed and optoelectronic devices. GaAs which is a direct band gap semiconductor possessing higher carrier mobility and higher effective carrier velocity in comparison to Si makes it better suited for optoelectronics devices. But this do not leads to the completion of requirement for the future world, something more is required that is high temperature electronics devices. The world therefore now demands a material that should possess inherent properties like larger band gap, higher electron mobility as well as higher breakdown field strength. So on making investigation about such a material the name of compound comes out is “Zinc Oxide” which is a wide gap semiconductor material very well satisfying the above required properties. Not only has this ZnO possessed many versatile properties for UV electronics, spintronic devices and sensor applications.

Also ZnO has been commonly used in its polycrystalline form over hundred years in a wide range of applications. This ignites many research minds all over the world and creates enthusiasm to develop proper growth and processing techniques for the synthesis of ZnO. ZnO has been used in medical treatment for quite number of years in China. The research on ZnO is catching fire right from the beginning of 1950, with a number of reviews on electrical [1] and optical properties [2] like N-type conductivity, absorption spectra and electroluminescence decay parameter. The decade of 1970 for ZnO passes away in manufacturing of simpler ZnO devices like ceramic varistors, piezoelectric transducers etc [3]. Also with a progress in the study of variety of characterization techniques such as cathodluminescence (CL), capacitance–voltage studies (CV), electrical conduction and so on [4-7].

In the field of ZnO research the last decade was mainly concerned with optimization of different growth parameters and processing techniques. Thus currently research work related to production of high quality, reproducible P-type conducting ZnO for device application is the main focus. ZnO has now become one of most studied material in the last seven years as it presents very interesting properties for optoelectronics and sensing applications, in nano range synthesis.

Materials and Methods

ZnO nano particles were synthesized by several different methods, such as the sol-gel techniques [8], wet chemical method [9], green chemistry [10], microwave method [11], Thermal decomposition method [12, 13], and chemical vapour decomposition method [14]. Here, the ZnO nano particles were prepared by sol-gel method. The crystal structure of the sample was analyzed by means of X-ray diffractometer (XRD). The absorbance spectra were recorded on ultraviolet – visible (UV-Vis) spectrometer. The composition quality of the synthesized material was characterized by Fourier transform infrared spectroscopy in the mid-infra red range ($400\text{--}4000\text{cm}^{-1}$).

All the chemical reagents in this experiment were obtained from commercial sources as guaranteed – grade, and were used as received without further treatment.

In this experiment, the sol - gel method was used for preparation of ZnO nano particles (ZnO-NPs). In a typical procedure 6.3g of zinc acetate dihydrate was added to 200 ml of double distilled water with continuous stirring to dissolve zinc acetate completely. Then the solution was heated to 50°C and 300ml of absolute alcohol was added slowly with stirring. After this, 3ml of H_2O_2 was added dropwise to the vessel and mixed it using a magnetic stirrer to get an almost clear solution. This solution was incubated for 24 hours and the solution was centrifuged and washed several times with double distilled water to remove the by products. After washing the ZnO nano particles is dried at 80°C in a hot air oven. Complete conversion of ZnO will occur during the drying process.

Results and Discussion

X-Ray Diffraction Analysis

The crystallinity was determined by XRD powder diffraction. Analysis is performed by using an XPERT-PRO Diffractometer system equipped with a $\text{CuK}\alpha$ ($\lambda=1.54 \text{ \AA}$) source, Here, about 0.3 g of dried ZnO particles were deposited as a randomly oriented powder into a plexi glass sample container, and the XRD patterns were recorded between 0° to 80° angles. The phase purity and composition of the particles obtained by a sol - gel process examined by XRD. Figure (1.1) shows a typical XRD pattern of ZnO nano particles, prepared in this work. A number of Bragg reflections with 2θ values of 36.12° , 31.63° and 34.30° are observed corresponding to (100), (002), (101) planes[15,16] which shows a typical XRD pattern of ZnO nano particles by using JCPDS 36-1451. The crystallite size (D) of the prepared nano powder can be calculated by using Scherrer's formula.

$$D = 0.9\lambda/\beta \text{ Cos } \theta$$

Where λ is the wavelength of X rays used (1.54060 \AA), β is the fullwidth at half maximum (FWHM) and θ is the angle of diffraction. The crystallite size of prepared ZnO nano powder is found to be 44.37nm .

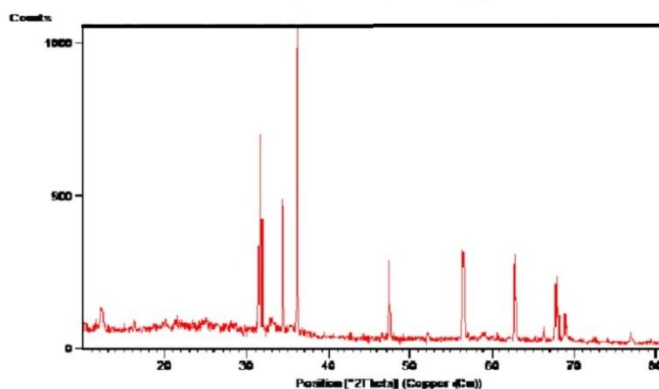


Figure (1.1):- X-Ray Powder Diffraction patterns of ZnO nano particles

UV- Optical Absorption Spectroscopy

Electromagnetic radiation such as visible light is commonly treated as a wave phenomenon, characterized by a wavelength or frequency. Visible wavelengths cover a range from approximately 400 to 800 nm [17,18]. The UV-optical spectra of ZnO is recorded in

SCHIMADZU UV-VISIBLE SPECTRO PHOTOMETER from 200-800 nm. Figure (1.2) shows the UV-Vis optical absorption spectrum of ZnO nano particles as shown in figure (1.2) dried in air at 80°C. The absorption spectrum shows a sharp absorbance onset at 275 nm, which indicates an almost uniform size of the nano particles [19-22].

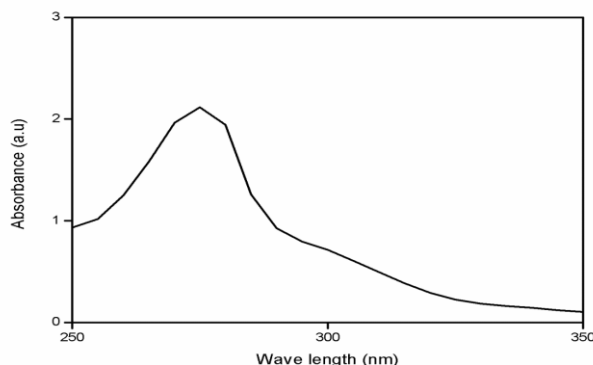


Figure (1.2):- UV-Visible absorption of ZnO nano particle

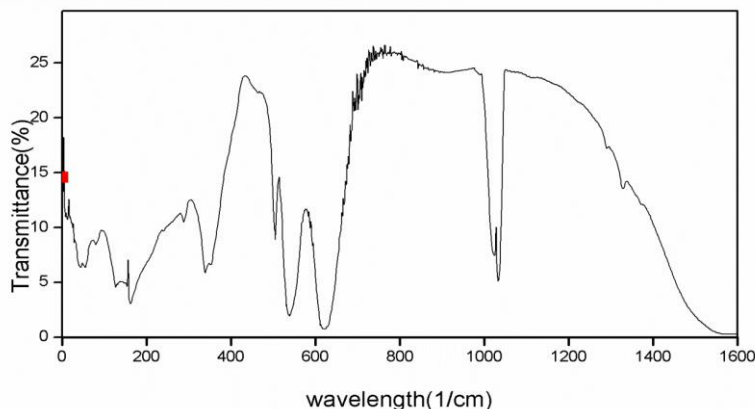
FTIR

FT-IR is an effective method to reveal the composition of products. FTIR stands for Fourier Transform Infrared, the preferred method of infrared spectroscopy. The prepared samples were characterized by FTIR spectroscopy. In infrared spectroscopy, IR radiation is passed through a sample. Some of the infrared radiation is absorbed by the sample and some of it is passed through (transmitted). The resulting spectrum represents the molecular absorption and transmission, gives information of type of bonding in the sample. This makes infrared spectroscopy useful for several types of analysis.

- FTIR can identify unknown materials
- FTIR can determine the quality or consistency of a sample
- FTIR can determine the amount of components in a mixture.

Figure (1.3) shows the FTIR spectrum of the ZnO nano particles synthesized by sol-gel method, [23] which was acquired in the range of 400-4000 cm^{-1} . The band between the 450-500 cm^{-1} correlated to metal oxide bond (ZnO). The peaks in the range of 1400-1500 cm^{-1} corresponds to the C=O bonds. The adsorbed band at 1544 cm^{-1} is assigned O-H bending vibrations. The peak at 1340 cm^{-1} and 1512 cm^{-1} corresponds to C=O and O-H bending vibrations respectively. The peaks in the range of 1600 to 4000 cm^{-1} indicates the

functional group present in it. Also the figure (1.3) shows the typical spectrum of pure ZnO nano particles, the peak at 414.7cm^{-1} is the characteristic absorption of ZnO bond.



Conclusion

ZnO nanoparticles have been prepared using sol-gel method. XRD result which shows the average particle size of ZnO nano particle is 44.37 nm. The synthesized ZnO nanoparticles exhibit the UV absorption peak at 275nm. In FT-IR spectroscopy pure ZnO nanoparticles shows stretching vibrations at $400\text{-}4000\text{cm}^{-1}$. The present work proves it is simple and low cost for producing ZnO nanoparticles.

Acknowledgement

I am grateful to Dr.P.Gnanadurai, Head of the Department, Department of Physics, N.M.S.S.Vellaichamy Nadar College for his encouragement of this work. I would also like to thank Dr.S.Pushpam, Assistant Professor, N.M.S.S.Vellaichamy Nadar College for her constant guidance and encouragement.

References

- [1] A.R. Hutson, Phys.Rev.,108 (1957) 222-230
- [2] G.Heiland, E.Mollwo, F.Stockmann, Solid State Phys.,8 (1959) 193-196
- [3] Shyam Sundar Pareek and Kapil Pareek, IOSR J.App.phy (IOSR-JAP), 3(2):(2013)16-24
- [4] M.Matsuoka, J.App.Phys.,10 (1971) 736
- [5] P.R.Emtage, J.App.Phys.,48 (1977) 4372-4384
- [6] M.Inada, J.Phys.,17 (1978) 1-10

- [7] F.S.Hickerne, J.App.Phys., 44 (1973)1061-1071
- [8] Ameer A, Faheem A, Nishat A, Chaman M, Naqvi A H, J. Alloys and Compounds,496, (2010): 399-402
- [9] Yadav A, Virendra P, Kathe A A, Sheela R, Deepti Y, Sundaramoorthy, et al, 29, (2006), 641-5
- [10] Jayaseelan C, Abdul Rahuman A, Vishnu Kirthi A, Marimuthua S, Santhoshkumar T, Bagavana A, et al, A, 90 (2012) 78-84
- [11] Deepali S, Sapna S, Kaitha B S, Jaspreet R, Mohinder K, App Surface Science, 257, (2011), 9661-72
- [12] Yang Y, Li X. and Bao X, Chemical physics letters 373. (2003), 22-27
- [13] Tonto P. Phatanasri S. and P. Prasertdam, Ceramics International 34: (2008), 57-62
- [14] Wu B.J. and liu S. C, Advanced materials 14; (2002), 215 -218
- [15] Liu B and Zeng H.C, J. Am.Chem. Soc, 125, (2003), 4430-4431
- [16] Shen G.Z, Cho J.H, Xoo J.K, Xi G.C. and Lee C. J, Phys chem. B, 109, (2005), 5491-5496
- [17] Ashtaputre S.S, Dephpande A., Marathe S, Wankhede M.E, Chimanpure J, Parischa R, Urban J, Hiram S.K, Gosavi S.W. and Kulkarni S.K, Phys, 65,(2005), 615-620
- [18] P.K. Giri, S. Bhattacharyya, B.Chetia, Satchi kumari, Dilip K. Singh, J. Nanoscience and Nanotechnology, 11, (2011), 1-6
- [19] Guo L, Cheng X. Y, Yan Y. J. and Ge W. K, Materials science and engineering, C16. (2001) 123-127
- [20] Marcos R.M., Daniel S. V. and Antonio M. N, Material letters, 125. (2014) 75-77
- [21] Shingo T, Atsushi N, Takeharu T. and Hiroyuki Wada, Materials. 4, (2011), 1132-1143
- [22] Tanujjal B, Karthik K. L, Soumik S and Joydeep D, J. Nanotechnology. 4, (2013), 714-725
- [23] Gupta T.K, Ceramic J. Mater. Res., 7, (1992), 3280-3295



Volume: 2; Issue: 3 [Special Issue]; March-2016; pp 366-378. ISSN: 2454-5422

Synthesis and Characterization of SiO₂ Doped TiO₂ Thin Films: Influence of Coating Cycles

M.Sankareswari¹, R.Vidhya¹, A.Azhagu Parvathy² and K.Neyvasagam^{3*}

¹ PG Department of Physics, V.V.Vanniaperumal College for Women, Virudhunagar, India.

² UG Department of Physics, V.V.Vanniaperumal College for Women, Virudhunagar, India.

³ PG and Research Department of Physics, The Madura College, Madurai, India.

*Corresponding Author Email Id: srineyvas@yahoo.co.in

Abstract

Silica doped Titanium di oxide (SiO₂-TiO₂) thin films (different coating cycles 4, 6 & 8) were prepared by spin coating deposition on glass substrate. The prepared films were pre annealed at 100°C for 10 minutes and post annealed at 400°C for 3 hours. Structural and optical properties of the synthesized films were analyzed as a function of coating cycle. X-Ray Diffractometer (XRD), Scanning Electron Microscope (SEM), Energy Dispersive X-Ray Analysis (EDAX), UV-Vis spectrometer and Photoluminescence spectrometer (PL) were used to explore the structural, morphological, stoichiometric ratio and optical properties of the SiO₂ doped TiO₂ thin films. All the films exhibited the anatase phase, tetragonal structure with preferential orientation along the (101) plane. X-Ray line profile analysis was carried out to determine the micro structural properties such as crystallite size, micro strain, dislocation density, number of crystallites and stress of the SiO₂ doped TiO₂ thin films. The crystallite size was found to increase as the coating cycle increases. Morphological studies revealed that the fractured structure on the surface of the films. The stoichiometric ratio of the film was confirmed by EDAX analysis. Surface roughness of the film was characterized by Atomic Force Microscope (AFM). Optical parameters such as band gap, extinction coefficient and refractive index were estimated by optical absorption measurements. Optical band gap values were found to decrease with the increase in coating cycle. Photoluminescence

studies displayed that strong emission peaks were observed at 485 nm, 542 nm and 560 nm. The results of structural and optical characteristic study suggested that coating cycle has strong effect on structural and optical properties of nano crystalline thin films.

Key Words: Thin film, TiO₂, SiO₂, spin coating, XRD, SEM, EDAX, AFM, UV-Vis.

Introduction

TiO₂ is the most attractive materials in nano science and nano technology because of its properties from fundamental and practical point of view [1]. Crystalline titania has three modification phases which are rutile (tetragonal), anatase (tetragonal) and brookite (orthorhombic). Titania nano particles received much interest for its applications such as optical devices, sensors and solar cell applications. There are several factors which determine the performance of TiO₂ for applications such as particle size, crystallinity and the morphology [2 - 4]. Depending on the phase structure, the TiO₂ films can be tailored for different applications. So it is necessary to understand the phase structure of TiO₂ when it is deposited on different substrates [5]. The addition of La₂O₃, CeO₂, CuO, Fe₂O₃, SiO₂ or other oxides into TiO₂ can improve the thermal stability [6]. Additionally the presence of some dopants could increase the adhesion and mechanical stability of thin film on substrates which play a key issue in device stability [6, 7]. The phase transformation of TiO₂ depends on the annealing temperature and dopant [8]. Many methods have been established for thin film synthesis such as sol-gel technique [9], hydrothermal methods [10], chemical vapour deposition [11], physical vapour deposition [12] etc., Among them, sol-gel technique is one of the most widely used methods due to its possibility of deriving unique metastable structure at low reaction temperatures and chemical homogeneity [9].

In the present work, SiO₂ doped TiO₂ thin films were deposited on to glass substrates for various coating cycles (4, 6 and 8). X-ray diffraction analysis was carried out to determine the structural properties of the deposited films. Micro structural parameters such as crystallite size, micro strain, dislocation density,

number of crystallites and stress were estimated from x-ray diffraction data using X-ray line profile analysis technique. Surface morphology, film composition and optical properties were analyzed using scanning electron microscopy, energy dispersive analysis by X-rays and optical absorption techniques respectively. The effect of coating cycles on the structural, morphological and optical characteristics of the SiO₂ doped TiO₂ thin films were studied and the results are discussed.

Experimental details

SiO₂ doped TiO₂ thin films were prepared using sol – gel spin coating technique. All chemicals were analytical reagent grade and used directly without any further purification. The precursors of TiO₂ and SiO₂ were Titanium Tetra Iso Propoxide (TTIP) and Tetra Ethyl Ortho Silicate (TEOS) respectively. Ethanol and acetic acid were selected as solvent and stabilizer of TTIP.

Nano structure SiO₂ doped TiO₂ thin films were prepared by the following method. 4ml TTIP was mixed with 30ml ethanol. Then 1ml acetic acid was dropped slowly to stabilize the solution. 0.1 ml TEOS was added into the matrix of TiO₂ solution and the solution was stirred for one hour. The films were deposited on to glass substrates (25mmx75mmx2mm) by the spin coating method with a speed of 3000 rpm/30s. The films were preannealed at 100°C for five minutes. The procedure was repeated to obtain 4 coating cycles. The same method was followed to prepare two more samples of 6 and 8 coating cycles. Finally all the films were post annealed at 400°C for three hours.

The deposited films were characterized extensively using the following instruments. All the measurements were performed at room temperature. X-ray diffraction pattern of the films were obtained using X' pert pro diffractometer with CuK_α radiation (K = 0.15405 nm) in steps of 0.1 over the 2θ range of 20° - 80°. Morphological examination of the films was done using Hitachi (s-3000H) scanning electron microscope. The optical data and PL spectra of the SiO₂ doped TiO₂ films was calculated using (Schimadzu 1800) UV–Vis–NIR spectrometer and (Schimadzu RF – 5301) Photoluminescence spectrometer. The thickness of the prepared films was measured by using (Surfest SJ – 301) stylus profilometer.

Results and discussion

Structural studies

To study the crystalline quality of the SiO₂ doped TiO₂ thin films for different number of coating cycles, the films were subjected to X-ray diffraction analysis. The XRD pattern recorded for SiO₂ doped TiO₂ thin films for different coating cycles is shown in Figure 1.

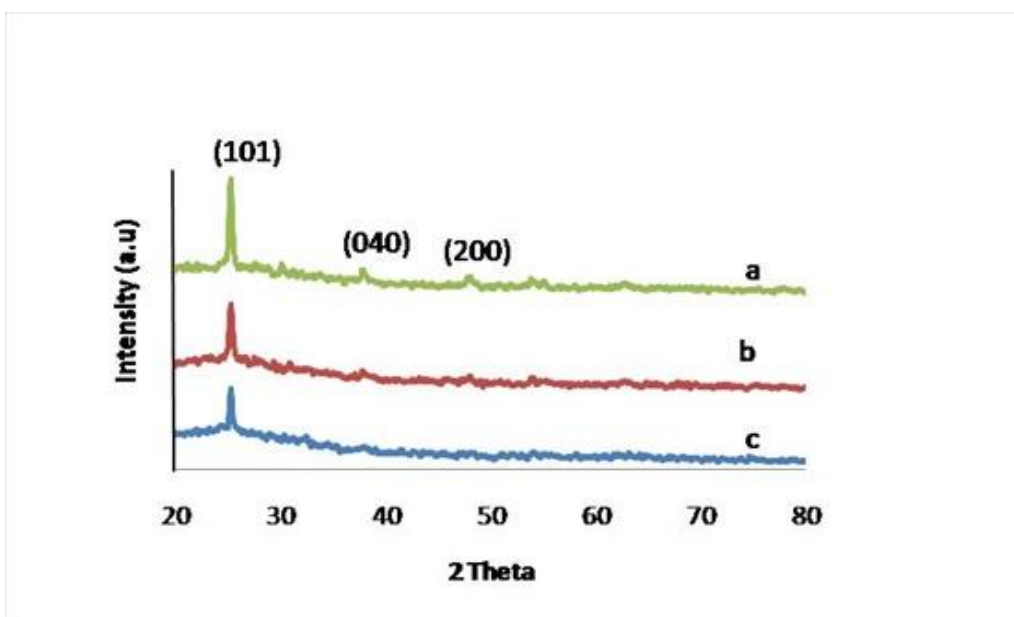


Fig .1: XRD Pattern of SiO₂ doped TiO₂ thin films for a) 8 coating cycles b) 6 coating cycles c) 4 coating cycles

The XRD result shows that all the films have anatase phase with a preferential orientation along (1 0 1) plane. All the prepared SiO₂ doped TiO₂ films have (1 0 1), (0 4 0), (2 0 0) peaks. When the coating cycle increases, there is a slight increase in the height of peaks. It is observed that there is no change in the phase structure of the SiO₂ doped TiO₂ thin films. Table 1 shows the observed and calculated values which were found to be in agreement with standard JCPDS data (File no. 89-4203).

The average crystal size of the deposited film was determined from Full Width Half maximum (FWHM) data using the following Scherrer formula

$$D = \frac{0.9\lambda}{\beta \cos\theta} \text{ (nm)} \quad (1)$$

Where β is the FWHM in radians θ is the Bragg's angle, λ is the x-ray wavelength (CuK α =0.15405 nm). As the coating cycle increases, the intensity of the peaks also increase which reveals that the crystallinity increases due to the preferential growth

of the SiO₂ doped TiO₂. The crystallite size of the SiO₂ doped TiO₂ thin films was found to increase from 20.22 nm for 4 coating cycles to 53.93 nm for 8 coating cycles.

In addition to the changes in crystallite size, crystal defects may occur by the effect of coating cycles. Crystal dislocation is the main defect related to the crystallite size. It needs to be addressed and hence the dislocation density available in the SiO₂ doped TiO₂ thin film is calculated from the given formula,

$$\delta = \frac{1}{D^2} \quad (2)$$

where 'D' is the crystallite size of the SiO₂ doped TiO₂ thin film. The observed results are summarized in table 1. The dislocation density decreases as the coating cycle increases.

The micro strain of the SiO₂ doped thin film was measured using the relation

$$\varepsilon = \frac{\beta \cos\theta}{4} \quad (3)$$

From Table 1, it is observed that the strain value decreases from 0.098 for 4 coatings to 0.036 for 8 coatings. The decrease in strain with increase in coating cycles implies that lattice imperfection is due to increase in crystallite size.

The number of crystallites per unit area (N) of the SiO₂ doped TiO₂ thin film was determined using the relation

$$N = \frac{t}{D^3} \quad (4)$$

where t is the thickness of the film. The calculated values are summarized in Table 1. Fig 2(a) and (b) show the variation of crystallite size & dislocation density and variation of thickness and micro strain respectively with number of coating cycles.

Malliga *et al.*, [13] observed similar results in their investigation on TiO₂.

Table 1: Structural parameters of SiO₂ doped TiO₂ thin films for various coating cycles.

Coating Cycles	2θ (degree)		(hkl) orientation	Phase and crystal structure	Thickness (μm)	Crystallite size D (nm)	Dislocation Density δX10 ¹⁴ lines /m ²	Micro strain μX10 ⁻³	No. of crystallites per unit area NX10 ¹⁶
	Observed	Standard							
4	25.254	25.304	101	Anatase, tetragonal	1.8	20.22	24.45	0.09	21.8
6	25.245	25.304	101	Anatase, tetragonal	1.9	40.43	6.12	0.05	2.87
8	25.256	25.304	101	Anatase, tetragonal	2	53.93	3.43	0.03	1.27

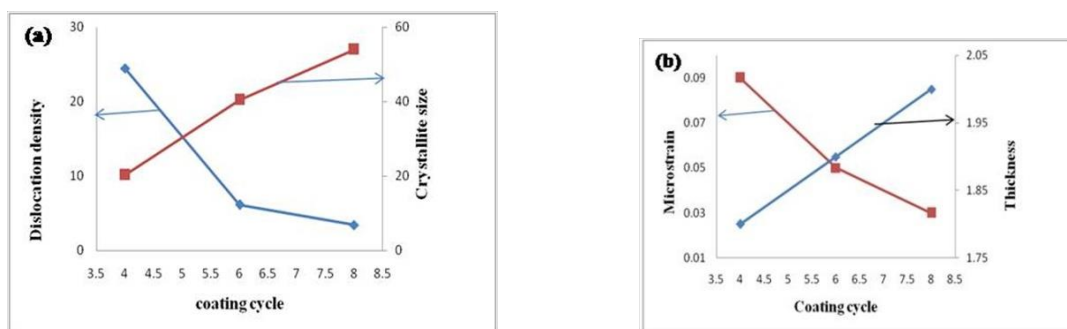


Fig 2 (a) variation of crystallite size & dislocation density and 2 (b) thickness & micro strain with coating cycles

Morphological and Compositional analysis

Figure 3 shows the SEM micrographs of 4 and 8 coating cycles of SiO₂ doped TiO₂ thin films. The films produced by this technique indicate fractured morphology. During the drying and annealing processes of the films, crack formation takes place as a result of contraction, stress and different thermal coefficients of expansion of the layer and substrate [5]. The fractured surface morphology of the SiO₂ doped TiO₂ thin films produced by this technique which resulted in a large surface area suggest a high photo catalytic activity. The results also suggest that uniformity of the thin film improves with increasing coating cycles.

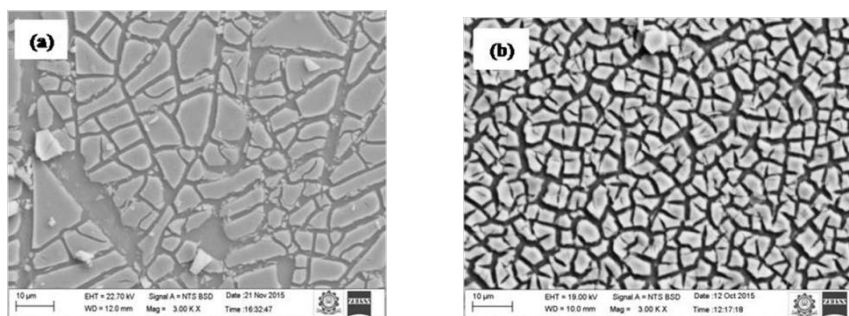


Fig.3 SEM micrographs of SiO₂ doped TiO₂ thin films (a) 4 coating cycles (b) 8 coating cycles

Figure 4(a) & (b) shows the EDAX pattern of SiO₂ doped TiO₂ thin films of 4 coating cycles and 8 coating cycles. EDAX results indicated the main peaks of Ti, Si and O. The presence of SiO₂ in the thin film could destroy the linkage of Ti-O-Ti and would change it to Ti – O – Si. This aspect can shift binding energy of Si to higher a value [14].

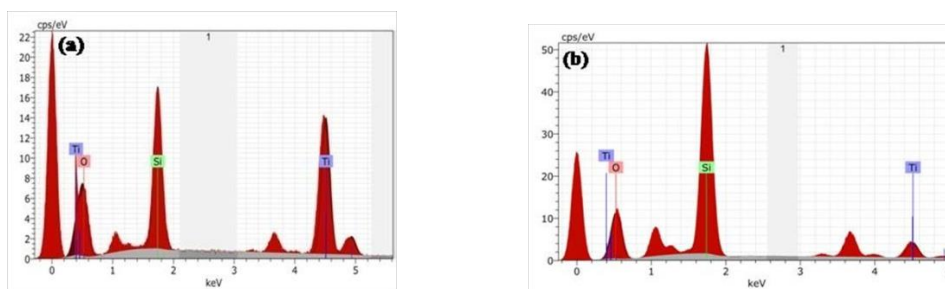


Fig.4 EDAX spectra of SiO₂ doped TiO₂ thin films (a) 4 coating cycles (b) 8 coating cycles

Atomic Force Microscope (AFM) was used to characterize the surface roughness of the thin film. AFM images (2D & 3D) of SiO₂ doped TiO₂ thin film for 8 coating cycles is shown in Figure 5. The root mean square and roughness values of the SiO₂ doped TiO₂ thin film are 16.40 nm and 10.93 nm respectively.

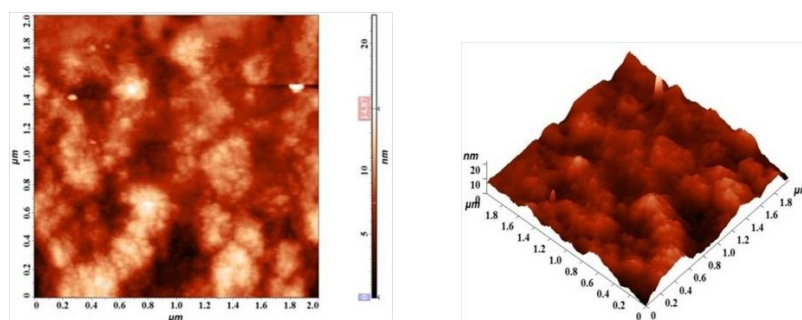


Fig.5 AFM image of SiO₂ doped TiO₂ thin film for 8 coating cycles

Optical analysis

The transmittance and reflectance spectra were recorded at room temperature to obtain the information of optical properties of SiO₂ doped TiO₂ thin films. The transmittance spectra of the SiO₂ doped TiO₂ thin films obtained in the range between 300 and 800nm for different number of coatings is shown in Figure 6. The reduction in the transmittance with increase in coating cycles may be attributed to the effect on the surface roughness and grain size boundary of the thin films as described in earlier studies [15 – 18].

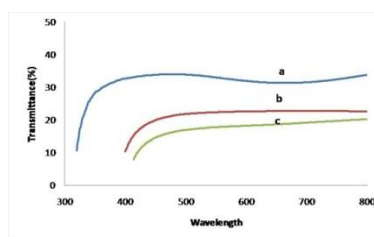


Fig.6 Transmittance spectra of SiO₂ doped TiO₂ thin films (a) 4 coating cycles (b) 6 coating cycles (c) 8 coating cycles

The reflectance spectra of the SiO₂ doped TiO₂ thin films for different number of coating cycles is shown in Figure 7. It shows that the reflectance the film increases as wavelength increases. The highest reflectance value of about 70% is obtained for films with 4 coating cycles.

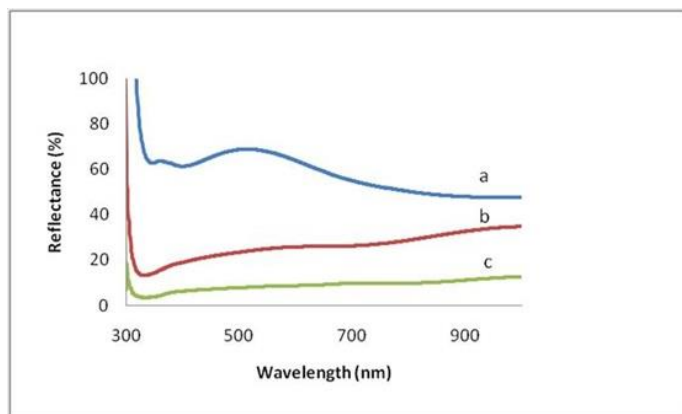


Fig.7 Reflectance spectra of SiO₂ doped TiO₂ thin films (a) 4 coatings
(b) 6 coating cycles (c) 8 coating cycles

The nature of transition is determined using the following equation

$$\alpha h\nu = k(h\nu - E_g)^m \quad (5)$$

Where α is the absorption coefficient in cm⁻¹, $h\nu$ is the photon energy, E_g is an energy gap in eV and A is a constant. The value of 'm' determines the type of transition present in the material. If $m = 1/2$ indicates that the transition involved in the material is direct allowed and $m = 2$ indicates that the transition involved in the material is indirect allowed. A plot of $(\alpha h\nu)^2$ with photon energy ($h\nu$) and $(\alpha h\nu)^{1/2}$ with photon energy ($h\nu$) for SiO₂ doped TiO₂ thin films obtained for 4, 6 and 8 coating cycles are shown in Figure 8 (a) and 8 (b).

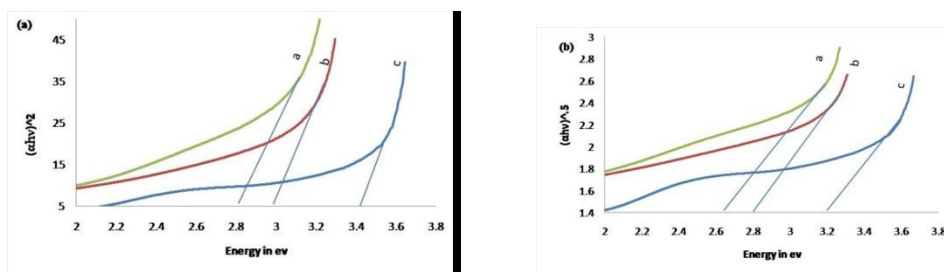


Fig. 8 a) Direct and b) Indirect band gap of SiO₂ doped TiO₂ thin films for
(a) 4 coating cycles (b) 6 coating cycles (c) 8 coating cycles

Extrapolation of linear portion of the graph to X-axis (energy) gives the band gap value of the material. The direct and indirect band gap values of the films obtained in the present work are found to be 3.4, 3, & 2.8 eV and 3.2, 2.8 & 2.6 eV for 4, 6 and 8 coating cycles respectively. The reason for decrease in band gap energy is attributed to quantum size effect.

The values of refractive index n and extinction coefficient (K) are determined using the following equations (7) and (8)

$$n = \frac{1 + R^{0.5}}{1 - R^{0.5}} \quad (6)$$

$$K = \frac{\alpha\lambda}{4\pi} \quad (7)$$

where n is the refractive index of the material, K is the extinction coefficient and R is the reflectance (%). The variation of refractive index with energy for various coating cycles is shown in Figure 9. The maximum value of refractive index is observed at 6 for 8 coating cycles. Also refractive index values of the prepared thin films for 6 coating cycles and 4 coating cycles are estimated at 4 and 2 respectively. The refractive index variation may be due to the film thickness. The same variation is observed in extinction coefficient of the SiO_2 doped TiO_2 thin films as shown in Figure 10.

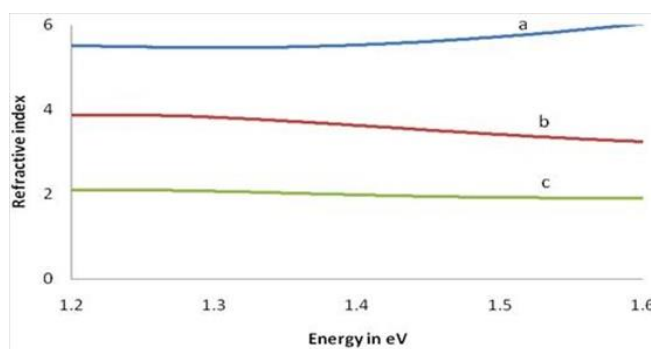


Fig.9 Refractive Index versus photon energy for SiO_2 doped TiO_2 thin films for
(a) 8 coating cycles (b) 6 coating cycles (c) 4 coating cycles

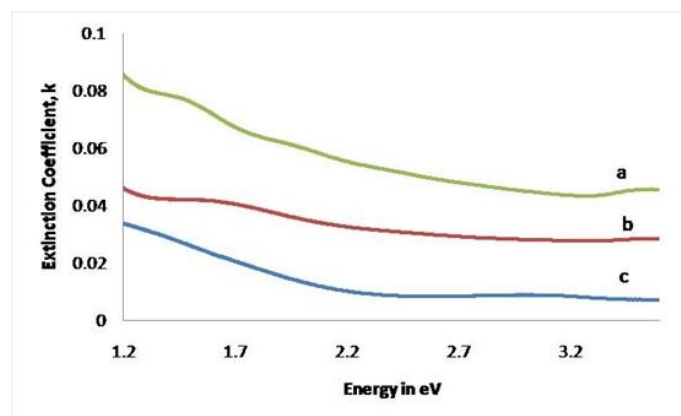


Fig.10 Extinction coefficient versus photon energy for SiO₂ doped TiO₂ thin films for (a) 8 coating cycles (b) 6 coating cycles (c) 4 coating cycles

To further validate the crystalline quality of the thin films, photoluminescence emission spectroscopy was used and the results are illustrated in Figure 11. PL spectra observed at excitation wavelength of 410 nm demonstrate that all the SiO₂ doped TiO₂ films exhibit three peaks (485nm, 542nm and 560nm) which lie in the visible range. The peaks in the visible region are associated with structural defects [19]. The structural defects of a seed solution exhibited in the visible region are referred to as native point defects and include oxygen vacancies which present deep energy levels of the band gap [20 – 21]. It was observed that the PL peaks of SiO₂ doped TiO₂ thin films are almost in the same wavelength position but have varying intensities for different number of coating cycles. The PL intensity of SiO₂ doped TiO₂ thin films increase with increase in number of coating cycles. This increase is due to the improvement in quality and increase in oxygen vacancies. It reveals that increase in the coating cycles could improve the structural quality which can contribute its usage as a transducer in biosensing applications [22].

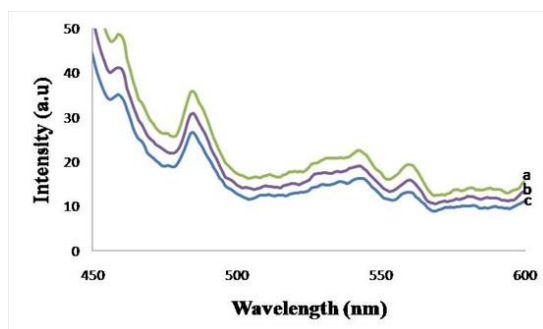


Fig. 11 PL spectra of SiO₂ doped TiO₂ thin films for (a) 8 coating cycles (b) 6 coating cycles (c) 4 coating cycles

Conclusion

SiO₂ doped TiO₂ thin films were deposited successfully onto glass substrates using spin coating technique for 4, 6 and 8 coating cycles respectively. X-ray diffraction analysis revealed that the prepared films have anatase phase with tetragonal structure with preferential orientation along (1 0 1) plane. Also the crystallite size was found to be 20.22 nm, 40.43 nm and 53.93 nm for 4 coating cycles, 6 coating cycles and 8 coating cycles respectively. The micro structural parameters such as dislocation density, strain and stress were estimated. Surface morphology showed that the films have fractured structure. EDAX analysis revealed that films with Ti, O and Si elements are obtained. Optical absorption measurements indicated that the deposited film has a direct band gap value of 3.4, 3 & 2.8 eV and indirect band gap value of 3.2, 2.8 & 2.6 eV for 4, 6 and 8 coating cycles respectively. PL spectra intensity increases with increase in number of coating cycles. The result of thickness suggested that thickness of the film increases as the coating cycle increases. Surface topography was found by using AFM. The uniformity of the film increases with coating cycles. These results showed that the properties of SiO₂ doped TiO₂ thin films were considerably influenced by the coating cycles and the nano crystalline SiO₂ doped TiO₂ films are desirable material for photo catalytic applications.

Reference

1. Castillo,N., Olguin,D., CondeA., Gallaro Jimenez,S. Structural and morphological properties of TiO₂ thin film prepared by spray pyrolysis. *Rensta Mexicana De Fisica*. 50(4), 382, 2004
2. Mahsid,S., Askari,M., Ghamsari,M.S., Afshar,N., Lahuti,S. Mixed-phase TiO₂ Nano particles preparation using sol-gel method. *J. Alloys and compounds*. 47, 586-589, 2009
3. Wang C.C and Ying J.Y. Sol-gel synthesis and hydro thermal processing of anatase and rutile Titania and nano crystal. *Chem. Mater*. 11,3113-3120,1999
4. Liu,T., Wang,W., Ma,T., Tao,J., Zhang,J and Hu,T. Synthesis and characterization of titania prepared by using a photo assisted sol-gel method. *Langmour*. 19, 3001-3005, 2003



5. Shanmugam,S., Mutharasu,D and Haslan A,H. Structural analysis of RF sputtered TiO₂ thin film on cu substrate for various annealing temperatures. *Int. J. Engineering Trends & Technology*. 14 (2),57-60, 2014
6. Lek Sikong., Jiraporn Damchan., Kalayanee Kooptarnond and Sutham Niyomwas . Effect of doped SiO₂ and calcinations temperature on phase transformation of TiO₂ photocatalyst prepared by sol–gel method. *Songklanakarinn J. Sci. & Technology*. 30(3), 385-391,2008
7. Z.Wenguang, L.Weimin, W.Chengtao Tribological investigations of sol-gel ceramic films. *J.Sci.Chin.B*.45 (2002)
8. Yuranova,T., Mosteo,R., Bandara,J., Laub,D and Kiwi,J. Self-cleaning cotton textiles surface modified by photoactive SiO₂/TiO₂ Coating. *J. Molecular catalysis A: Chemical*. 244, 160-167,2005
9. Bischof,B.L., and Anerson,M.A. Peptization process in the sol-gel preparation of porous anatase TiO₂. *Chem.Mater*.7,1772 - 1778, 1995
10. Jinghuanzhang., XinXiao, JunminNan. Hydro Thermal hydrolysis synthesis and photo catalytic properties of nano-TiO₂ with an adjustable crystalline structure. *J. Hazardous Materials*, 176-617-622, 2010
11. Dongjin Byun, Yongki Jin, Bumjoonkim Joongkee Lee, Dalkeum Park. Photocatalytic TiO₂ deposition by chemical vapour deposition. *J. Hazardous Materials*. 73, 199-206, 2000
12. Balachandran,K., Venckatesh,R, Rajeshwari Sivaraj. Synthesis of Nano TiO₂–SiO₂ Composite using sol gel method. Effect of ize, surface morphology and thermal stability. *IJEST*, 2(8), 3695-3700, 2010
13. Malliga,P., Pandiarajan,J., Prithivikumaran,N and Neyvasagam,K. Influence of Film Thickness on structural and optical properties of Sol – Gel spin Coated TiO₂ thin film .*IOSR J. Applied Physics*. 6, 22-28,2014
14. Rahmani,E., Ahmadpour,A., Zebarjad,M .Enhancing the photocatalytic activity of TiO₂ nano crystalline thin film by doping with SiO₂. *Chemical Engineering J*. 174, 709-713, 2011
15. Xu,L,Lix. Influence of Fe – doping on the structural and optical properties of ZnO thin films prepared by sol gel method. *J. Crystal Growth*.312,851-855, 2010
16. Tcheliobou,F., Ryu,H.S., Hong,C.K., Park,W.S., Baik,S. On the microstructure and optical properties of Ba Sr TiO₃ films.*Thin solid films* .299, 14-17, 1997



17. Xu,L., Zheng,G., Lai,M., Pei,S. Annealing impact on the structural and photoluminescence properties of ZnO thinfilms on Ag substrate. *J. Alloys comp.* 583,560-565, 2014
18. Singh,A., Singh,S., Joshi,B.D., Shukla,A., Yadav,B,C., Tandon,P. Synthesis, characterization, magnetic properties and gas sensing applications of $Zn_xCu_{1-x}Fe_2O_4$ nanocomposites. *Mater Science Semiconductor Process*, 27,934-949,2014
19. Fabbri.F., Villani.M., Catellani.A., Calzolari.A., Cicero.G. Zn vacancy induced green luminescence on non polar surfaces in ZnO nano structures. *Sci Rep* 4:5158, 2014
20. Thandavan.TMK., Gani.SMA., SanWong.C., Nor.R. Enhanced Photoluminescence and Raman properties of Al doped ZnO nano structures using Thermal Chemical Vapour Deposition of Methanol assisted with heated Brass. *PLOS One*.10,2015
21. Jin.X., Gotz.M., Wille.S., Mishra.y.k., Adelung.R., Zollfranz.C. A novel concept for self reporting materials:stress sensitive photoluminescence in ZnO tetrapod filled elastomers. *AdvMater.* 25,1342-1347, 2013
22. Hariindraprasad.R., Hashim.U., Subash C.B Gopinath. Low temperature annealed zinc oxide nano structured thin film based transducer: Characterization for sensing applications. *PLOS ONE*. 10(7), 1-20, 2015



Synthesis and characterization of Cu-TiO₂ thin films by Sol-Gel process

R.Vidhya¹, M.Sankareswari¹, A. Azhaghu parvathi² and K.Neyvasagam^{3*}

¹PG Department of Physics, V.V.Vanniaperumal College for Women, Virudhunagar, India.

²UG Department of Physics, V.V.Vanniaperumal College for Women, Virudhunagar, India.

³PG and Research Department of Physics, The Madura College, Madurai, India.

*Corresponding Author Email Id: srineyvas@yahoo.co.in

Abstract

Copper doped TiO₂ (Cu-TiO₂) thin films have been deposited onto the microscopic glass substrate by spin coating technique. The influence of varying coating cycles (3, 5 and 7) on the structural, surface morphological and optical properties of the films have been studied by X-ray diffraction method (XRD), Scanning Electron Microscopy (SEM) with Energy Dispersive X-ray Analysis (EDAX), Atomic Force microscopy (AFM), UV-Vis absorption spectroscopy (UV-Vis-NIR), and Photoluminescence (PL) study. The X-ray diffraction pattern of Cu-TiO₂ films confirmed the tetragonal crystal structure of anatase phase with a strong orientation along (1 0 1) plane. The X-ray line profile analyses have been carried out to determine the micro structural parameters such as crystallite size, micro strain and dislocation density. The thickness of the films was about 0.96 μm to 1.8 μm using stylus profilometer. Morphological studies have revealed that grains are agglomerated, irregular with mosaic like structure. The elemental compositions of the films were confirmed by EDAX spectrum. The UV-Visible spectral analysis showed the transmittance and band gap (direct & indirect) were found to decrease with increase in coating cycles. The room temperature PL spectra of Cu-TiO₂ thin films show blue and green emissions at 485 nm and 545 nm with excitation at 410 nm. These results suggest that the varying coating cycles is an important parameter for the improvement of structural and optical quality of Cu-TiO₂ thin films derived by sol-gel spin coating technique.

Keywords: Cu-TiO₂ thin film, spin coating method, XRD, AFM, UV-Visible, PL, SEM, EDAX.

Introduction

Titanium dioxide (TiO₂) is one of the most important semiconductor materials in daily life; moreover, it has been widely used in fuel cell, solar energy conversion, photo catalysts/catalyst for environmental remediation process, white pigment in paints and paper and ultra-violet absorber in sunscreen cream [1-3]. Such wide range of application is quite reasonable, because TiO₂ is an inexpensive, environmentally friendly material with high chemical stability, high mechanical strength and photo activation. TiO₂ possesses three different crystal structure: rutile (tetragonal), anatase (tetragonal) and brookite (orthorhombic). The anatase crystalline TiO₂ has been found to be the most active photocatalyst due to slow recombination rate of excited electron and hole compared to that of rutile and brookite [4].

However, exploring the properties of TiO₂ for improving its efficiency is still an emerging area of research. In this regards, modifications of intrinsic properties of TiO₂ by doping with transition metal like Cu [5], Co, V [6], Fe [7] and Nb [8] have long been proposed. Specially, copper (Cu) was found to be one of the most considerable element among the transition metal because of its notable effects on the activity of TiO₂. The existence of Cu species at TiO₂ plays an important role on the activity, because Cu could influence the particle size [9], optical or electronic properties of TiO₂ [10] as well as the number of oxygen or intermediate species on the surface of the TiO₂ [11]. A number of methods have been reported to prepare Cu doped TiO₂ thin films, including chemical vapor deposition [12], spray pyrolysis [13], sputtering [14], sol-gel process [15] etc. Among these, sol gel technique has many advantages over other synthesis techniques for its excellent control over chemistry, homogeneity, purity and crystalline phase.

In our work, we prepared the Cu-TiO₂ films by sol-gel spin coating method. Their influence with varying coating cycles on structural, surface morphological and optical properties have been investigated.

Materials and Methods

Raw materials

Titanium (IV) isopropoxide (TTIP, 99.95 %, Sigma-Aldrich), and copper (II) nitrate trihydrate ($\text{Cu}(\text{NO}_3)_2 \cdot 3\text{H}_2\text{O}$) were used as raw materials. Ethanol ($\text{C}_2\text{H}_5\text{OH}$, 99.9 %, Merck Germany) was used as a solvent.

Preparation of Cu-TiO₂ thin films

Cu-TiO₂ thin films were prepared at room temperature by using sol-gel spin coating technique reported previously [16]. A stoichiometric amount of titanium (IV) isopropoxide was mixed with ethanol and magnetically stirred for 10 min, and then glacial acetic acid was added and stirred for 15 min. To achieve the desired concentration of Cu ion as a dopant in TiO₂ host lattice, required stoichiometric amount of Copper II Nitrate trihydrate ($\text{Cu}(\text{NO}_3)_2 \cdot 3\text{H}_2\text{O}$) as a dopant precursor was dissolved in ethanol. This dopant solution was then added to the mixture and stirred vigorously for 2 hour. Prior to deposition the substrates were cleaned with soap solution, acetone, chromic acid and distilled water. Finally the substrates were ultrasonically cleaned for 30 minute.

The gel was dropped onto the cleaned glass substrates which were rotated at a speed of 3000 rpm/30 s by using a spin coater. The coated layer was dried at 100°C for 5 min in a muffle furnace. The process of spinning and drying was repeated for two more times to obtain a three-coating film. Two more films of five and seven coatings were also prepared. Finally, three, five, and seven layer coated films annealed at 500°C for 3 hour were also synthesized.

Characterizations

The XRD pattern of Cu-TiO₂ thin films obtained for various coating cycles were characterized by X-Ray diffraction (XRD) using X'PERT-PRO X - ray diffractometer which was operated at 40 KV and 30 mA with $\text{CuK}\alpha_1$ radiation of wavelength 1.5406 Å. The surface morphological observations and elemental analysis were done by EV018 Carlzeiss SEM and S-Flash 6130 Bruker EDAX respectively. The thickness of the films was measured using Surfest SJ-301 (Stylus profilometer). UV-Visible spectra were recorded in the range of 400-700 nm by using the (Schimadzu 1800) UV-VIS-NIR spectrophotometer. The Photoluminescence (PL) spectra were recorded using (Schimadzu RF-5301) luminescence

spectrophotometer with xenon lamp as the light source at room temperature with an excitation wavelength of 410 nm.

Results and Discussion

XRD analysis

The XRD patterns of different coating cycles of Cu-TiO₂ thin films coated on glass substrate by spin coating method is shown in figure 1.

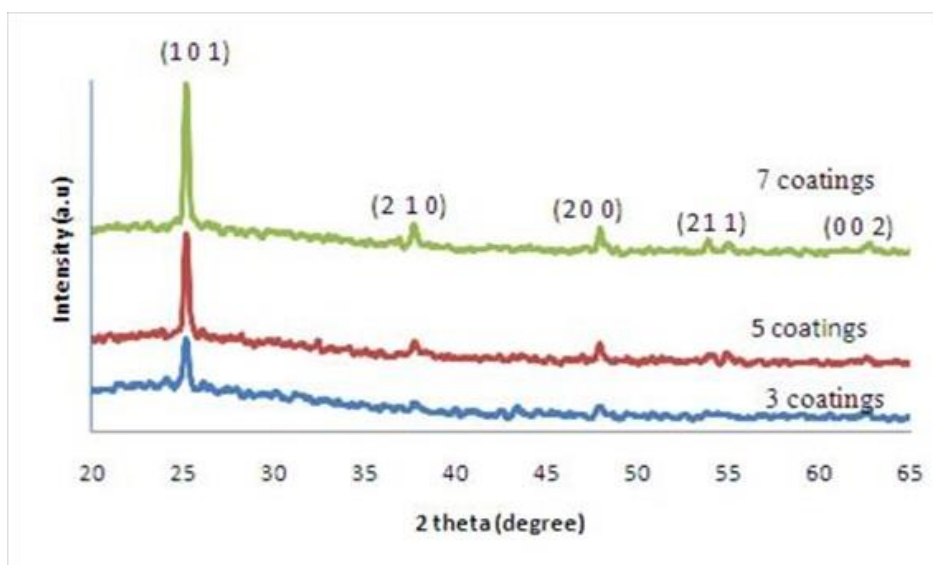


Figure1: XRD pattern of Cu-TiO₂ films for different coating cycles

The observed XRD patterns show that the coated films have tetragonal BCC structure of anatase phase with high intensity peak in (1 0 1) orientation. The other orientations (2 1 0), (2 0 0), (2 1 1) and (0 0 2) are also observed for all the samples with low intensities which is consistent with JCPDS file no. 89-4203. From the XRD pattern, it is observed that the intensity of the peaks increases with increase in number of coating cycles. The film thickness values measured using stylus profilometer are given in Table 1.

The crystallite size was determined using the Debye- Scherrer's formula,

$$D = \frac{k\lambda}{\beta \cos\theta} \text{ (nm)} \quad (1)$$

where D = particle size (nm), k = shape factor (0.94), λ = wavelength of the incident X-ray beam in Å°, β = full width at half maximum (FWHM) of the prominent peak, and θ =

diffraction (Bragg) angle. From the calculation it is found that the crystallite size increases with increase in coating cycles. Similar results have been shown by earlier literature saranya et.al, [17]. Using the size of the crystallites, the dislocation density (δ) and strain in the films (μ) has been determined from the relations given below

$$\delta = \frac{1}{D^2} \quad (2)$$

$$\mu = \frac{\beta \cos\theta}{4} \quad (3)$$

where t is the film thickness. The calculated crystallite size, dislocation density and strain values were summarized in Table 1. From the calculation it was observed that as the coating cycle increases, the crystallite size also increases whereas the dislocation density and micro strain decreases which reveals the improved crystalline structure.

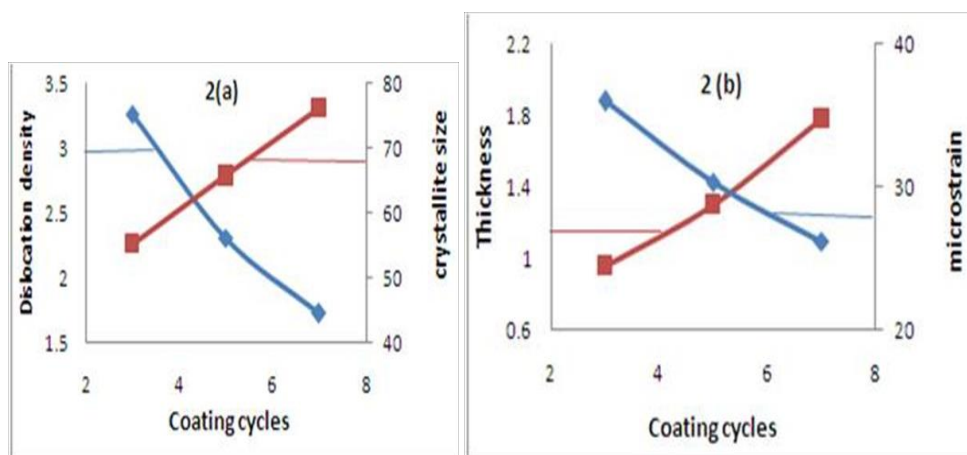


Figure: 2(a) Variation of crystallite size and dislocation density & 2(b) variation of thickness and strain with different coatings of Cu-TiO₂ thin films

Table 1: Micro structural parameter of Cu-TiO₂ thin films with varying coating cycles

Number of coatings	Crystallite size D (nm)	Thickness t (μm)	Dislocation density(δ) lines/m ²	Strain μ ($\times 10^{-3}$)
3	55.30	0.96	3.27	36.01
5	65.77	1.30	2.31	30.03
7	76.14	1.8	1.73	26.15

Surface morphology with Elemental analysis

The SEM micrographs of Cu-TiO₂ thin films prepared at various coating cycles are shown in Figure 3.

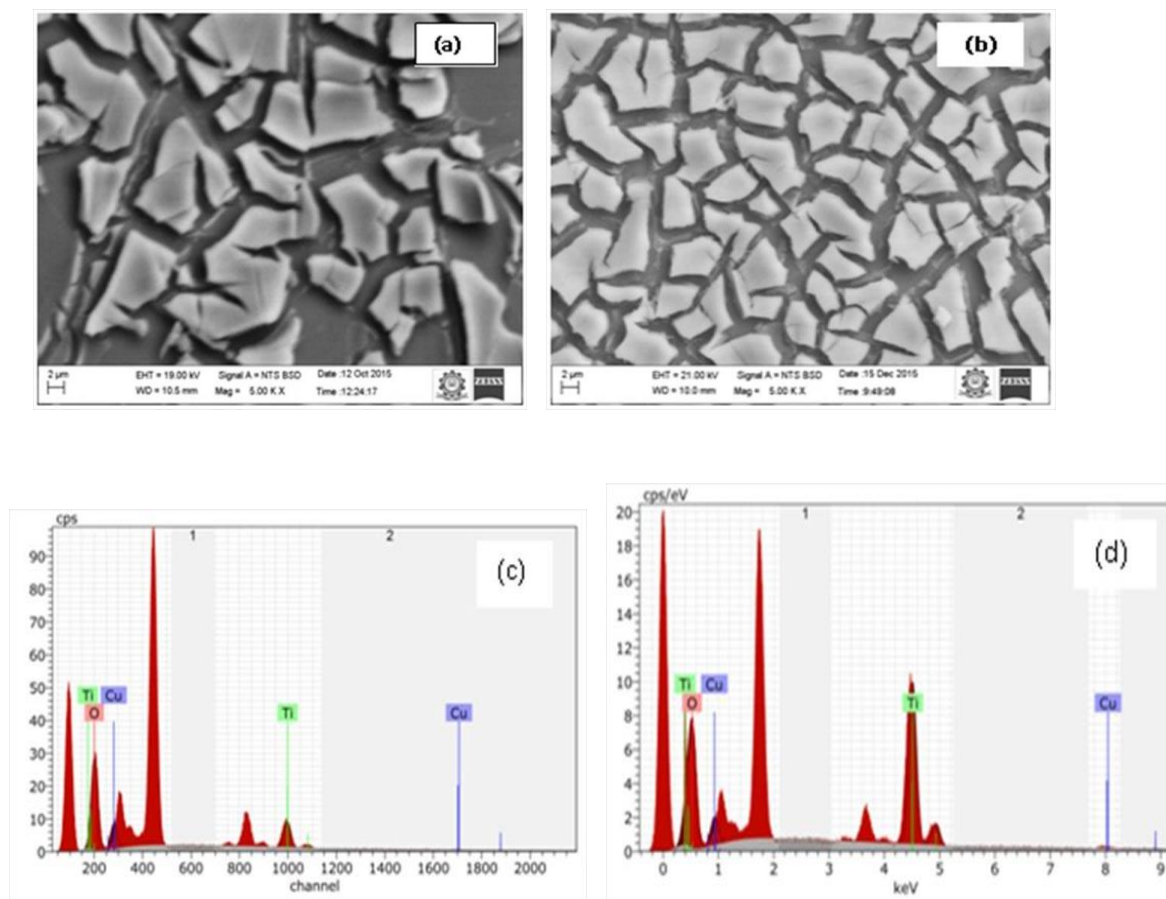


Figure 3: SEM images for (a) 5 (b) 7 coating cycles with EDAX spectrum for (c) 5 (d) 7 coating cycles of Cu-TiO₂ thin films

From the morphological image it is observed that the prepared Cu-TiO₂ thin films were agglomerated, irregular grain size and island like structure. Increase in coating cycle results in nucleation over growth and the film surface observed to be closely packed. The surface composition of the films was identified by EDAX measurement. The EDAX results are shown in figure c and d which demonstrates the presence of Ti, O and Cu in the spectrum.

Surface topography

Atomic force microscopy (AFM) images (2D and 3D) of Cu doped TiO₂ thin film deposited on glass substrate for 3 coating cycles are illustrated in figure 4(a) and 4(b) respectively. Figure (4a) shows the uneven distribution of spherical shaped grains over the surface and (4b) shows mountain and valley like nanostructure in some places. The surface roughness and root mean square values are about 1.69 nm and 3.21 nm respectively. The lower roughness value represents the homogeneity of the TiO₂ particles on the surface [18].

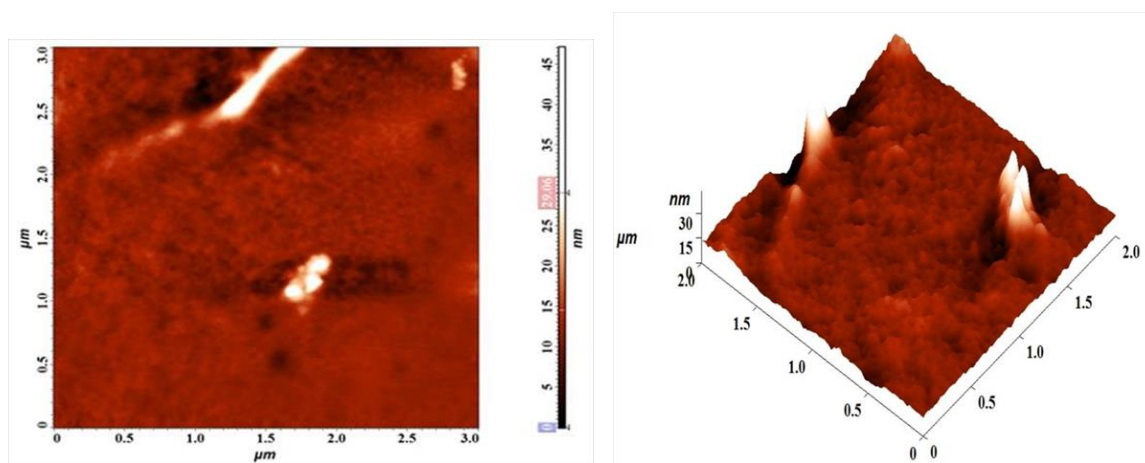


Figure: 4(a) AFM 2D and 4(b) 3D image of Cu-TiO₂ thin films for 3 coating cycles

Optical Analysis

The UV-Visible transmittance spectra of Cu-TiO₂ thin films for different number of coating cycles are shown in figure 5.

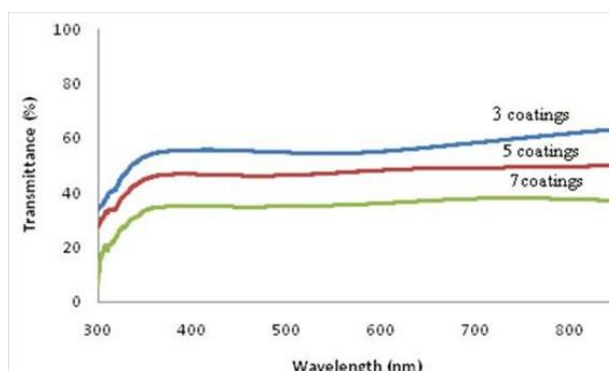


Figure 5: Transmittance spectra of Cu-TiO₂ thin films for different number of coating cycles

From UV-Visible plots, it is observed that the optical transmittance is found to decrease with increase of film thickness. The transmittance in the visible region was observed to be maximum for the film with three coating cycles. The transmittance found to decrease at about 350 nm for all the Cu-TiO₂ thin film and approaches to zero at around 300 nm. This decrease in transmittance is due to absorption of light caused by the excitation and migration of electrons from the valence band to the conduction band of TiO₂ [19].

The band gap energy (E_g) can be estimated from the optical absorption measurements. The band gap value can be obtained from the optical absorption spectra by using Tauc's relation

$$\alpha hv = A(hv - E_g)^n \quad (4)$$

Where A is a constant related to the effective masses associated with the bands and $n = \frac{1}{2}$ for direct transition and $n = 2$ for indirect transition, α is the absorption coefficient, $h\nu$ is the incident photon energy and E_g is the optical band gap. The plot of $(\alpha h\nu)^2$ with photon energy ($h\nu$) is shown in Figure 6. The optical band gap is obtained by extrapolating the linear portion of the plot $(\alpha h\nu)^2$ versus $h\nu$ to $\alpha = 0$. The direct and indirect band gap of Cu-TiO₂ thin films for different number of coating cycles are shown in figure 6(a) and 6(b) respectively.

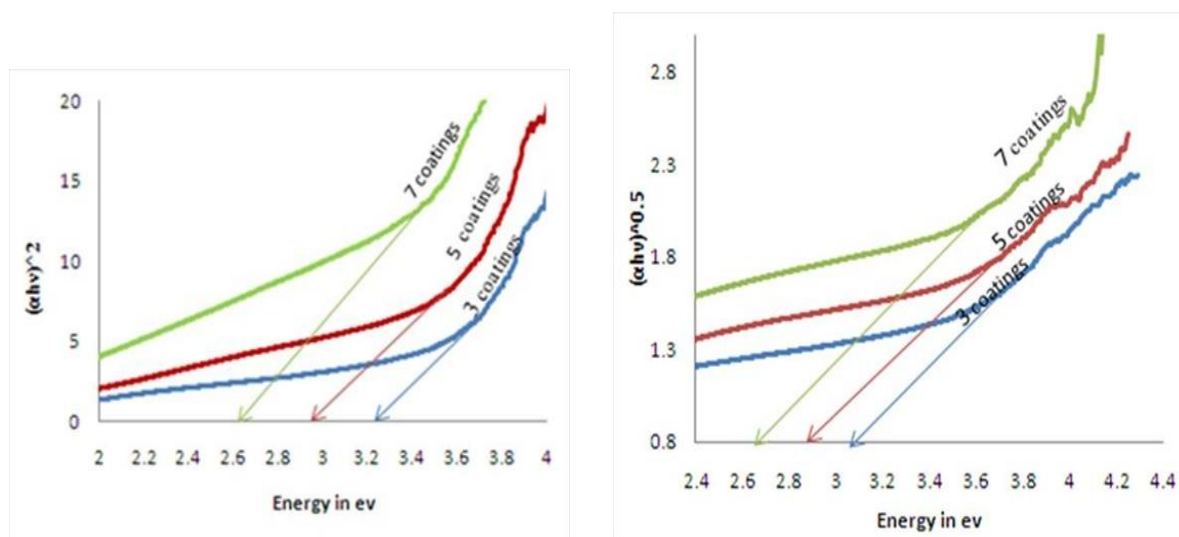


Figure 6: (a) Direct and (b) Indirect bandgap of Cu-TiO₂ thin films for different number of coating cycles

The direct and indirect band gap energy values of the Cu-TiO₂ thin films (Table. 2) are found to decrease with increase in number of coating cycles which might be the result of the change in film density and increase in crystal size. Similar results have been shown by earlier literature malliga et.al, [20].

The extinction coefficient (K) and refractive index (n) of Cu-TiO₂ thin film has been calculated from

$$k = \frac{\alpha\lambda}{4\pi} \quad (5)$$

$$n = \left(\frac{1+R}{1-R} \right) + \sqrt{\frac{4R}{(1-R)^2} - K^2} \quad (6)$$

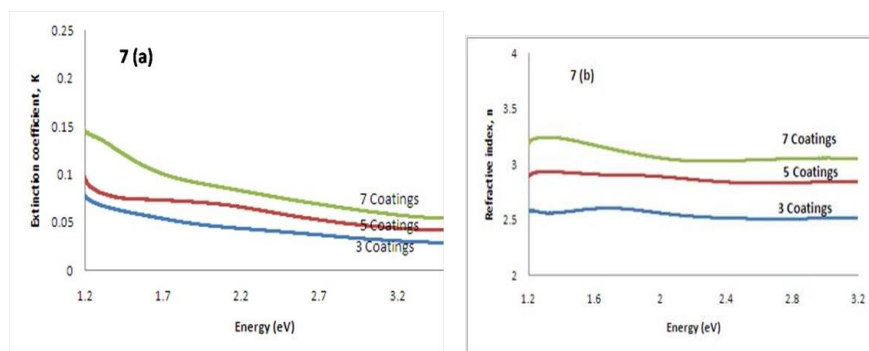


Figure 7: (a) Extinction coefficient and (b) Refractive index vs Energy of Cu-TiO₂ thin films for different number of coating cycles

From the figure, it is observed that the extinction coefficient increases with increase in coating cycle and this due to increase in absorption. The refractive index of the films also increases with respect to coating cycle. The value of refractive index of different coating cycles is in the range of 2.5 to 3.1 which is higher than bulk anatase due to thickness of the film [21].

Table 2: Optical Data of Cu-TiO₂ Thin Films

Coating cycles	Direct bandgap (eV)	Indirect bandgap (eV)	Transmittance (%)
3	3.2	3.0	60
5	3.0	2.8	45
7	2.8	2.6	35

Photoluminescence Analysis

The most valuable information on the quality and purity of the films may be obtained from PL spectra. The PL spectra of Cu-TiO₂ thin films for different coating cycles at room temperature with excitation wavelength of 410 nm is shown in figure 8. Each PL spectra is characterized by three emission bands. A blue emission with a peak centered at around 486 nm (2.6 eV) can be attributed to indirect recombination via defect states with the interaction of phonons in TiO₂ lattice. The peak at 545 nm (2.2 eV) corresponds to TiO₂ anatase phase. In general, it has been observed that the transparency in the films adversely affects their PL response [20].

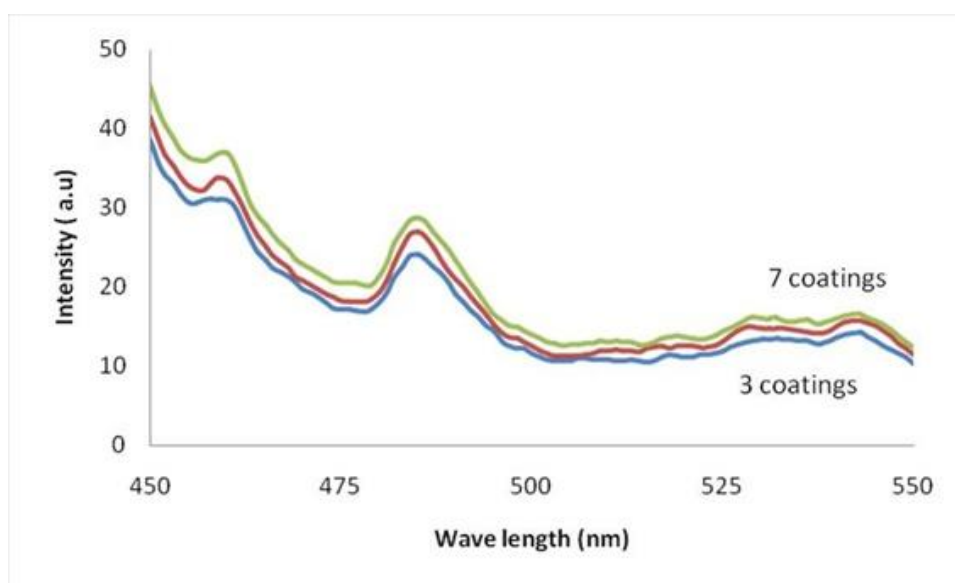


Figure 8: PL spectra of Cu-TiO₂ thin films for different number of coating cycles

Conclusion

Cu-TiO₂ thin films have been deposited onto glass substrates using sol-gel spin coating technique with different coating cycles. X-ray diffraction analysis revealed that the prepared films have tetragonal crystal structure with preferential orientation along (1 0 1) plane. It was also observed that the crystallite size increases but dislocation density and strain decreases with increasing number of coatings due to increase in film thickness. Surface morphology shows that the films are with irregular grains with flake like morphology. EDAX spectra confirms the presence of Ti, O and Cu. Optical study revealed that the transmittance and optical band gap (both direct and indirect) decrease but PL band emission intensity increases

with increase in number of coating cycles. These results confirm that varying coating cycles has strong effect on structural & optical properties of Cu-TiO₂ thin films and high potential application in photo catalytic activities.

References

- [1] O. Carp, C. L. Huisman and A. Reller, “Photo induced reactivity of titanium dioxide”, *Prog. Solid State Ch.* 32 (1-2), 33-177, 2004
- [2] G. R. Dey, “Chemical reduction of CO₂ to different products during photocatalytic reaction on TiO₂ under diverse conditions: An overview”, *J. Nat. Gas Chem.* 16(3), 217-226, 2007
- [3] K. Kořc’ı, L. Obalov’ a and Z. Lacn’ y “Photocatalytic reduction of CO₂ over TiO₂ based catalysts”, *Chem. Pap.* 62(1), 1-9, 2008
- [4] Weerachai Sangchay, Lek Sikong, Kalayanee Kooptarnond and Walailak, “The Photocatalytic and Antibacterial Activity of Cu-Doped TiO₂ Thin Films”, *J Sci & Tech*, 10(1) 19-27, 2013
- [5] S S Roy, A H Bhuiyan,” Optical Characterization of Synthesized Pure and Copper Doped Titanium Oxide Thin Films” *ARNP J. Sci. & Technology*, 5(8), 2015
- [6] Bhattacharyya K, Varma S, Tripathi AK, Bharadwaj SR, Tyagi AK: Effect of vanadia doping and its oxidation state on the photocatalytic activity of TiO₂ for gas-phase oxidation of ethene. *J. Phys Chem C* 2008
- [7] Arana J, Dona-Rodriguez JM, Gonzalez-Diaz O, Rendon ET, Melian JAH, Colon G, Navio JA, Pena JP: Gas-phase ethanol photocatalytic degradation study with TiO₂ doped with Fe, Pd and Cu. *J Mol Catal A: Chem*, 215:153-160, 2004
- [8] Li W, Wang Y, Lin H, Shah SI, Huang CP, Doren DJ, Rykov SA, Chen JG, Barteau MA: Band gap tailoring of Nd₃-doped TiO₂ nanoparticles. *Appl Phys Lett*, 83:4143-4145, 2003
- [9] B. Zhu, Q. Guo, X. Huang, S. Wang, S. Zhang, S. Wu and W. Huang, “Characterization and catalytic performance of TiO₂ nanotubes-supported gold and copper particles”, *Mol. Catal. A: Chem.* 249(1-2), 211-217 2006
- [10] L. S. Yoong, F. K. Chong and B. K. Dutta, “Development of copper-doped TiO₂ photocatalyst for hydrogen production under visible light”, *Energy*. 34 (10), 1652-1661, 2009
- [11] B. Xin, P. Wang, D. Ding, J. Liu, Z. Ren and H. Fu, “Effect of surface species on Cu-TiO₂ photocatalytic activity”, *Appl. Surf. Sci.* 254(9), 2569-2574, 2008



- [12] Hongfu Sun, Chengyu Wang, Shihong Pang, Xiping Li, Ying Tao, Huajuan Tang and Ming Liu, "Photocatalytic TiO₂ films prepared by chemical vapor deposition at atmosphere pressure", *J. non-crystalline solids*", 354, pp.1440-1443, 2008
- [13] S. S. Roy, J. Podder, "Synthesis and optical characterization of pure and Cu doped SnO₂ thin films deposited by spray pyrolysis", *JOAM*, Vol. 12, pp.1479 -1484, 2010
- [14] M. Sreedhar, Neelakanta Reddy, Parthasarathi Bera, D. Ramachandran, K. Gobi Saravanan, Arul Maximus Rabel, C. Anandan, P. Kuppusami and J. Brijitta, "Cu/TiO₂ thin films prepared by reactive RF magnetron sputtering", *Applied Physics A*, 120, pp. 765-773, 2015
- [15] M.J. Alam and D. C. Cameron, "Characterization of Transparent Conductive ITO Thin Films Deposited on Titanium Dioxide Film by a Sol-gel Process", *Surface and Coatings Technology*, 14, pp. 776-780, 2001
- [16] R.Vidhya, M.Sankareswari and K.Neyvasagam," Effect of annealing temperature on structural and optical properties of Cu-TiO₂ thin film", *Int. J. Technical Res. & Applications*, Special Issue 37, PP. 42-46, 2016
- [17] Saranya Amirtharajan, Pandiarajan Jeyaprakash, Jeyakumaran Natarajan and Prithivikumaran Nataraja," Electrical investigation of TiO₂ thin films coated on glass and silicon substrates -effect of UV and visible light illumination", *Appl Nanosci*, 2015
- [18] Suzana segota, Lidija curkovic, Davor Ijubas and Nenad tomasic, Synthesis, characterization and photocatalytic properties of sol-gel TiO₂ films, *Ceramic International*, 10.034, 2010
- [19] A.K.M. Muaz, U. Hashim, K.L.Thong, and Wei-wen Liu, "Effect of annealing temperatures on the morphology, optical and electrical properties of TiO₂ thin films synthesized by the sol-gel method and deposited on Al/TiO₂/SiO₂/p-Si", *Microsyst Technol.*, 2015
- [20] P. Malliga, J. Pandiarajan, N. Prithivikumaran and K. Neyvasagam, "Influence of film thickness on structural and optical properties of sol-gel spin coated TiO₂ thin film", *J Appl Phys*, vol 6, pp 22-28, 2014
- [21] V. Ramya, K. Neyvasagam, R. Chandramohan, S. Valanarasu and A. Milton Franklin Benil, " Studies on chemical bath deposited CuO thin films for solar cells application", *J. Mater Sci: Mater Electron*, 26, pp 8489-8496, 2015



**Synthesis and characterization of L-ALANINE DOPED GLYCINE Lithium chloride
CRYSTALS GROWN by solution method**

D.Jencylin NavaRani ^{*1}, P.Selvarajan², S.Lincy Mary Ponmani¹ and N.Balasundari³

¹Department of Physics, Sarah Tucker College, Tirunelveli, Tamilnadu, India.

²Department of Physics, Aditanar College of Arts and Science, Tiruchendur, India

³Department of Physics, Sri K.G.S.Arts College, Srivaikundam, Tamilnadu,India.

*Corresponding Author Email Id: david_jency@yahoo.co.in

Abstract

Nonlinear optical (NLO) crystals can be classified into organic, inorganic and semi organic materials. L-alanine doped glycine lithium chloride crystal is a semi-organic material and it was grown using water as the solvent by slow evaporation at room temperature. Colourless crystals of well-defined morphology were grown in a growth period of 20 days. The solubility of the material was measured. The grown crystals were characterized by powder X-ray diffraction analysis and FT-IR analysis. Also UV-Vis spectral studies, dielectric studies and microhardness measurement of the grown crystals were carried out.

Keywords: NLO, GG, Gamma-glycine

Introduction

γ -glycine single crystals have been grown using additives such as potassium chloride, sodium chloride, potassium bromide, ammonium chloride, phosphorous acid, lithium nitrate, magnesium chloride, cadmium chloride etc . In this work, γ -glycine (GG) crystals have been grown using lithium chloride as the additive and to modify the various properties of gamma-glycine, L-alanine is added as dopant. Single crystals of undoped and doped gamma-glycine was grown by solution method with slow evaporation technique at room temperature (31°C). The grown crystals were characterized to analyze the structural, spectral, mechanical, electrical properties and other properties and the obtained results are presented.

Materials and Methods

Sample preparation

Single crystals of gamma-glycine (γ -glycine) was grown by taking AR grade glycine and lithium chloride in 1:1 molar ratio. Initially, the aqueous solution of lithium chloride was prepared and the calculated amount of glycine was added into it. By adding more double distilled water and by stirring using a hot plate magnetic stirrer, saturated solution was prepared and this solution was filtered using high a quality filter paper. Then the filtered solution was allowed for slow evaporation to obtain the crystals. It took about 20 days to get single crystals of gamma-glycine (GG). The sample was re-crystallized again to improve the purity. To grow L-alanine doped gamma-glycine crystals, 1 mole%, 2 mole% and 3 mole% of L-alanine were added into the solutions of gamma-glycine and single crystals were obtained by slow evaporation technique. The grown crystals are displayed in the figure 1. It is observed that all the grown crystals are transparent, colourless and non-hygroscopic.



(i)



(iii)

Figure 1: The grown crystals: i) 1 mole% of L-alanine doped gamma-glycine crystal, ii) 2 mole% of L-alanine doped gamma-glycine crystal

Measurement of solubility

The solubility is the amount of solute present in 100 ml of saturated solution at a particular temperature and it is measured by gravimetric method. The solubility curves for the pure and L-alanine doped gamma-glycine are presented in the figure 2. It is observed from the results that the solubility values decrease when L-alanine is added as the dopant into gamma-glycine crystals and as the concentration of these dopant increase in the host crystals, the solubility is found to decrease.

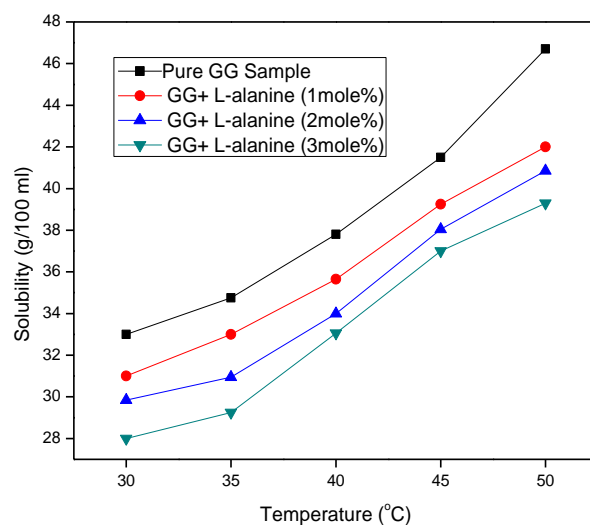


Figure 2: Solubility curves for undoped and L-alanine doped gamma-glycine crystals.

Characterization techniques

X-ray diffraction (XRD) provides an efficient and practical method for the structural characterization of crystals and the molecular structure, atomic coordinates, bond lengths, bond angles, molecular orientation and packing of molecules in single crystals can be determined by X-ray crystallography. The grown crystals were subjected to the single crystal XRD method to estimate the lattice parameters by employing a Bruker-Nonious MACH3/CAD4 single X-ray diffractometer with Mo K α radiation ($\lambda=0.71073 \text{ \AA}$). The optical transmission spectrum of the samples was recorded in the 190- 1100 nm region using a Perkin Elmer UV-vis-NIR spectrometer (model-Lambda 35).

For this study, an optically polished single crystal of thickness 2mm was used. In the present study, microhardness measurements were done using a Vickers microhardness indenter (Leitz Weitzier hardness tester). Hardness test provides useful information on the strength and deformation characteristics of materials. The Vickers microhardness number was calculated using the relation $H_v = 1.8544 P/d^2 \text{ kg/mm}^2$, where P is the applied load and d, the diagonal length of indentation impression. Dielectric constant and dielectric loss values of crystalline samples were measured using a two probe arrangement and an LCR meter.

Results and Discussion

XRD studies for identification of crystal structure

From the Single crystal x-ray diffraction study, it is noticed that all the grown undoped and doped crystals of gamma-glycine crystallize in hexagonal crystal structure. The unit cell dimensions obtained by single crystal XRD studies for the sample are shown in the table 1. The diffraction data shows a very good match with the data reported in the literature and slight changes in the values of lattice parameters have been noticed for L-alanine doped gamma-glycine samples compared to pure gamma-glycine crystal.

Table 1: Unit cell constants of undoped and doped gamma-glycine crystals

Crystal	Axial dimensions (Å)	Angular parameters (degrees)	Unit cell volume Å ³
Undoped gamma-glycine (GG)	a= b=7.023 (2) c=5.4780(1)	$\alpha=\beta= 90^\circ$ $\gamma =120^\circ$	234.04
GG crystal doped with 1 mole % of L-alanine	a=b=7.092(4) c=5.501(2)	$\alpha=\beta= 90^\circ$ $\gamma =120^\circ$	239..82
GG crystal doped with 2 mole % of L-alanine	a=b=7.102(3) c=5.507(6)	$\alpha=\beta= 90^\circ$ $\gamma =120^\circ$	240.41
GG crystal doped with 3 mole % of L-alanine	a=b=7.111(3) c=5.510(1)	$\alpha=\beta= 90^\circ$ $\gamma =120^\circ$	241.29

Powder XRD studies for the grown crystals were carried out and the recorded XRD patterns are given in the figures 3 . The sharp diffraction peaks in the patterns indicate the percentage of crystallinity is high. The diffraction peaks were indexed using the indexing software package and the obtained Miller indices (hkl values) were compared with the standard chart (JCPDS file No. 06-0230).. The powder XRD data for the samples are given in the tables 2. The unit cell parameters obtained from powder XRD diffraction method are observed to be almost the same with the data obtained from single crystal XRD method.

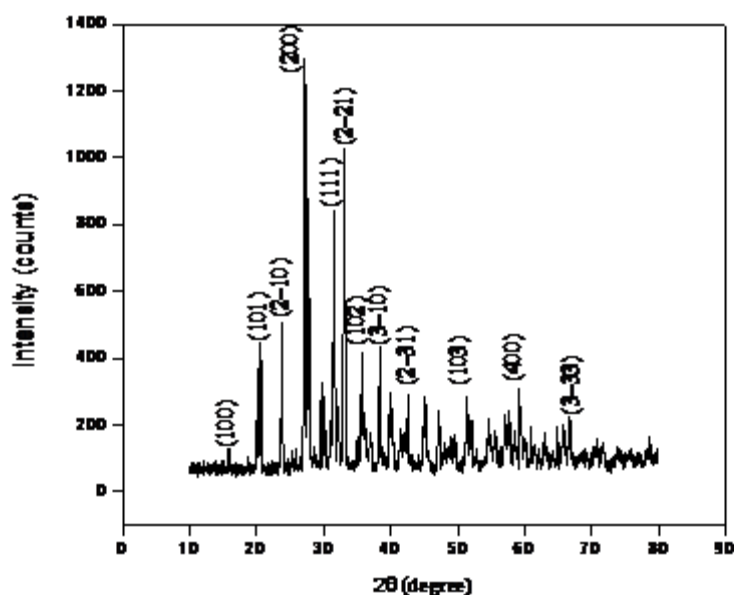


Figure 3: Powder X-ray diffractogram for GG crystal doped with 1 mole% of L-alanine

Table 2: Values of 2-theta, interplanar distance, Miller indices and relative intensity for GG sample doped with 1 mole % of L-alanine

S.No.	2 θ (degrees)	d (Å)	Hkl	I/I _{max} (%)
1	21.672	4.097	101	37.93
2	25.092	3.546	2-10	43.1
3	29.053	3.070	200	100
4	29.957	2.980	111	67.2
5	33.390	2.681	2-21	70.6
6	35.745	2.509	102	36.2
7	38.758	2.321	3-10	37.9
8	42.220	2.138	2-31	27.5
9	52.013	1.756	103	27.5
10	60.220	1.535	400	31.0
11	68.665	1.365	3-33	24.1

Critical nucleation parameters

Nucleation kinetic studies were performed for the grown crystals of undoped and doped gamma-glycine using a constant temperature bath (CTB). From these studies, the data of

critical nucleation parameters were obtained and these data will be useful to understand the nucleation phenomena that are taking place in the supersaturated solutions of samples. The plots of induction period versus supersaturation ratio for undoped gamma-glycine (GG), GG sample doped with L-alanine is presented in the figures 4. From the results one can understand that the induction period decreases with supersaturation ratio values and the induction period is observed to be increased when gamma-glycine is doped with L-alanine.

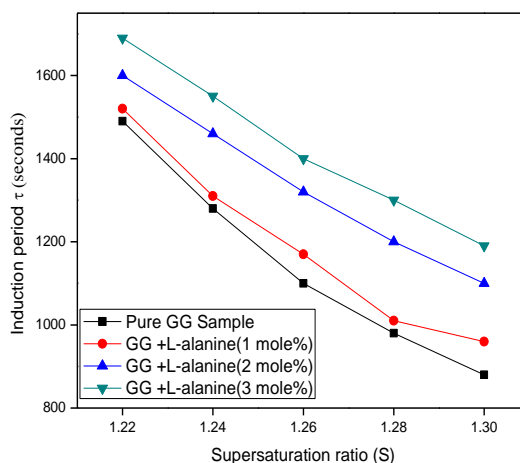


Figure 4: Plots of induction period versus supersaturation ratio for gamma-glycine samples doped with L-alanine

Dielectric studies

The grown crystals were cut, polished and subjected to the measurement of dielectric constant and loss factor. The lower the dielectric loss the more effective is a dielectric material. The dielectric loss angle is an important parameter both for the material of a dielectric and an insulated portion. The plots of dielectric constant (ϵ_r) and dielectric loss factor ($\tan \delta$) versus log of frequency for the samples at different temperatures such as 30, 50 and 80 °C are presented in the figure 5. The variations of AC conductivity with temperature for the undoped and doped gamma-glycine crystals are shown in the figures 6. The AC conductivity of the grown crystals increases with increase in temperature. When the temperature of the crystals is increased, there is a possibility of weakening of hydrogen bond and this results in an enhanced conductivity.

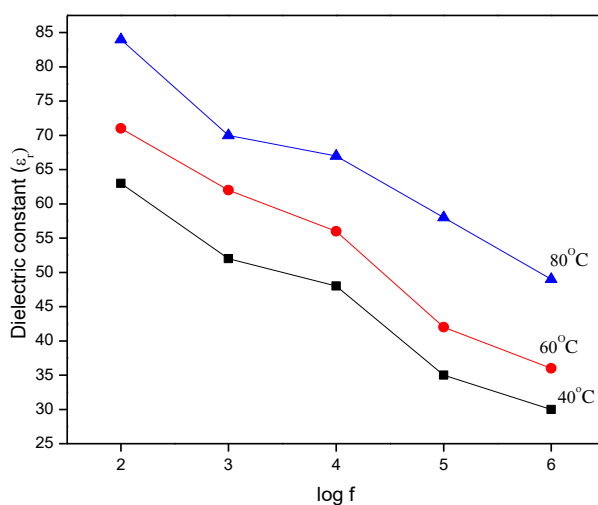


Figure 5: Variation of dielectric constant with frequency for 1 mole% of L-alanine added gamma-glycine crystal at different temperatures

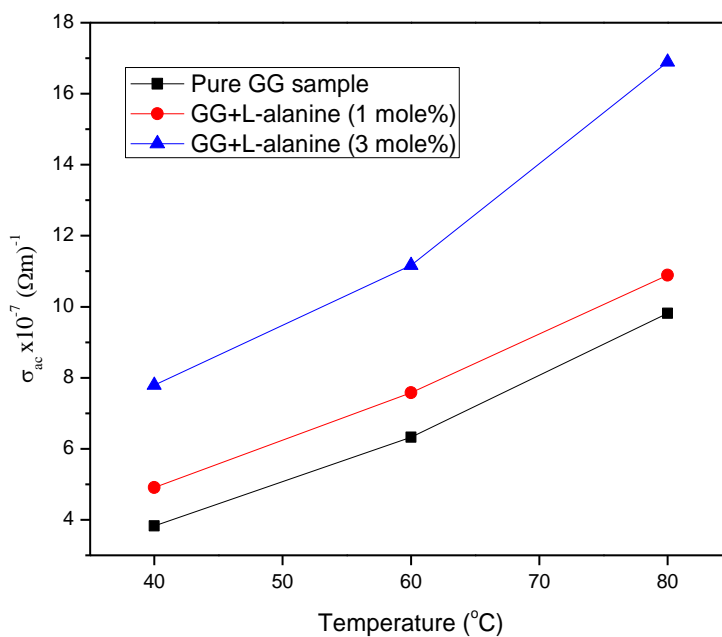


Figure 6: Temperature dependence of AC conductivity for undoped and L-alanine doped gamma-glycine crystals at 103 Hz

Fourier transform infrared (FTIR) spectroscopic studies

Functional groups and the molecular structure of compounds can be identified using the infrared spectroscopy. The higher-energy near-IR, approximately $14000\text{--}4000\text{ cm}^{-1}$ can excite overtones and harmonic vibrations. The mid-infrared, approximately $4000\text{--}400\text{ cm}^{-1}$ may be used to study the fundamental vibrations and associated rotational-vibrational structure. The recorded FTIR spectra of the samples are shown in the figures 7. The assignments for absorption bands of infrared spectra were given in accordance with the data reported in the literature . The broad envelope in the higher wavenumber region between 3200 and 2400 cm^{-1} was due to hydrogen interaction with other atoms such as N–H stretching of NH_2 and C–H of CH_2 stretching. The bands observed at 501 , 606 and 683 cm^{-1} are attributed to carboxylate groups while the peaks absorbed at 1491 and 556 cm^{-1} are attributed to NH_3 group. Thus, the carboxyl group is present as carboxylate ion and amino group exists as ammonium ion in gamma-glycine. The peak observed at 1040 cm^{-1} is assigned to C–C–N stretching vibration. The band at 606 cm^{-1} is due to the wagging vibration of COO^- structure. The bending vibration of CH group appears at 927 cm^{-1} in the spectrum. The peak at 1385 cm^{-1} is assigned to CH_2 twisting vibration. The peak around 2885 corresponds to CH stretching. The presence of carboxylate and ammonium ion clearly indicates that the glycine molecule exists in zwitter ionic form in gamma-glycine crystal. It is observed that the absorption peaks/bands are shifted slightly and some bands are narrowed or broadened when the dopants are added into the lattice of gamma-glycine crystals.

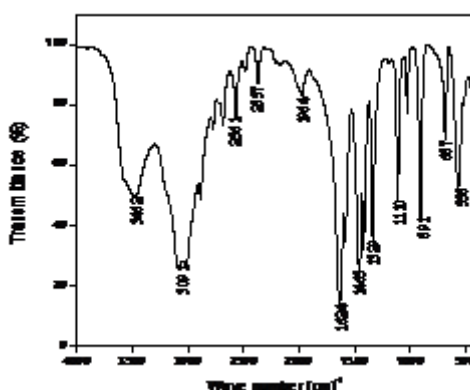


Figure 7: FTIR spectrum of 1 mole% of L-alanine doped gamma-glycine sample

Microhardness, Stiffness constant and Yield strength

The mechanical strength of crystals was tested by carrying out microhardness studies by applying different low loads. The traces of Vickers hardness number with a load for the undoped gamma-glycine and doped gamma-glycine crystals are shown in the figures 8. The results show that the hardness increases when gamma-glycine (GG) is doped with L-alanine. The presence dopant in the lattice of GG may be strengthening the bonds and hence the microhardness increases.

The values of slope are the work hardening coefficient or Mayer's index for the samples and they are given in the table 3. It is known that if the value of n is less than 1.6, the material will be hard category of materials and hence the L-alanine doped gamma-glycine crystals are found to be more harder than undoped (pure) gamma-glycine crystal.

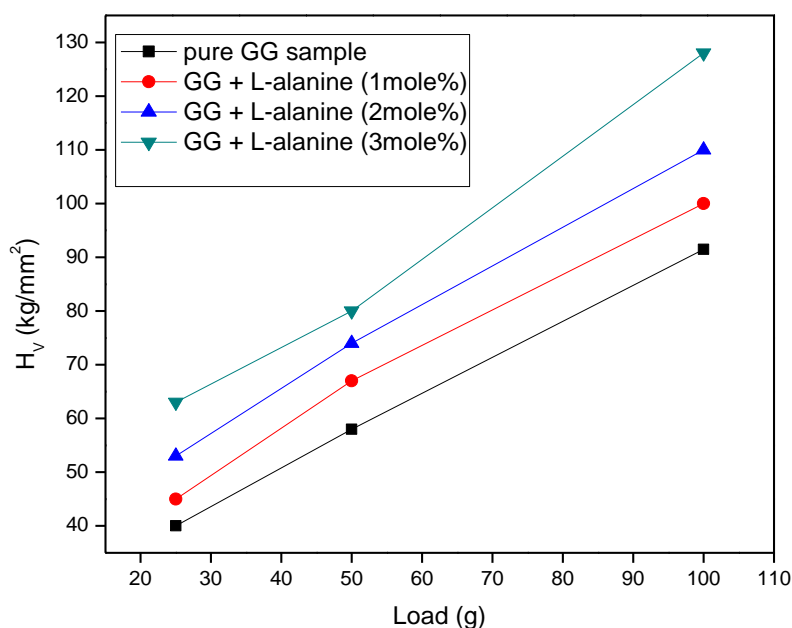


Figure 8: Dependence of hardness number with applied load for pure and L-alanine doped gamma-glycine crystals

Table 3. Values of work hardening coefficient (n) for the samples of L-alanine gamma-glycine

Sample	Work hardening coefficient(n)
Pure Gamma glycine(GG)	5.175
GG +L-alanine (1mole%)	5.083
GG +L-alanine (2mole%)	4.324
GG +L-alanine (3mole%)	3.914

Determination of transmittance, optical band gap, extinction coefficient and refractive index

Optical transmittance and transparency cut-off wavelength and other linear optical parameters are important for single crystals mainly used in optical applications. The grown crystals were cut and polished and the specimen 1.5 mm thick was subjected to transmission measurements using a spectrophotometer in the spectral region of 200–1100 nm. The recorded transmittance spectra of the samples are presented in the figures 9. From the transmittance spectra it is evident that the grown crystals of undoped, and L-alanine doped gamma-glycine crystals have UV lower cut-off wavelength and the transparency in the entire visible region and it suggests that the crystals are suitable for second harmonic generation. The calculated band gap values are given in the table 4.

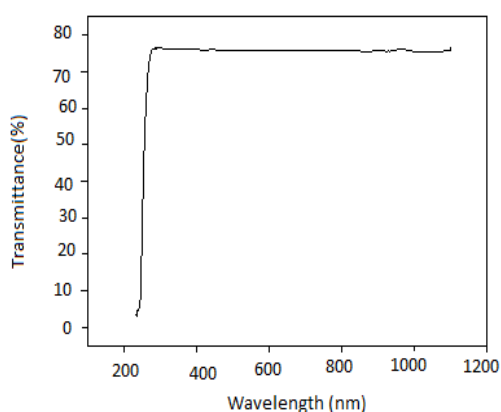


Figure 9: Transmittance spectrum of gamma-glycine crystal doped with 1 mole% of L-alanine

Table.4. Band gap values for Undoped and doped gamma-glycine

Sample	Band gap (eV)
Undoped gamma-glycine	5.62
Gamma-glycine + 1 mole% of L-alanine	5.12
Gamma-glycine + 3 mole% of L-alanine	4.95

Conclusion

Pure gamma glycine and L-alanine doped gamma glycine were synthesized and solubility studies were carried out. Single crystals of un doped and L-alanine doped gamma-glycine grown by slow evaporation technique. Single crystal XRD study reveals the hexagonal structure of the grown crystals. The band gap of both the samples of this work is found. The mechanical property of the grown crystals was studied by micro hardness test and it is noticed that there is an increase in hardness when gamma glycine crystal is doped with l-alanine. The dielectric property also effectively studied.

Acknowledgement

The authors thank the staff members of St.Joseph's college, Trichy for helping us to take microhardness data UVvisible spectral and FTIR data. The supports extended in the research by Crecent Engineering College, Chennai

References

- T.P. Srinivasan, R. Indirajith, R. Gopalakirhnan, J. Crystal Growth 318 (2011) 762
- J. Zaccaro, J. Matic, A.S. Myerson, B.A. Garetz, Cryst. Growth Des.1 (2001) 5
- K. Allen, R.J. Davey, E. Ferrari, C. Towler, G.J. Tiddy, Cryst.Growth Des. 2 (2002) 523
- C.S. Towler, R.J. Davey, R.W. Lancaster, C.J. Price, J. Am. Chem.Soc. 126 (2004) 13347
- T. Balakrishnan, R. Ramesh Babu, K. Ramamurthi, Spectrochim. Acta Part A69 (2008)114



B. Narayana Moolya, A. Jayarama, M.R. Sureshkumar, S.M. Dharmaprakash, J. Crystal Growth 280 (2005) 581

J. Uma, V. Rajendran, Optik 125 (2014) 816

Sd. Zulifiqar Ali Ahamed, G.R. Dillip , P. Raghavaiah , K. Mallikarjuna, B. Deva Prasad Raju, Arab.J. Chem. (2013) 6, 429

M. Esthaku Peter, P. Ramasamy Spectrochimica Acta Part A 75 (2010) 1417

S.Govinda, K.V.Rao, Phys. Status Solidi 27 (1975) 639

B.Tareev, Physics of dielectric materials, Mir Publishers, Moscow (1979)





Investigation on the nucleation kinetics of urea doped Bis glycine picrate

N.Balasundari¹, P.Selvarajan², S.Lincy Ponmani³ and D.JencylineNavarani³

¹Department of Physics, Sri KGS College of Arts and Science, Srivaikundam, India.

²Department of Physics, Aditanar College of Arts and Science, Tiruchendur, India.

³Department of Physics, Sarah Tucker College, Tirunelveli, India.

*Corresponding Author Email Id: enbalasundari@yahoo.co.in

Abstract

The present communication deals with the nucleation kinetics of urea doped Bis glycine picrate (BGP). Induction period and interfacial energy have been determined for the aqueous solution growth of urea doped BGP. It is observed that the induction period decreases as the supersaturation ratio increases and hence the nucleation rate increases. The solubility of urea doped BGP crystal has been estimated at different temperatures. It is observed that, BGP has a positive temperature coefficient of solubility. Nucleation parameters such as radius of the critical nucleus, number of molecules in the critical nucleus and critical free energy change have also been investigated.

Keywords: Nucleation kinetics; Induction period; Interfacial energy; solubility; BGP; doping

Introduction

Crystals of amino acid family have been grown and studied by several researchers for their excellent nonlinear optical (NLO) properties. The study of amino acid crystallizes with other organic and inorganic molecules, which presents a high non-linear optical coefficient has gained much attention in the last few years because of the possibility of using them in technological devices. Picric acid forms stable picrates with various organic molecules like glycine through π bonding or ionic bonding. BisGlycine picrate (BGP) is an organic nonlinear optical material that belongs to monoclinic crystal system and the lattice parameters are $a =$

14.968 Å, $b = 6.722$ Å, $c = 15.165$ Å and $\beta = 93.65^\circ$. Influence of urea on the morphology, growth rate and the characteristics of BGP have been reported in our earlier investigation. In the present study, the nucleation parameters such as interfacial energy, volume free energy and critical free energy change were evaluated numerically using the experimentally determined induction period for urea doped BGP.

Material synthesis and purification

The BGP was synthesized by reacting the aqueous solutions of high purity glycine and picric acid in the molar ratio of 2:1 with double distilled water as the solvent. The reactants were thoroughly dissolved in double distilled water and stirred well using a temperature controlled magnetic stirrer to yield a homogeneous mixture of solution. Then the solution was heated until the synthesized salt of pure Bisglycine picrate was obtained. Calculated amount of urea of 0.5, 1 and 1.5 mole % were added to the solution of Bisglycine picrate to obtain urea-doped Bisglycine picrate salt. The purity of the synthesized salts was further improved by repeating the recrystallization process.

Experimental procedure

The solution growth method is widely used and best suited for growing good quality single crystals with well faceted morphology. Solubility measurements are an essential pre-requisite for the success of the solution growth technique. Solubility studies were carried out in an aqueous solution by gravimetric method. The solubility of pure BGP was determined by dissolving the solute in water. The solution was kept in a constant temperature bath maintained at 30 °C (accuracy ± 0.01 °C) and continuously stirred using a motorized magnetic stirrer.

It is done to have uniform temperature and concentration throughout the volume of the solution. After attaining saturation, the equilibrium concentration of the solute was analyzed gravimetrically. The same process was repeated for the urea doped BGP. Solubility diagrams for undoped (pure) and urea doped BGP salts at various temperatures ranging from 30 °C to 50 °C are presented in the figure 1.

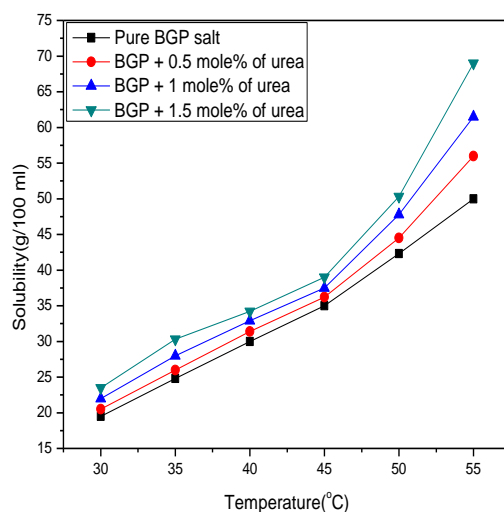


Figure 1: Solubility diagram for pure and urea doped BGP crystals

The saturated solution of pure and urea doped BGP were prepared using the solubility data for the nucleation experiments. The induction period was measured experimentally at different supersaturations by employing the isothermal method. In this method, 50 ml of saturated solution of BGP in an aqueous solution of 1.1 supersaturation ratio was prepared in accordance with pre determined solubility at 303 K. The prepared saturated solution was placed in the constant temperature water bath. The temperature of the bath was raised a few degrees above the saturated temperature to dissolve the excess solute that remained undissolved. The bath temperature was lowered to 303 K and a stop clock was started as soon as the solution reached 303 K, when the nucleation formed inside the solution a bright glitter was observed. The total time elapsed between supersaturation and the appearance of a nucleus of detectable size was taken as the induction period (τ). The time required for the growth of the critical nucleus to a detectable size was negligibly small, compared with the time needed between the attainment of supersaturation and the appearance of a nucleus of detectable size. Hence this can be taken as induction period. The appearance of the first speck of the nucleus was seen at the bottom of the container. This process was repeated for calculating the induction periods for different supersaturation ratios (1.13, 1.16, 1.2). The same process was repeated for the urea doped BGP and the obtained results were plotted as a function of supersaturation as shown in Fig. 2. The induction period decreased as the supersaturation increases. The measured induction period values were used to estimate the interfacial tension values.

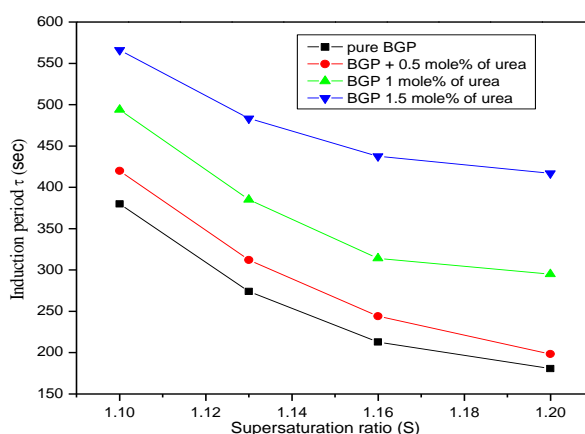


Figure 2. Plot of induction period (τ) vs Supersaturation ratio (S)

Nucleation kinetics

The classical nucleation theory states that the energy required to form the nuclei (spherical) is given as ,

$$\Delta G = \frac{4}{3}\pi r^3 \Delta G_V + 4\pi r^2 \sigma \quad (1)$$

where ΔG_V is the energy change per unit volume, ' σ ' is the interfacial tension and 'r' is the radius of the nucleus. The first term in Eq. (1) represents the formation of a new surface and the second term represents the differences in the chemical potential between the crystalline phase and the surrounding mother liquor. Fluctuation in the supersaturated solution causes the formation of a small cluster of molecules known as embryos. The driving force for the nucleation from the saturated solution is given as,

$$\Delta G_V = \frac{kT \ln S}{V} \quad (2)$$

where ΔG_V is the volume free energy change, V is the specific volume of the solute molecule and k is the Boltzmann's constant. In the critical state, the free energy formation obeys the condition

$d(\Delta G_V)/dr = 0$. Hence, the critical radius and the Gibbs critical free energy barrier for nucleation can be expressed as;

$$r^* = \frac{2\sigma V}{kT \ln S} \quad (3)$$

Here k is the Boltzmann's constant, T is the absolute temperature, S is the supersaturation ratio

$$\Delta G^* = \frac{mRT}{N_A (\ln S)^2} \quad (4)$$

The rate of nucleation (i.e., the number of nuclei formed per unit time per unit volume) can be expressed by an Arrhenius-type equation

$$J = A \exp\left(\frac{-\Delta G^*}{kT}\right) \quad (5)$$

where A is the pre-exponential factor

(approximately $A = 1 \times 10^{30}$ for solution),

The number of molecules in the critical nucleus is expressed by

$$n = \frac{4\pi r^{*3}}{3V} \quad (6)$$

According to the classical theory of homogenous nucleation(14), the induction period (τ) is related to the interfacial tension (σ) as follows

$$\ln \tau = -\ln B + \frac{16\pi\sigma^3 N_A^3 V^2}{3R^3 T^3 (\ln S)^2} \quad (7)$$

$$k = \frac{R}{N_A}$$

where B is a constant, R is the universal gas constant and N_A is the Avogadro's number and τ the induction period at temperature T and supersaturation ratio S. A plot of $1/(\ln S)^2$ against $\ln(\tau)$ (fig 3) from Eq. (6) is a straight line and the intercept on the Y-axis gives the value of $\ln B$. The slope is given as,

$$m = \frac{16\pi\sigma^3 N_A^3 V^2}{3R^3 T^3} \quad (8)$$

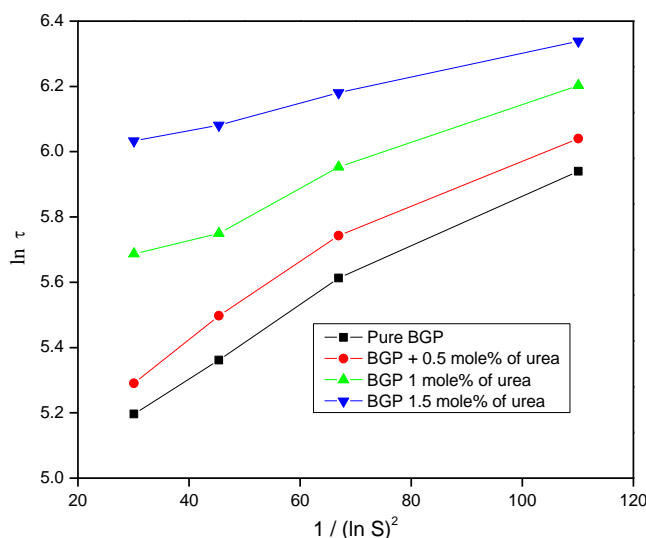


Figure.3. Plot of $1/(\ln S)^2$ vs $\ln(\tau)$.

Results and discussion

The solubility of Pure and urea doped BGP crystals as a function of temperature is shown in Fig. 1. From the graph, it is observed that solubility of the samples in water increases with temperature and it is found to be more for urea doped BGP than the pure BGP. Since the solubility increases with temperature, the samples have positive temperature coefficient of solubility. Fig.2 shows the induction period as a function of supersaturation ratio at constant temperature. The value of τ decreases and hence the nucleation rate increases as the supersaturated concentration of the aqueous solution is increased. It can be noticed that the induction period increases with increase in additive concentration of urea. The study of induction period against supersaturation gives an idea of optimized induction period in order to have a controlled nucleation rate to grow good quality single crystals.

Table 1: Summary of critical nucleation parameters for pure and urea doped BGP samples

Sample	S	$\Delta G^* \times 10^{-20}$ (joules)	$J \times 10^{29}$ nuclei/s /volume	$r^* \times 10^{-10}$ m	N
Pure BGP	1.1	0.429	3.608	12.6	21.47
	1.13	0.261	5.378	9.82	10.10
	1.16	0.177	6.567	8.08	5.66
	1.2	0.117	7.573	6.58	3.05
BGP + 0.5 mole% of urea	1.1	0.425	3.643	12.5	21.12
	1.13	0.258	5.417	9.76	10.05
	1.16	0.175	6.598	8.04	5.62
	1.2	0.116	7.591	6.54	3.025
BGP + 1 mole% of urea	1.1	0.308	4.810	11.2	15.41
	1.13	0.187	6.412	8.72	7.27
	1.16	0.127	7.395	7.18	4.06
	1.2	0.084	8.186	5.85	2.19
BGP + 1.5 mole% of urea	1.1	0.179	6.535	9.32	8.97
	1.13	0.109	7.718	7.27	4.258
	1.16	0.074	8.387	5.98	2.37
	1.2	0.049	8.901	4.87	1.28

The interfacial tension has been calculated at constant temperature (room temperature) for pure BGP and various mole percentage of urea doped TGS crystals from the graph (fig.3) drawn

between $\ln \tau$ and $1/(\ln S)^2$. The calculated values of interfacial tension vary from 6.473 to 6.661 mJ/m². Using the interfacial tension value, the nucleation parameters such as radius of critical nucleus (r^*), Gibbs free energy change (ΔG^*) and number of molecules (n) in the critical nucleus have been calculated for the controlled nucleation condition and the results are summarized in the Table 1. It is noted from Table 1 that the value of r^* decreases with the increase of supersaturation and consequently the nucleation rate (J) increases with increase of supersaturation. That means the number of critical nuclei formed will be increased which will lead to spurious nucleation. Also it was observed that the values of n and ΔG^* decrease with the increase of supersaturation and also these parameters decrease when concentration of urea is increased.

Conclusion

The fundamental nucleation parameters of pure and urea doped BGP crystals were determined on the basis of the classical nucleation theory. The solubility and induction period have been experimentally determined. The interfacial tension was calculated at different supersaturation conditions using the experimentally determined induction period values. The nucleation parameters such as volume free energy, Gibbs critical free energy, radius of critical nucleus and the number of molecules in the critical nucleus were determined using the interfacial tension values.

Acknowledgements

The authors are thankful to the supported work from various research centers such as Regional Research Laboratory (Trivandrum), Crescent Engineering College (Chennai), St Joseph College (Trichy), M.K. University (Madurai) and Cochin University (Cochin).

References

- X. Liu, Z. Wang, G. Zhang, X. Wang, A. Duan, Z. Sun, L. Zhu, D. Xu, J. Cryst. Growth 308 (2007) 130-132.
- Y. Zhang, H. Li, B. Xi, Y. Che, J. Zheng, Mater. Chem. Phys. 108 (2008) 192-195.
- J. Hernandez-Paredes, D. Glossman-Mitnik, H.E. Esparza-Ponce, M.E. Alvarez-Ramos, A. Duarte-Moller, J. Mol. Struct. 875 (2007) 295-301.
- D. Eimerl, S. Velsko, L. Davis, F. Wang, G. Loiacono, G. Kennedy, 25 (1989) 179-193.
- Sachinkumar, Hotam sing choudhari, Chandrabhanseniya. *Chem. Pharm. Res.*, 2011, 3[4]. 854-860



Chandrabhanseniya Sumit sing trivedia, Santoshkumarverma *JChem.Pharm.Res.*, **2011**, 3(6) 330-336

S. Yamaguchi, M. Goto, H. Takayanagi, H. Ogura, *Bull. Chem. Soc. Jpn.* 61 (1988) 1026–1028.

T. Kai, M. Goto, K. Furuhashi, H. Takayanagi, *Anal. Sci.* 10 (1994) 359.

T. Uma Devi, N. Lawrence, R. Ramesh Babu, K. Ramamurthi, *Spectrochim. Acta A* 71 (2008) 340.

N. Balasundari, P. Selvarajan, S. Lincy Mary Ponmani and D. Jencylin *Recent Research in Science and Tech.* 2011, 3(12): 64-67

K. Byrappa, T. Ohachi, “Crystal Growth Technology”, William Andrew Publishing (Springer), Norwich, New York (2003)

N.P. Zaitseva, L.N. Rashkovich, S.V. Bogatyreva, *J. Cryst. Growth* 148 (1995) 276.

A.E. Nielsen, S. Sarig, *J. Cryst. Growth* 8 (1971) 1.

M. Volmer, A. Weber, *phys. chem.* 119(1926)27





Volume: 2; Issue: 3 [Special Issue]; March-2016; pp 411-419. ISSN: 2454-5422

Investigation on structural, spectroscopic and mechanical properties of organic non-linear optical DL-alanine oxalate single crystals

S.Lincy Mary Ponmani^{1*}, P.Selvarajan², D.Jencylin¹ and N.Balasundari³

¹Department of Physics, Sarah Tucker College, Tirunelveli, India.

²Department of Physics, Aditanar College of Arts and Science, Tiruchendur, India.

³Department of Physics, Sri KGS college of Arts and Science, Srivaikundam, India.

*Corresponding Author Email Id [*lincyking@gmail.com](mailto:lincyking@gmail.com)

Abstract

Over recent years, amino acid family crystals have been subjected to extensive investigations by several researchers for their nonlinear optical (NLO) properties. DL-alanine is one among the rare amino acid racemates crystallizing in a noncentro symmetric space group. A new Organic Single crystal of DL-Alanine Oxalate (DLAO) has been grown from solution by slow evaporation technique. Transparent colourless crystals upto 10 mm x 6 mm x 3 mm were obtained. Formation of the new crystal has been confirmed by single crystal XRD and FTIR spectra. The grown crystals have been subjected to powder X-ray diffraction studies to identify the crystalline nature.

Single crystal X-ray diffractometer was utilized to measure unit cell parameters and to confirm the crystal structure. The cell parameters of the grown crystal are identified from single crystal XRD. DLAO belongs to monoclinic system with lattice parameters $a=11.329(3)$ Å, $b=6.583(3)$ Å, $c=12.460(4)$ Å and $\alpha=\gamma=90^\circ$ and $\beta=113.58(2)^\circ$ and volume of the unit cell is $851.6(6)$ Å³. The functional groups are confirmed in vibrational analysis. Mechanical strength



of the grown material is tested by Hardness studies. The value of hardness increases when the applied load is increased.

Keywords : Aminoacid; DL-alanine; Crystal growth; Single crystal; X-ray Diffraction; Crystal structure; Microhardness

Introduction

The organic materials play an important role in second frequency mixing, electro-optical modulation, optical parametric oscillation, optical bi-stability, harmonic generation (SHG) etc. Over recent years, amino acid family crystals have been subjected to extensive investigations by several researchers for their nonlinear optical (NLO) properties. Amino acids and their complexes are the organic or semi-organic materials that have attracted great attention due to their ability in ease of processing in the assembly of optical devices. The complete understanding of the properties of amino acid crystals, as well as other organic crystals, still requires more attention

DL-Alanine is one among the rare amino acid racemates crystallizing in a non-centrosymmetric space group. The structure of DL-alanine was elucidated by Subha Nandini et al. The crystal structure is stabilized by a network of characteristic head-to-tail hydrogen bond sequences. The carboxyl group is present as a carboxylate ion and amino group as ammonium ion. From the literature survey, it is noticed that a limited number of papers are available on DL-alanine complexes.

Experimental studies of DLAO crystal

Growth procedure

DL-alanine oxalate (DLAO) was grown from the aqueous solution using double distilled water by slow solvent evaporation technique. An equimolar amount of DL-alanine and oxalic acid (AR grade) were mixed with sufficiently large amount of water at 50 °C to synthesize DL-alanine oxalate. A saturated solution of 150 ml was taken and the solution was filtered using filter paper. The filtered solution was taken in a beaker, which was tightly closed with a thick filter paper so that the rate of evaporation could be minimized. Good transparent, small single crystals were obtained after 3 weeks and the obtained material were re-crystallized twice in distilled water in order to improve their purity. The recrystallized crystals were used as the seed



to obtain big sized crystals of DL-alanine oxalate. The harvested crystals of DLAO are displayed in the figure 1.

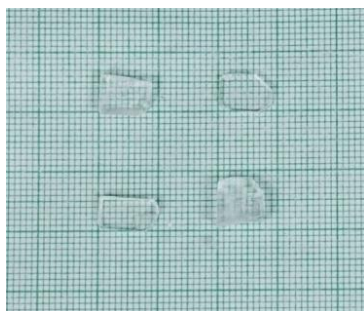


Fig 1: Photograph of DLAO crystals

Solubility measurement

To grow bulk crystals from solution by slow evaporation technique, it is desirable to select a solvent in which it is moderately soluble. It is found that DLAO sample is sparingly soluble in organic solvents like acetone, methanol and ethanol and is reasonably soluble in water. The size of a crystal depends on the amount of material available in the solution, which in turn is decided by the solubility of the material in that solvent. The solubility of DL-alanine oxalate in water was determined by adding a known quantity of solute in solvent maintained at constant temperature till it was completely dissolved. Using this technique, the magnitude of the solubility of DL-alanine oxalate was evaluated at various temperatures viz. 30°C, 40°C, 45°C, 50°C and 55°C. The temperature dependence of solubility of DL-alanine oxalate is shown in figure 2. From the result, it is observed that the solubility increases with temperature. These data can be used for preparing the saturated solution and for carrying out nucleation kinetic studies.

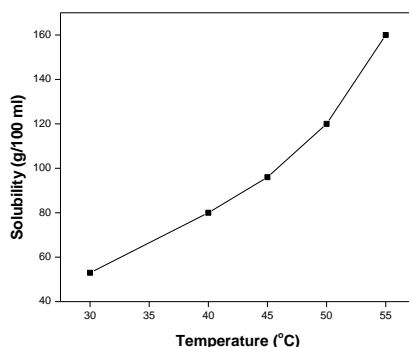


Fig 2: Variation of solubility with temperature for DLAO crystal

Results and Discussion

X-ray diffraction studies

The cell parameters of the grown crystal were obtained using single crystal X-ray diffractometer (Bruker-Nonius MACH3/CAD4). It is observed that the DLAO crystal belongs to monoclinic system with the cell parameters $a=11.329(3)\text{\AA}$, $b=6.583(3)\text{\AA}$, $c=12.460(4)\text{\AA}$ and $\alpha=\gamma=90^\circ$ and $\beta=113.58(2)^\circ$ and volume of the unit cell is $851.6(6)\text{\AA}^3$.

In order to identify the diffraction planes of the crystal of DLAO, the grown sample was subjected to powder X-ray diffraction studies with a high resolution PANalytical X'pert PRO diffractometer. The XRD pattern is shown in figure 3. The reflections of powder XRD pattern were indexed using the INDEXING software package by following the procedure of Lipson and Steeple. The values of 2θ , hkl values and d-values etc. are presented in the table 1.

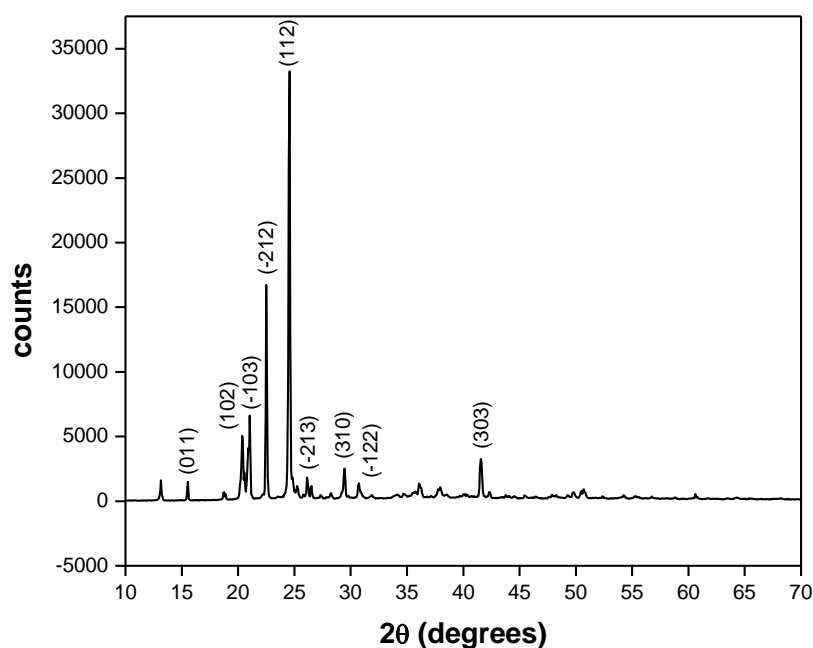


Fig 3: Powder XRD pattern of DLAO crystal

Table 1: The values of 2 θ , hkl values and d-values for DLAO crystal

2θ	d(std)	Hkl
15.55	5.7032	011
20.36	4.3256	102
21.391	4.1506	-103
22.50	3.9571	-212
24.57	3.6150	112
26.51	3.3575	-213
29.45	3.0634	310
30.72	2.9018	-122
41.55	2.1656	303

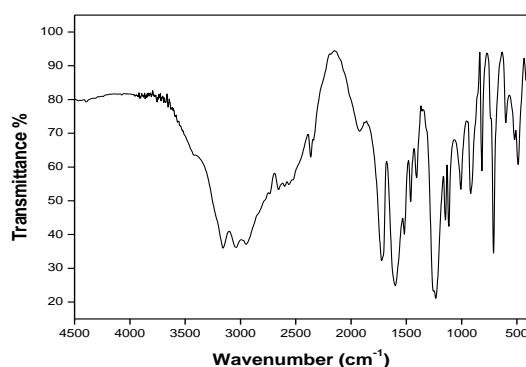
FTIR analysis

The vibrational analysis of the grown crystal was done using FTIR spectrometer. The FTIR spectrum is recorded in the range of 400–4500 cm^{-1} . The recorded spectrum is shown in Fig. 4. In FTIR spectrum, the broad intense peak is observed between 3200–2800 cm^{-1} , which is due to NH_3^+ vibrations. This confirms that the amine group presented in the DL-alanine molecule bonded with oxalic acid through hydrogen bonding. To analyze the FTIR spectrum, the molecular structure of this compound is taken into account. The broad bands around 3039 cm^{-1} and 3157 cm^{-1} correspond to NH stretching vibrations. The peak observed at 2948 cm^{-1} shows CH stretching and that at 1929 cm^{-1} indicates CN stretching. The C=O stretching band observed at 1724 and 1600 cm^{-1} indicate the presence of carboxylic acid group. The CH_3 bending deformation was assigned to the peak at 1460 cm^{-1} . The peak at 1407 cm^{-1} was assigned to symmetrical stretching of the COO^- group. The C-O stretching was assigned to 1006 cm^{-1} . The peaks between 1147 cm^{-1} and 918 cm^{-1} are assigned to asymmetrical coupled vibrations of alanine. In the lower frequency range, the sharp peak observed at 520 cm^{-1} is assigned to COO^- rocking. The assigned vibrational frequencies are given in the table 2.



Table 2: FTIR frequency assignment of pure DLAO crystal

Wavenumber in cm^{-1}	Band assignments
520	COO ⁻ rocking
918	Asymmetric coupled vibrations of alanine
1006	C-O stretching
1147	Asymmetric coupled vibrations of alanine
1407	COO ⁻ symmetrical stretching
1460	CH ₃ bending deformation, O-H symmetric stretching & C-O symmetric stretching
1517	NH ₃ ⁺ symmetric deformation & NH ₂ in-plane deformation
1600	C=O stretching
1724	C=O stretching
1926	C-N stretching
2948	C-H stretching
3039	N-H stretching
3157	N-H stretching

**Fig 4: FTIR spectrum for the grown crystal DLAO**

Mechanical Properties

The mechanical strength of DLAO crystal was checked by carrying out microhardness studies by means of Leitz Vickers microhardness tester. The static indentations were made at room temperature with a constant indentation time of 10 s. The indentation marks were made by varying the load from 25 to 100 g. Vickers microhardness values have been calculated and a graph (Fig.5) is plotted between Vickers hardness number (VHN) and applied load P. It is observed from the graph that the hardness increases as the load increases. The experiment

shows that the crystal of DLAO breaks when a load more than 100 g is applied and this result is not shown in figure 5. The formation of cracks on the surface of the crystal beyond the load 100 g is due to the release of the internal stresses generated locally by indentation. The work hardening coefficient 'n' of the DLAO crystal is 3.67 and it has been determined from the slope of the log P versus log d plot (fig. 6). Since the work hardening coefficient is more than 1.6, this crystal is a soft material and the hardness is low.

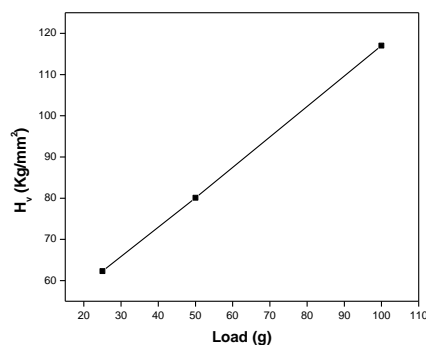


Fig 5: Plot of H_v versus load for DLAO crystal

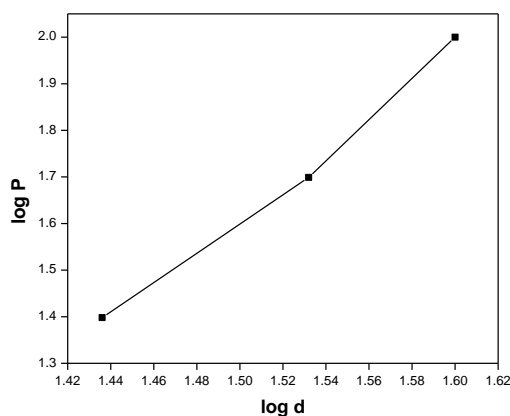


Fig 6: Variation of log P with log d for DLAO crystal

Second Harmonic Generation (SHG) studies

A high density Nd:YAG laser ($\lambda=1064$ nm) with a pulse duration of 6 ns was passed through the powdered sample of the DLAO. The SHG emission was confirmed from the output of the laser beam having the green emission ($\lambda=532$ nm). SHG efficiency of the grown DLAO crystal

is 1.13 times that of the standard KDP crystal. Thus this crystal is a potential material for frequency conversion.

Conclusion

Solubility studies of DL-alanine oxalate (DLAO) sample has been carried out at different temperatures and the single crystal of this sample has been grown from aqueous solution by slow evaporation method. XRD studies reveal that the structure of DLAO crystals is monoclinic. The XRD studies show that the crystalline perfection of the grown crystal is reasonably good. The presence of functional groups in the sample has been confirmed by FTIR analysis. The mechanical strength has been checked for the sample and the work hardening coefficient value has been calculated.

Acknowledgement

The authors are thankful to the authorities of National Institute for Interdisciplinary Science and technology, Papanamcode, Trivandrum, Madurai Kamaraj University, Madurai, and St. Joseph's College (Autonomous), Triuchirappalli for providing instrumental facility for characterization.

References

J. Badan, R. Hierle, A. Perigand, J. Zyss, Am. Chem. Soc. Symp. Ser. 233, in: D.J. Williams (Ed.), Am Chem. Soc., Washington, 1993

M. Kitazawa, R. Higuchi, M. Takahashi, Appl. Phys. Lett. 64 (1994) 2477

L. Misoguti, A.T. Varela, F. D Nunes, V.S. Bagnato, F.E.A. Melo, J. MendesFilho, S.C, Zilio, Opt. Mater. 6 (1994) 147

W.S. Wang, M. D Aggarwal, J. Choi, T. Gebre, A.D. Shield, B.G. Penn, D.O. Frazier, J. Cryst.Growth 198/199 (1999) 578

M. SubhaNandhini, RV. Krishnakumar, K. Sivakumar, S.Natarajan, ActaCrystalogr., E 58 (2002) 307

R.Becker and W.Doring, Ann. Physik, 24 (1935) 719

D.Turnbull and J.C. Fisher, J.Chem.Phys., 17 (1949) 71



H. Lipson, H.Steeple, “Interpretation of X-ray powder Diffraction Patterns”, FifthEd, Macmillan, NewYork (1970)

Ivan Kityk, MalgorzataMakowska-Janusik, Mol. Cryst. Liq. Cryst. 353 (2000) 513

M. Arivanandhana, K. Sankaranarayanan, P. Ramasamy, J. Crystal Growth 31 (2008) 1493

N.TheresitaShanthi, P.Selvarajan, C.K. Mahadevan, Curr. Appl. Physics, 9 (2009) 1155



Volume: 2; Issue: 3 [Special Issue]; March-2016; pp 420-427. ISSN: 2454-5422

Synthesis and characterization of semi organic nonlinear optical material: Ammonium Tartrate Tetra hydrate

S.G.PushpalathaGracelin¹, C.Krishnan² and P.Selvarajan³

¹Department of Physics, Sarah Tucker College, Tirunelveli, India.

²Department of Physics, Aringnar Anna College, Aralvaimozhi, India.

³Department of Physics, Aditanar College of Arts and Science, Tiruchendur, India.

Abstract

A semiorganic non-linear optical crystal of ATT have been grown by slow evaporation technic using water as a solvent. The structural and vibrational properties of the crystals were studied. Fourier transform infrared (FTIR) studies confirm the vibrations of various functional groups present in the grown crystal. The optical transmittance is studied through UV visible spectroscopy. The crystal system and lattice parameters were determined from the crystal X-Ray diffraction analysis. And the solubility of the crystal is determined.

Key words: Semi-organic, non-linear, slow evaporation, X-Ray diffraction.

Introduction

Recent research is focused on semi organic materials due to their large linearity, high damage threshold good mechanical and thermal stability .The present investigation is focused on the growth and characterization of crystal of ATT(ATT) a new semi organic material .The ATT crystals are grown by slow evaporation technique at room temperature.The ATT crystals obtained is subjected to various characterization studies such as XRD,FT-IR and UV-VIS.



Crystal Growth

The calculated amount of ATT salt was first dissolved in 100 ml of deionised water by continuous stirring to get a homogeneous mixture. The saturated solution was then filtered using walt man filter paper to remove the suspended impurities. Then the solution was left undisturbed. The filtered solution was allowed to evaporate slowly at room temperature. Good, optically transparent crystals were harvested in a growth period of three weeks.

Characterization Studies

Single crystal X-ray diffraction analysis of the grown crystal of Ammonium Tartrate Tetra hydrate was carried out using Enraf-Nonius CAD-4 diffractometer using Mo K_{α} radiation to determine the unit cell parameters and space group. Optical studies have been carried out using ELICO SL 218 double beam UV-visible spectrophotometer which records optical spectrum in the wavelength range of 200-1100nm. FTIR absorption spectrum of the grown crystal in the infrared region $4500 - 400 \text{ cm}^{-1}$ was recorded on a spectrometer (Model: SHIMADZU- FTIR-8400S) using a KBr pellet technique. Second Harmonic Generation (SHG) test for the grown crystal was performed by the powder technique of Kurtz and Perry using a pulsed Nd: YAG laser (Model: YG501C, $\lambda = 1064 \text{ nm}$). Smooth, flat surface was selected and subjected to this study on the (001) plane of the crystal.

Results and Discussion

Single Crystal X-ray diffraction analysis

Single crystal X-ray diffraction analysis of the grown crystal of Ammonium Tartrate Tetra hydrate was carried out using Enraf-Nonius CAD-4 diffractometer using Mo K_{α} radiation to determine the unit cell parameters and space group. The analysis of the collected data reveals that the ATT crystal is monoclinic in structure with space group P1 and lattice parameter are $a = 8.9901(\text{\AA})$, $b = 15.5424(\text{\AA})$, $c = 6.2512(\text{\AA})$ $\alpha = \gamma = 90^{\circ}$, $\beta = 101.507^{\circ}$

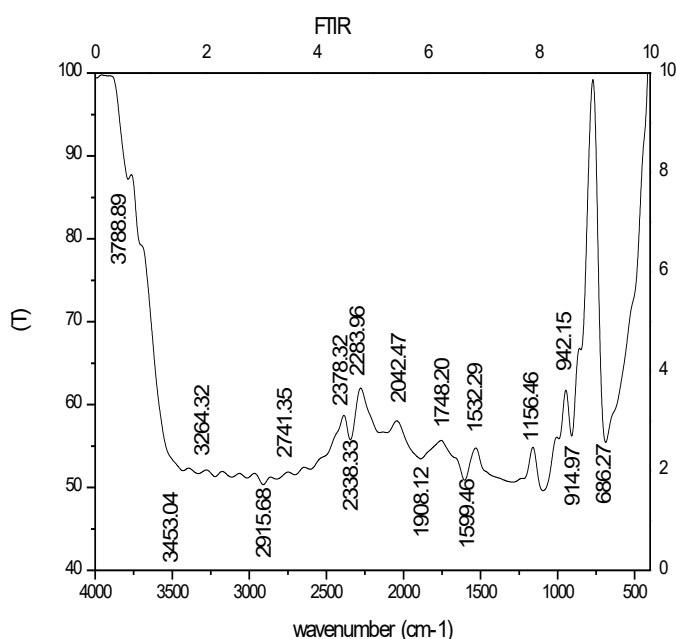
FTIR Spectral analysis

The infrared spectroscopy is effectively used to identify the functional groups of the sample. When infrared radiation interacts with a sample, a portion of the incident radiation is absorbed at a specific wavelengths and the Fourier Transform Infrared (FTIR) absorption



spectrum is a characteristic of functional groups of molecules in a sample. FTIR absorption spectrum of the grown crystal in the infrared region $4500 - 400 \text{ cm}^{-1}$ was recorded on a spectrometer (Model: SHIMADZU- FTIR-8400S) using a KBr pellet technique. The recorded FTIR spectrum of ATT crystal is presented in the figure 1. The present vibrational spectroscopic study was carried out with a view of obtaining an insight into the structural aspects of crystals. The assignments for absorption bands of infrared spectra were given in accordance with the data reported in the literature. The broad envelope in the higher wavenumber region between 3238 and 2700 cm^{-1} was due to hydrogen interaction with other atoms such as N-H stretching of NH_2 and C-H of CH_2 stretching. The bands observed at 539 cm^{-1} are attributed to carboxylate groups while the peaks absorbed at 612 cm^{-1} are attributed to NH_3 group. Thus, the carboxyl group is present as carboxylate ion and amino group exists as ammonium ion in ATT. The peaks observed at 827 cm^{-1} are assigned to C-C-N stretching vibration. The presence of carboxylate and ammonium ion clearly indicates that the ATT molecule exists in zwitter ionic form in ATT crystal. The grown crystals were subjected to FTIR analysis to analyze the presence of functional groups. The observed frequencies and their assignments of ATT crystal are given.

Fig 1 FTIR Graph



Fig(1) FTIR Spectra Of Ammonium Tartrate Tetrahydrate.

Optical properties

To determine the transparency range of the grown ATT crystal, UV-vis transmittance spectrum was recorded and is shown in Fig.2. Optically clear single crystal of thickness 2mm was used for this study. The cut- off wavelength of the crystal occurs at 225 nm. From the figure, it shows that the crystal was optically transparent in the wavelength range from 300 to 1100 nm and it is a feature that promotes possible optical applications in NLO devices. The crystal has sufficient transmission in the visible and IR region. The optical absorption coefficient (α) was determined using following formula $\alpha = ((2.303 \log(1/T))/t)$, where T is the transmittance and t is the thickness of the crystal. Optical transmittance range and transparency cut-off of single crystal are important factors for optical applications. The recorded transmittance spectra of ATT crystals in the wavelength range of 200 – 1200 nm are shown fig (3). Transmittance (T) = % T/100. The wave length is increased, transmittance is also increased. At about 225 nm a sharp fall to zero in the transmittance is observed for ATT sample and the crystal has sufficient transmittance in the entire visible and near IR region. The sharp fall at 225 nm for the sample corresponds to the fundamental absorption edge, which is essential in connection with the theory of electronic. The band gap of ATT is calculated using the formula $E_g = 1240/\lambda_{max}$, it is found to be (4.97) eV.

Fig 2 The wave length versus percentage of transmittance

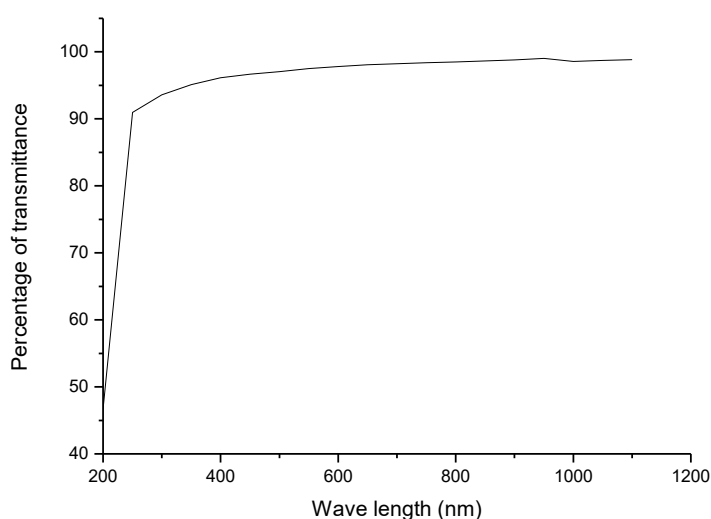


Fig.2 The graph was drawn between wave length versus percentage of T. From the graph increasing the wavelength also increased the percentage of T.

Fig.3 The Wavelength Verses the Absorbance

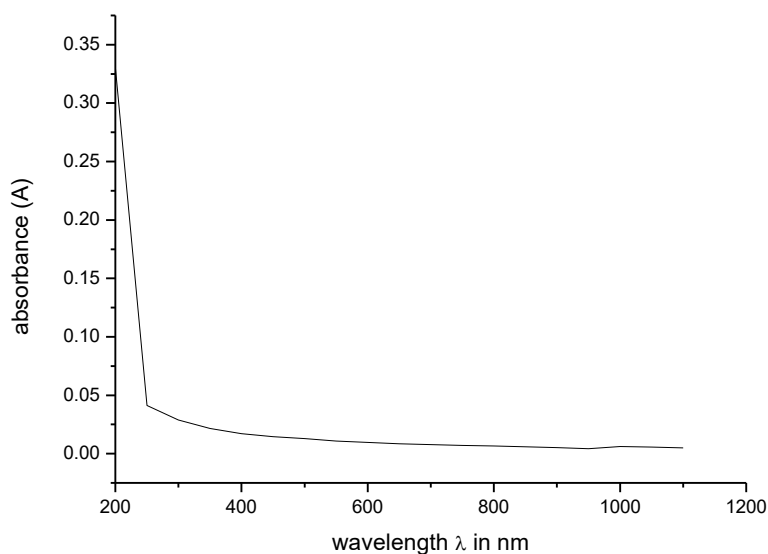
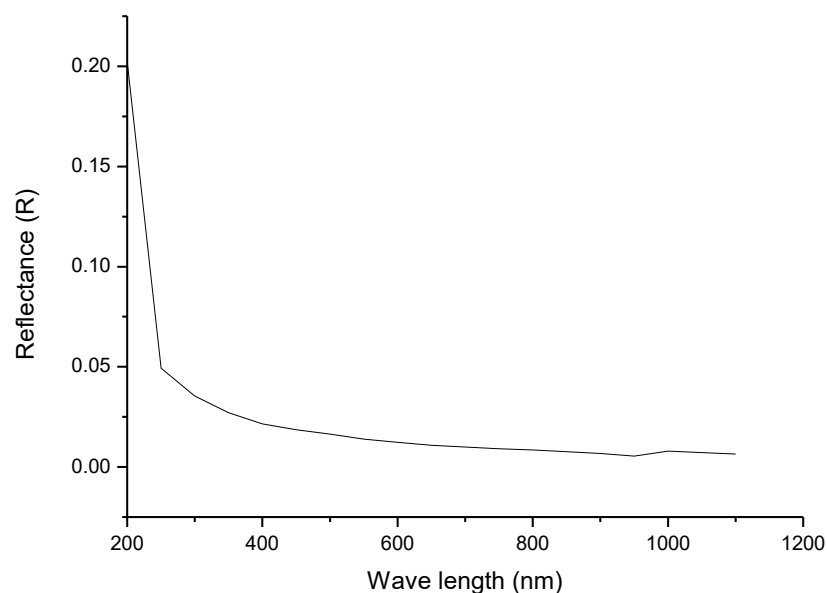


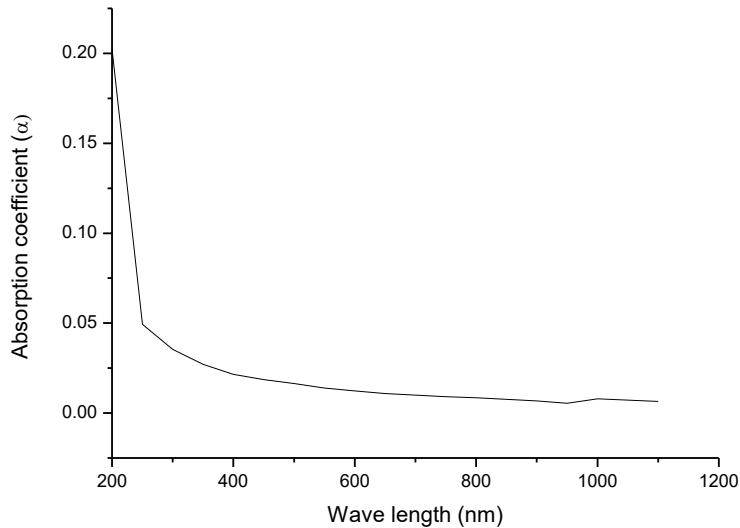
Fig 3 The absorbance wave length is 249nm. The absorbance is decreased, also the wave length is increased.

Fig 4 Wave length versus Reflectance



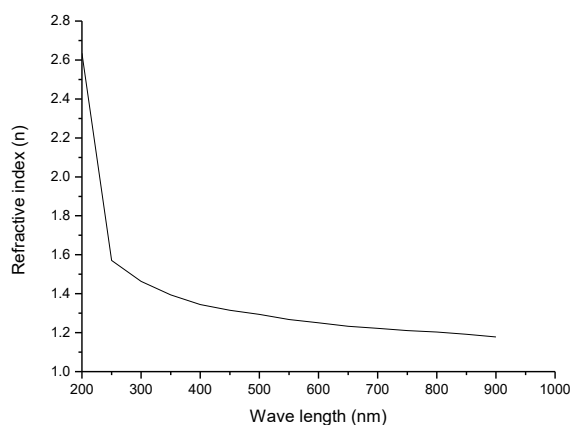
The graph was plotted between Wave length (λ) and Reflection (R) as shown in fig (4). The relation is given by $Reflectance(R) = 1 - (T + A)$. The Reflectance wavelength is 249nm. The reflectance is decreased also the wavelength is increased.

Fig 5 Wave length versus absorption coefficient



The dependence of optical absorption coefficient with the photon energy helps to study the band structure and the type of transition of electrons. The absorbance is decreased; also the wave length is increased.

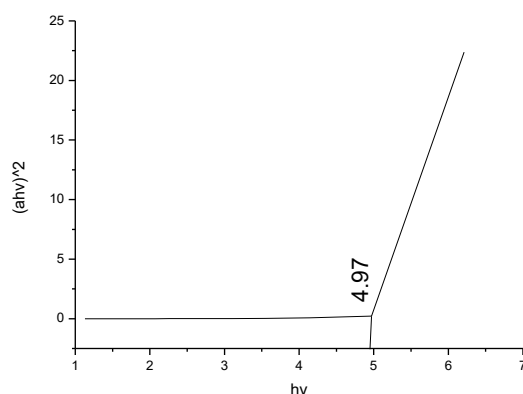
Fig 6 Wave length versus refractive index



The refractive index (n) can be determined from reflectance data using $n = (1 + \sqrt{R}) / (1 - \sqrt{R})$. The plot between wavelength and refractive index (n) of ATT crystal is shown in fig (6). From

the fig (6) it is observed that the refractive index decreases with increasing wavelength. The refractive index (n) of the ATT crystal is 1.57 at 297nm.

Fig 7 Photon of energy versus $(\alpha h\nu)^2$



The plot of variation of $(\alpha h\nu)^2$ versus $h\nu$ is shown in fig (10). This plot is known as the Tauc's plot and it is used to find out the accurate optical band gap value. The band gap was evaluated by the extrapolation of the linear part and the value is found to be 4.97eV. As a consequence of wide bandgap, the grown crystal has large transmittance in the visible region.

Conclusion

Semi organic crystals of ATT was grown from slow evaporation technique. Single crystal X-ray diffraction study shows the crystal belongs to monoclinic crystal system. The FT-IR spectrum confirms the functional groups present in the grown crystal. UV-Visible spectral analysis reveals that ATT crystals are optically transparent in the entire uv-visible range and has transparency of about 90% with a lower cut off wavelength at 225 nm. As ATT crystal have good optical transparency and reasonably good NLO properties, these materials could be potential candidates for NLO applications.

Acknowledgements

The authors are grateful to the managements of Sarah Tucker College, Tirunelveli, Arignar Anna College, Nagercoil and Aditanar College of Arts and Science, Tiruchendur for the encouragement given to us to carry out the research work. Also the authors are thankful to the staff members of St. Joseph's College, Trichy, Cochin University, Cochin, Crescent

Engineering College, Chennai, VIT, Vellore, IIT, Madras, who helped us to carry out the experimental work.

References

G.Albrecht, R.B.Corey, J.Am.Chem. Soc.61 (1939) 1087

E.Ramachandran, K.Baskaran, S. Natarajan Cryst. Res. Technol. 42(2007) 73

K. Srinivasan, J. Arumugam Optical Materials 30 (2007) 40

Y. Iitaka, Acta Crystallogr. 11 (1958) 225

Jan Baran, Henryk Ratajczak, Spectrochimica Acta Part A 61 (2005) 1611

T. Balakrishnan, R. Ramesh Babu, K. Ramamurthi Spectrochimica Acta Part A 69 (2008) 1114

P.Selvarajan , J.Glorium ArulRaj, S.Perumal, J. Crystal Growth 311 (2009) 3835

R.W. Williams J. Molecular Structure (Theochem) 685 (2004) 101

A. Dawson, D.R. Allan, S.A. Belmonte, S.J. Clark, W.I.F. David, P.A.McGregor, S.Parsons, C.R.Pulham, L. Sawyer, Cryst. Growth Des. 5 (2005)1415

Charles J,Pouchert, The Aldrich library of Infrared Spectra, Third Edn., Aldrich Chemical Company,INC,Milwaukee,Wisconsin (1981)

P.Kalsi , Spectroscopy of Organic Compounds, Wiley Eastern, New Delhi(1985)

J.C.Anderson, Dielectrics, Chapman and Hall, London, (1963)

J.B.Birks, J. Hart, Progress in Dielectrics, Heywood, London(1959)

B.Helina, P Selvarajanand A S J Lucia Rose, Phys. Scr. 85 (2012) 055803

1K.V. Rao, A. Samakula, J. Appl. Phys. 36 (1965) 2031

E.M. Onitsch, uber die mikrohartete der metalle, Mikroskopia 2 (1947) 131

S.K. Kurtz, T.T. Perry, J. Appl. Phys. 39 (1968) 3798





Volume: 2; Issue: 3 [Special Issue]; March-2016; pp 428-438. ISSN: 2454-5422

Studies on the Mechanical and Thermal Properties of Sulphamic Acid Doped Glycine NLO Single Crystals

A. Effie Cordelia¹ and S. Perumal²

¹Department of Physics, Sarah Tucker College, Tirunelveli, India.

²Physics Research Centre, S.T. Hindu College, Nagercoil, India.

Abstract

Amino acids contain proton donor carboxylic group and proton acceptor amino group. Thus at favorable pH, the natural amino acids exist as zwitterions with a negatively charged carboxyl group and positively charged amino group. Among these, Glycine ($\text{HN}_2\text{CH}_2\text{COOH}$) is a nonpolar and aliphatic amino acid. It is also the smallest of 20 amino acids commonly found in proteins. It is not chiral and can fit into hydrophilic and hydrophobic environments due to its minimal side chain of only one carbon atom. As doping can alter the physical and chemical properties of crystals, here an attempt was made to dope Glycine crystals with sulphamic acid. The dopant sulphamic acid is a classical inorganic compound which crystallizes in space group P_{bca} , which is centrosymmetric. According to the theoretical concept of SHG, the centrosymmetric crystals do not show SHG. But it was fruitful indeed, as a novel NLO single crystals GSA had been harvested as a result of doping. X-ray diffraction analysis and FTIR spectral analysis had been carried out. Thermal stability, hardness studies, second and third harmonic nonlinear optical studies of the crystals were reported in this work.

Keywords: Single crystal XRD, Powder XRD, FTIR Spectrum, Vicker's microhardness analysis, TG-DTA, SHG efficiency, Third harmonic nonlinear optical parameters

Introduction

Nonlinear optical (NLO) crystals play a major role in the fast developing fields like photonics and opto-electronics. In recent decade, major advances have been made in the development of NLO materials with improved optical, mechanical characteristics and high damage thresholds. Ideal NLO crystals are expected to possess large nonlinear figure of merit for frequency conversion, wide phase matching angle, high laser damage threshold, wide optical transparency, ease of fabrication and high mechanical, thermal and chemical stability. Several NLO single crystals have been grown with Glycine and sulphamic acid separately but this work is a new attempt to dope glycine with sulphamic acid.

Experimental work

AR grade chemicals glycine and sulphamic acid were purchased so as to harvest GSA single crystals. To grow single crystals GSA, 1mole % of sulphamic acid was added with calculated amount of glycine in doubly deionized water and put on magnetic stirrer for four hours to get highly homogeneous mixture of uniform composition. After proper filtration, the solution was left undisturbed in dust free atmosphere. Fine colourless transparent single crystals BASA were obtained after a period of three weeks.

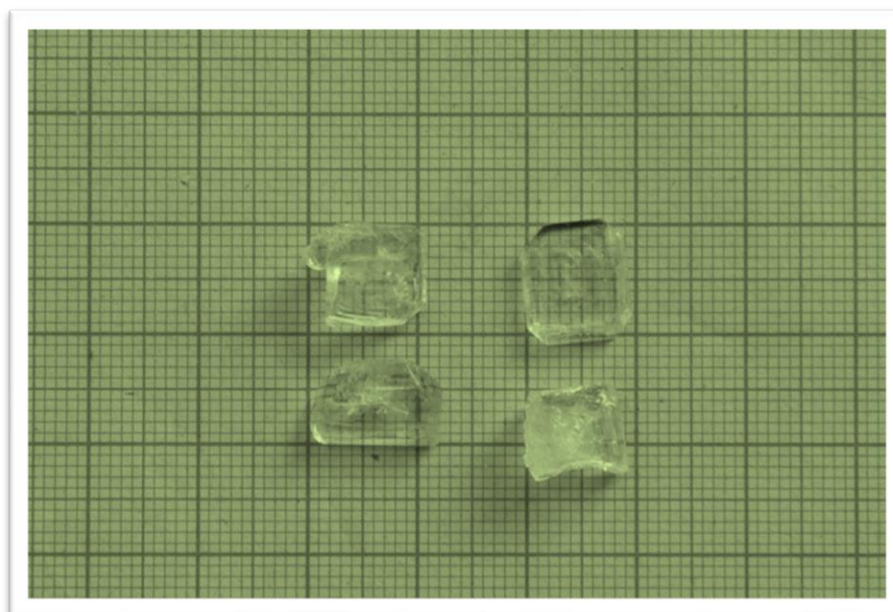


Fig.1 Photograph of the crystal GSA

Results and discussion

Single Crystal XRD analysis

The crystals GSA were analyzed for cell parameter values with computer controlled Bruker-Nonius MACH3/CAD4 single crystal X-ray diffractometer and the obtained results are tabulated as below:

Table 1 Cell parameter values of GSA

Sample	System	a(Å)	b(Å)	c(Å)	V(Å) ³
GSA	Monoclinic	5.14	12.01	5.5	315

For GSA, the value of $\beta = 111.77^\circ$

Powder XRD analysis

Powder XRD patterns of the grown crystals GSA was recorded using BRUKER AXS D8 advance diffractometer with $\text{CuK}\alpha$ ($\lambda=1.5418\text{\AA}$) radiation after crushing the sample into fine powder. The sample was scanned over the range $0-80^\circ$ at the rate of 2 per minute. The patterns are given in fig.2. The unit cell parameters determined from single crystal XRD were used to index the reflecting planes. In the figure, we can notice the appearance of sharp peaks in the diffraction patterns which indicate the good crystalline nature of the grown crystals. The variation in the intensity of diffracted beam at different planes accounts for the incorporation of the dopant sulphamic acid into the host lattice.

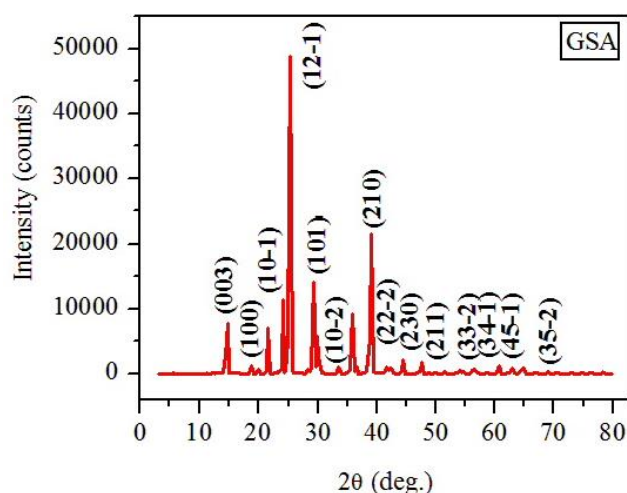
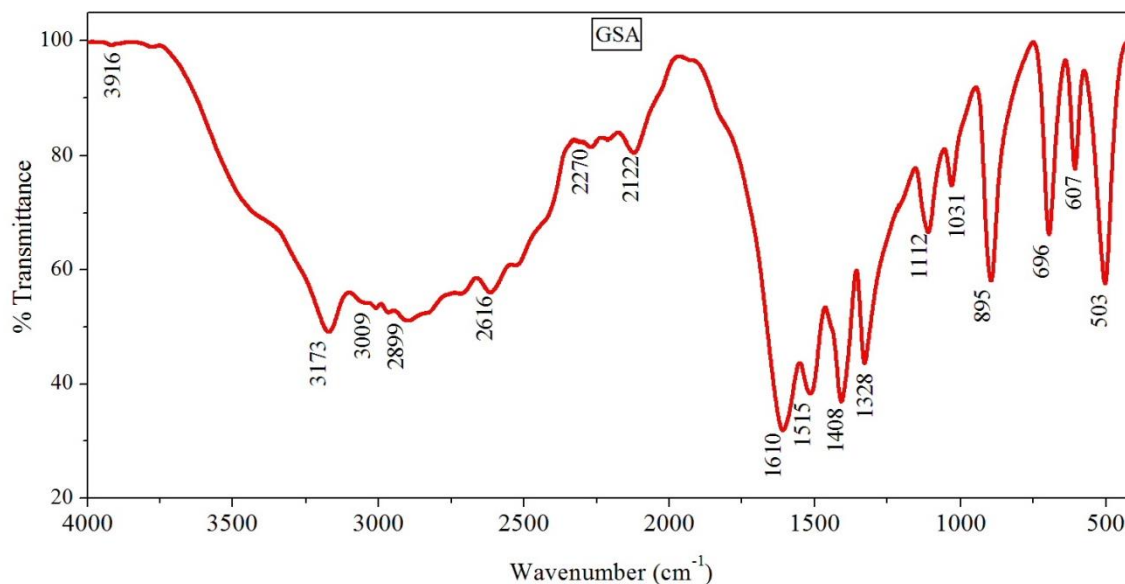


Fig.2 Powder XRD pattern of GSA

Fourier Transform Infrared (FTIR) spectral studies

FTIR absorption spectra of the grown crystals in the infrared region 4000-400 cm^{-1} were recorded on a Lambda 35 spectrophotometer using a KBr pellet technique and it is shown in the figures 3. The absorption bands/peaks and their assignments are given in the table 2.

**Fig.3 FTIR spectrum of GSA****Table 2 Spectral assignments of sample GSA**

Wave number (cm^{-1})	Spectral assignments
3173	NH_3^+ stretching
3009	NH_3^+ stretching
2899	C-H stretching
2616	N-H-O stretching
2270	N-H stretching
2122	Combination band
1610	C=O stretching
1515	N-H bending
1408	COO^- symmetric stretch
1328	CH_2 twisting
1112	C-C stretching
1031	C-C-N stretching
895	$(\text{SO}_4)_2$ stretching
696	N-S stretching
607	COO^- wagging
503	COO^- rocking

Microhardness studies

Measurement of microhardness of a material is a measure of resistance to plastic deformation. It is a mechanical property that is studied by measuring the Vickers microhardness number (H_v) with various loads. The variation of Vicker’s hardness number (H_v) with different loads for GSA crystals were measured using Shimadzu HMV-2T microhardness tester and is presented in Fig.4. and it is noticed that the Vickers hardness number (H_v) increases with the applied load which confirms the reverse indentation size effect.

The graph plotted between $\log d$ and $\log P$ for the crystals GSA are shown in fig.5. The slope of the line gives the Meyer’s index or work hardening coefficient (n). If $n < 1.6$, the material is brought under the category of hard materials. If $n > 1.6$, the material is soft one. Here for GSA, $n = 2.94$. Hence GSA is a soft material.

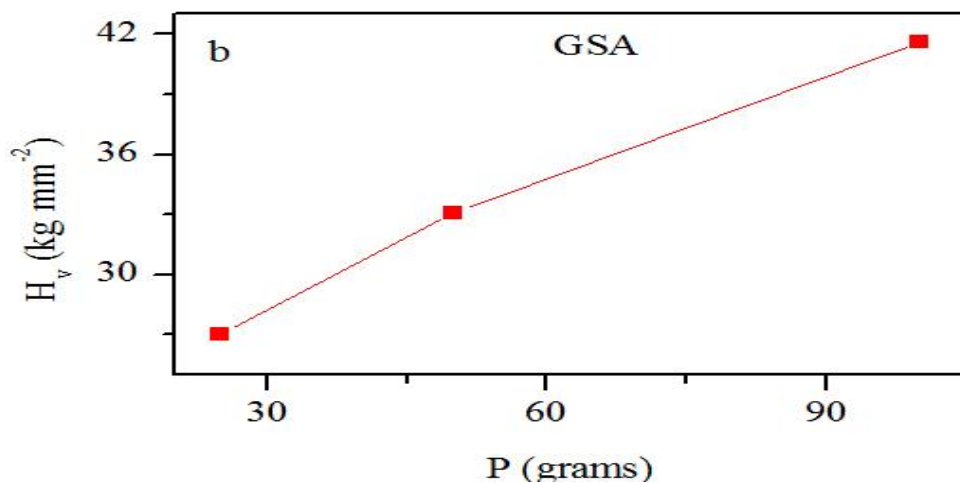


Fig. 4 Variation of H_v with load

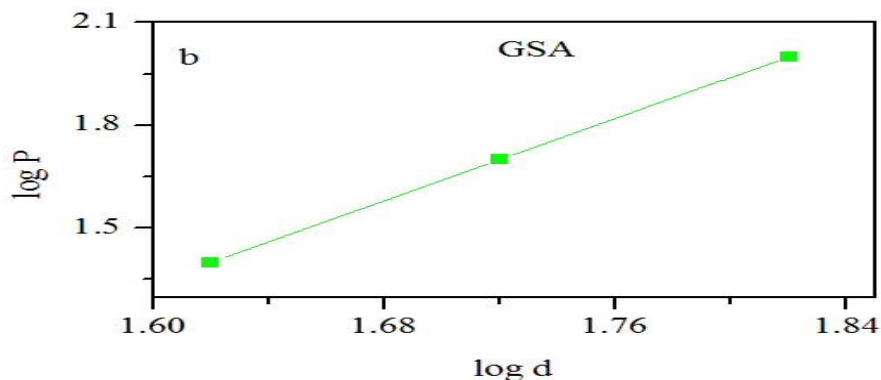


Fig. 5 Graph between $\log d$ and $\log P$

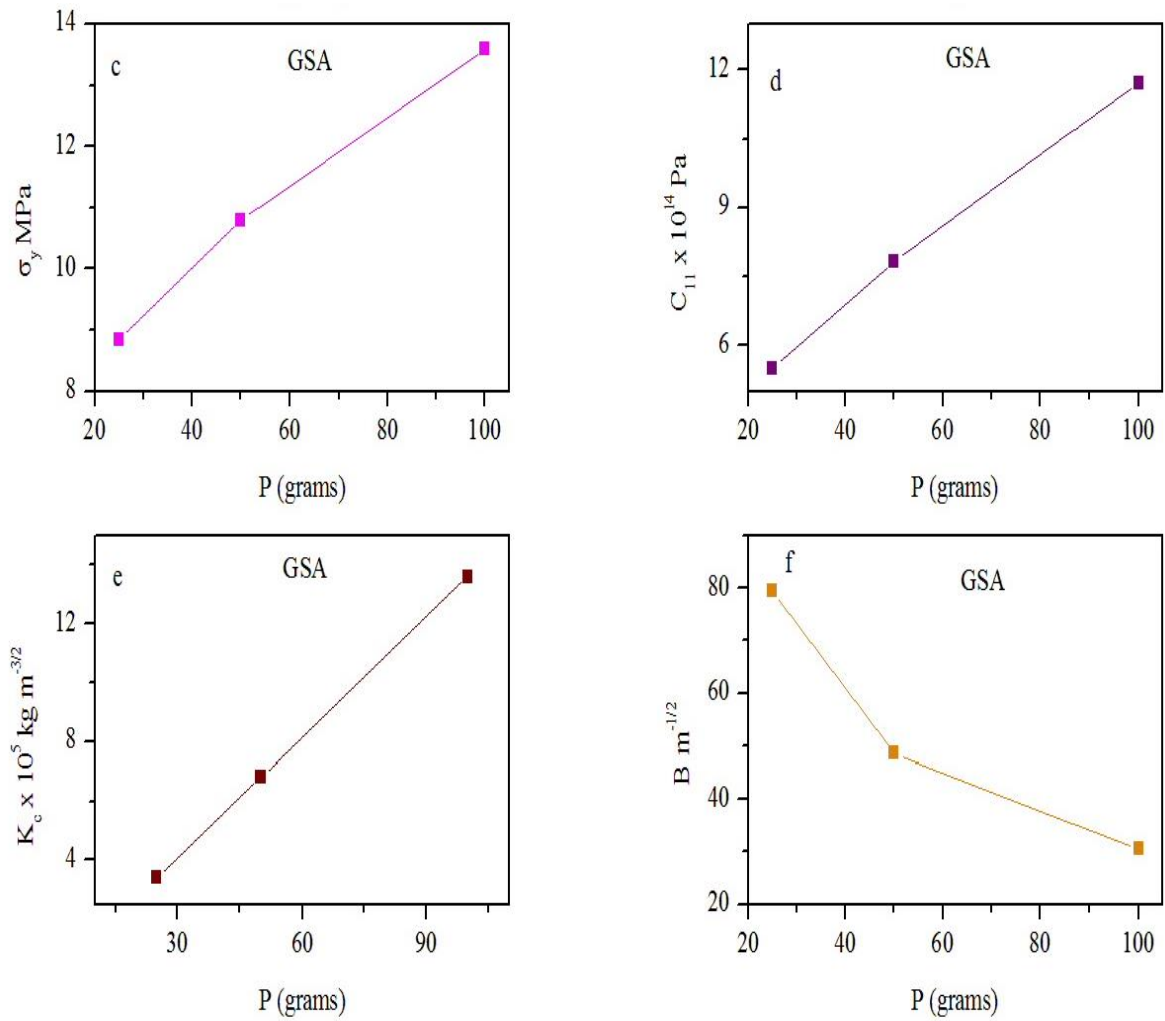


Fig.6 Plot of yield strength, elastic stiffness constant, fracture toughness coefficient and brittleness index as function of load

Table 3 Calculated mechanical parameters of GSA

Load (P) gm	Yield strength (σ_y) MPa	Elastic stiffness constant (C_{11}) x 10^{14} Pa	Fracture toughness (K_c) X $10^5 \text{ kgm}^{-3/2}$	Brittleness index (B) $\text{m}^{-1/2}$
25	8.836	5.51	3.401	79.53
50	10.796	7.82	6.803	48.58
100	13.589	11.7	13.606	30.58

Thermal studies

Thermo gravimetric analysis on the grown crystals GSA are performed with the help of Perkin Elmer Diamond instrument in nitrogen atmosphere with a rate of flow of 20

° C/min upto 800 °C. The corresponding curves are shown in fig.7.

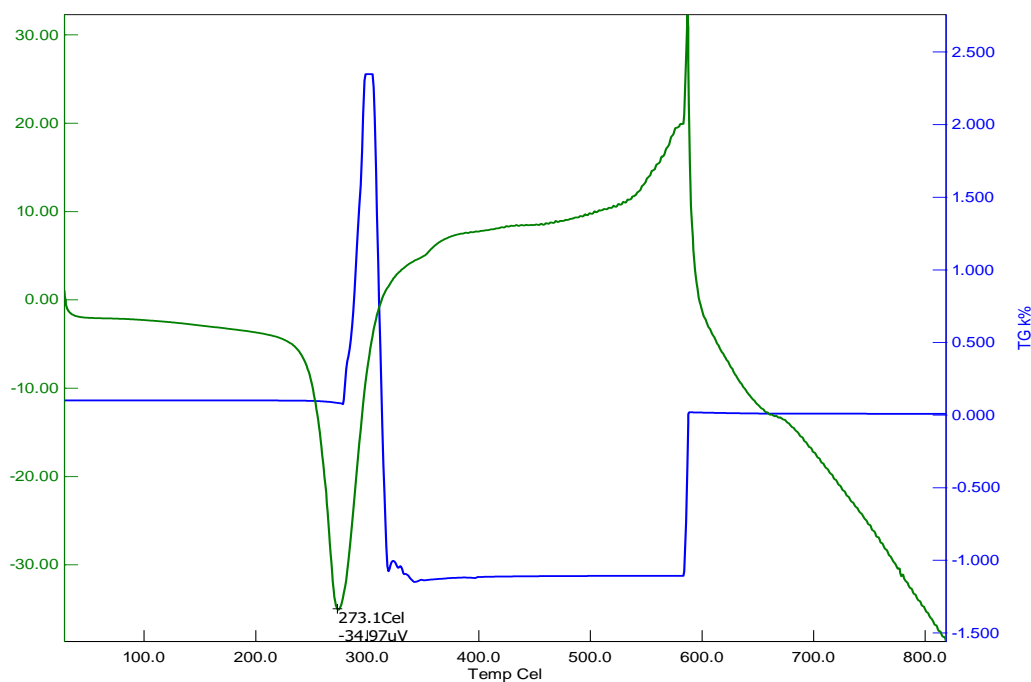


Fig.7 TG-DTA thermogram of GSA

GSA is thermally stable upto 273°C. This is proved both by TG and DTA. The occurrence of a sharp endothermic peak at 273.1°C represents the melting point of the component. A small sharp exothermic peak at 580°C may be due to volatilization of the compound. Melting point at 273 °C is also confirmed by the TG curve also.

Second order NLO studies

The Second Harmonic Generation (SHG) test for the grown sulphamic acid doped Glycine samples was performed using Nd: YAG laser with first harmonics output of 1064 nm, width 8 ns and repetition rate 10 Hz. The second harmonic signal generated in the samples was confirmed from the emission of green radiation. In this experiment, potassium dihydrogen phosphate (KDP) was used as the reference. Both the reference material and the samples are taken in powder form. The values of SHG relative efficiency of the grown crystals BASA and

GSA with reference to KDP are tabulated in the table 4. The powder SHG test confirms the NLO property of the samples. This shows that doped crystals will be better candidates for NLO applications. Due to the presence of dopant into the crystal lattice, there is an increase in polarizability of the molecules, which tends to increase the SHG efficiency.

Table 4 Value of relative SHG efficiency

Sample	Relative SHG Efficiency
GSA	0.613

Z-Scan analysis

Third order nonlinear optical property of the grown crystals GSA was studied by Z-scan technique. The magnitude and sign of the nonlinear refractive index (n_2) and nonlinear absorption coefficient (β) of the crystals were calculated from Z-scan data. The open aperture (OA) and closed aperture (CA) Z-scan methods are used for the simultaneous measurement of nonlinear absorption coefficient and nonlinear optical refraction for optical materials. In this experiment, Gaussian laser beam was used for molecular excitation and its propagation direction has been taken as Z –axis of the optically polished crystal. The beam was focused using a convex lens and the focal point was taken as $Z=0$. The monochromatic continuous wave (CW) laser light 632.8 nm with power 3.13 MW beam from He-Ne laser was used. The optically polished 1mm thick crystal was fixed in the travel range of 25 mm. The input energy and the energy transmitted by the sample were measured using a power meter. The normalized transmittance for the positioned crystal was measured at different positions and was used to calculate the third order nonlinear optical property of the crystal. The peak followed by a valley is the signature for nonlinearity of the material.

The Z-scan curves in closed and open aperture modes are illustrated in fig.8 and fig.9

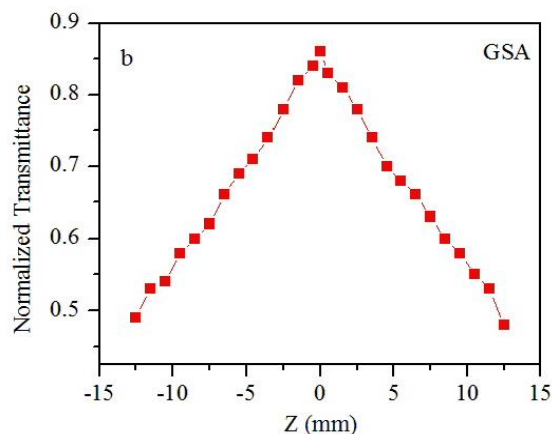


Fig.8 Open aperture Z-scan curve

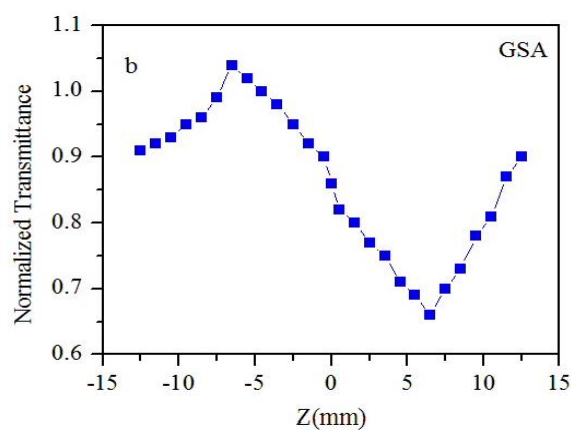


Fig.9 Closed aperture Z-scan curve

Table 5 Third harmonic nonlinear optical parameters of GSA

Sample	n_2 $10^{-12} \text{ cm}^2/\text{W}$	β 10^{-6} cm/W	R.P of $\chi^{(3)}$ 10^{-10}	LP of $\chi^{(3)}$ 10^{-10}	$\chi^{(3)}$ 10^{-9} e.s.u
GSA	4.546	1.081	7.904	9.465	1.233

The values of third order nonlinear refractive index, absorption coefficient and susceptibility for the crystals GSA are given in table 5. The negative value of nonlinear refractive index indicates the self defocusing nature of the crystals and nonlinear absorption value tells that the crystals have saturable absorption. Thus the materials which are opaque to a smaller number of photons have now become transparent when a large number of photons are incident on it.

Conclusion

Novel sulphamic acid doped NLO single crystals GSA were successfully grown by slow evaporation solution growth method at room temperature. The crystals are found to be colourless and transparent with well defined external appearance. Single crystal diffraction studies reveal that GSA belongs to monoclinic system. Powder XRD analysis elucidates the good crystalline nature of the samples and the planes responsible for the occurrence of reflecting peaks. FTIR studies are utilized to identify the modes of vibration and the possible functional groups present in the crystals. The crystals belong to the category of soft materials from Vickers's hardness analysis. GSA is stable upto 273 °C. Hence below these temperatures, these materials are ideal candidates for device fabrication. From SHG measurement, it is evident that GSA has 0.613 times SHG efficiency of KDP. The negative third order nonlinear refractive index of the doped crystals makes them prominent materials for protection optical night vision sensor devices. The open aperture transmittance data confirmed the saturable absorption by the candidates. The promising third order NLO properties of the crystals especially the self defocusing nature suggest their suitability for applications in optical limiting and photonic devices.

Reference

1. D.S. Chemla and J.Zyss, *Nonlinear Optical Properties of Organic Molecules and Crystals*, Vol 1,2, Academic press, Orlando (1987)
2. H.S. Nalwa, *Hand Book of Advanced Electronic and Photonic Materials and Devices*, Vol.9, Academic press, New York (2001). R. Valluvan, K. Selvaraju, S. Kumararaman, *Materials Chemistry and Physics*, **97** (2006) 81
3. Thaila T, Kumararaman S. *Spectrochimica Acta Part A: Molecular and Biomolecular Spectroscopy*, **82** (2011) 20



4. Samson Yesuvadian, Anbarasu Selvaraj, Martina Mejeba Xavier Methodius, Bhagavannarayana Godavarti, Vijayan Narayanasamy, Prem Anand Devarajan, *Optik – Int. J. for Light and Electron Optics*, **126** (2015) 95
5. Lipson H, Steeple H, *Interpretation of X-ray Powder Diffraction Pattern*, 5th edition, Macmillan, New York, (1970)
6. A.L. Smith, *Applied Infrared Spectroscopy* 2nd edition, Holden-Day (1977)
7. P.R. Griffiths, J.A. De Hoseth, *Fourier Transform Infrared Spectroscopy*, Wiley, Chichester (1986)
8. P.J. Haines, *Thermal Methods of Analysis*, Blackie, London (1995)
9. M.I. Pope, M.D. Judd, *Differential Thermal Analysis*, Heyden, Philadelphia (1997)
10. www.wordftest.com/ microhardness test
11. <http://www.gordonengland.co.uk/hardness/vickers.html>.
12. S. Ishwar Bhat, P. Mohan Rao, V. Upadyaya and H.S. Nagaraja, *Growth and Characterization of new nonlinear optical mixed borate crystals*, *Jour. of Crys. Growth*, **236** (2002) 318
13. C. Balarew, R. Dehlew, *Application of hard and soft acids and bases concept to explain ligand co-ordination in double salt structures*, *Jour. Solid State Chem.*, **55**,1(1984)1
14. Sahadevan Suresh, *Studies on growth, microhardness and dielectric characterization of Lithium Potassium Sulphate NLO single crystals*, *The African Review of Phy.*(2013)8,0006
15. S.K. Bachav, N.S. Patil, M.S. Kale, D.S. Bhavsar, *Crystal growth and characterization of Cobalt doped Barium Tartarate crystals by Silica Gel Method*, *Int. Jour. of Eng. Res. and App.*, **4**,8,(2014),108
16. D. Jaishree, G. Kanchana, R. Kesavasamy, *Investigations on growth, optical and thermal properties of Sulphamic acid single crystals*, *Advances in Condens. Matter Phy.*,(2014)
17. R. DeSalvo, N. Sheik-Bahae et al, *Z-scan measurements of the anisotropy of nonlinear refraction and absorption in crystals*, *Optics Letters*, Vol.**18**,no.3,194



Electrical conductivity measurements of pure and nickel sulphate doped KDP crystals grown by gel medium

M.P.Rameela¹, Vinu Bharathi² and T. Asaithambi^{2*}

¹Department of Physics, Sarah Thucker College For Women, Thirunelveli, India.

²P.G and Research Department of Physics, Alagappa Govt. Arts College, Karaikudi, India.

*Corresponding Author Email Id : tkthambi@gmail.com

Abstract

Crystals are the unacknowledged pillars of modern technology. Without crystals, there would be no electronic industry, no photonic industry, no fiber optic communications. Crystal growth is an interdisciplinary subject covering physics, chemistry, material science, chemical engineering, metallurgy, crystallography, mineralogy, etc. In past few decades, there has been a growing interest on crystal growth processes, particularly in view of the increasing demand of materials for technological applications. Optically good quality pure and metal doped KDP crystals have been grown by microbial free gel growth method at room temperature and their characterization have been studied. Gel method is a very simple method and can be utilized to synthesize crystals which are having low solubility. Potassium dihydrogen orthophosphate KH_2PO_4 (KDP) continues to be an interesting material both academically and industrially. KDP is a representative of hydrogen bonded materials which possess very good electro – optic and nonlinear optical properties in addition to interesting electrical properties. Due to this interesting properties, we made an attempt to grow pure and nickel sulphate doped kdp crystals in various concentrations (0.002, 0.004, 0.006, 0.008 and 0.010) using gel method. The grown crystals were collected after 15 days. We get crystals with good quality and shaped. The dc electrical conductivity(resistance, capacitance and dielectric constant) value were measured at different frequencies of pure and nickel sulphate added crystal with a temperature range of 40⁰C to 120⁰C using simple two probe setup with Q band digital LCR meter present in our lab. The electrical conductivity increases with increase of temperature. The dielectric constants of metal doped KDP crystals were slightly decreased compared to pure KDP crystals.

Keywords: KDP, NiSO_4



Introduction

Potassium dihydrogen orthophosphate (KDP) KH_2PO_4 continues to be an interesting material both academically and industrially. KDP is a representative of hydrogen bonded materials which possess very good electro-optic and nonlinear optical properties in addition to interesting electrical properties. The demand for high quality large single crystals of KDP increase due to the application as frequency conversion crystal in inertial confinement fusion [1-2]. The piezo electric property of KDP crystal makes it useful for the construction of crystal filters and frequency stabilizers in electronic circuit's .

The excellent properties of KDP include transparency in a wide region of optical spectrum, resistance to damage by laser radiation and relatively high non- linear efficiency, in combination with reproducible growth to large size. Therefore, it is commonly used in several applications such as laser fusion, electro-optical modulation and frequency conversion. Many studies on the growth and properties of KDP crystals in the presence of impurities have been reported [3 - 4]. Potassium dihydrogen phosphate (KDP) crystal draws persistent attention of scientists due to its excellent quality and possibility of growing large- size crystals [5 - 6]. Microscopically, crystal growth includes crystal morphology, crystal defects, and growth rate, which are all related to the constituent growth units and their chemical bonding process [7 - 8]. KDP, ADP and DKDP are the only nonlinear crystal currently used for these applications due to their exclusive properties. The grown crystals were characterized using dielectric constant, electrical properties, optical transmittance, for pure and NiSO_4 doped KDP crystals.

Materials and Methods

Pure and NiSO_4 doped KDP single crystals are grown in sodium meta silicate gel medium using analar grade KDP and NiSO_4 with in concentrations of 0.002, 0.004, 0.006, 0.008 and 0.010 of dopant and sodium meta silicate ($1.08\text{g}/\text{cm}^3$). During the process p^{H} was maintained at 5-6 at room temperature figure (1). Ethyl alcohol of equal volume is added over the set gel without damaging the cell surface .When the alcohol diffuses into the set gel, it reduces the solubility. This induces nucleation and the nuclei are grown into the single crystals. The crystal growth was carried out at room temperature. The growth period was about 20 days for pure and NiSO_4 doped KDP crystals. Pure and KDP doped crystals are shown in the fig (2).



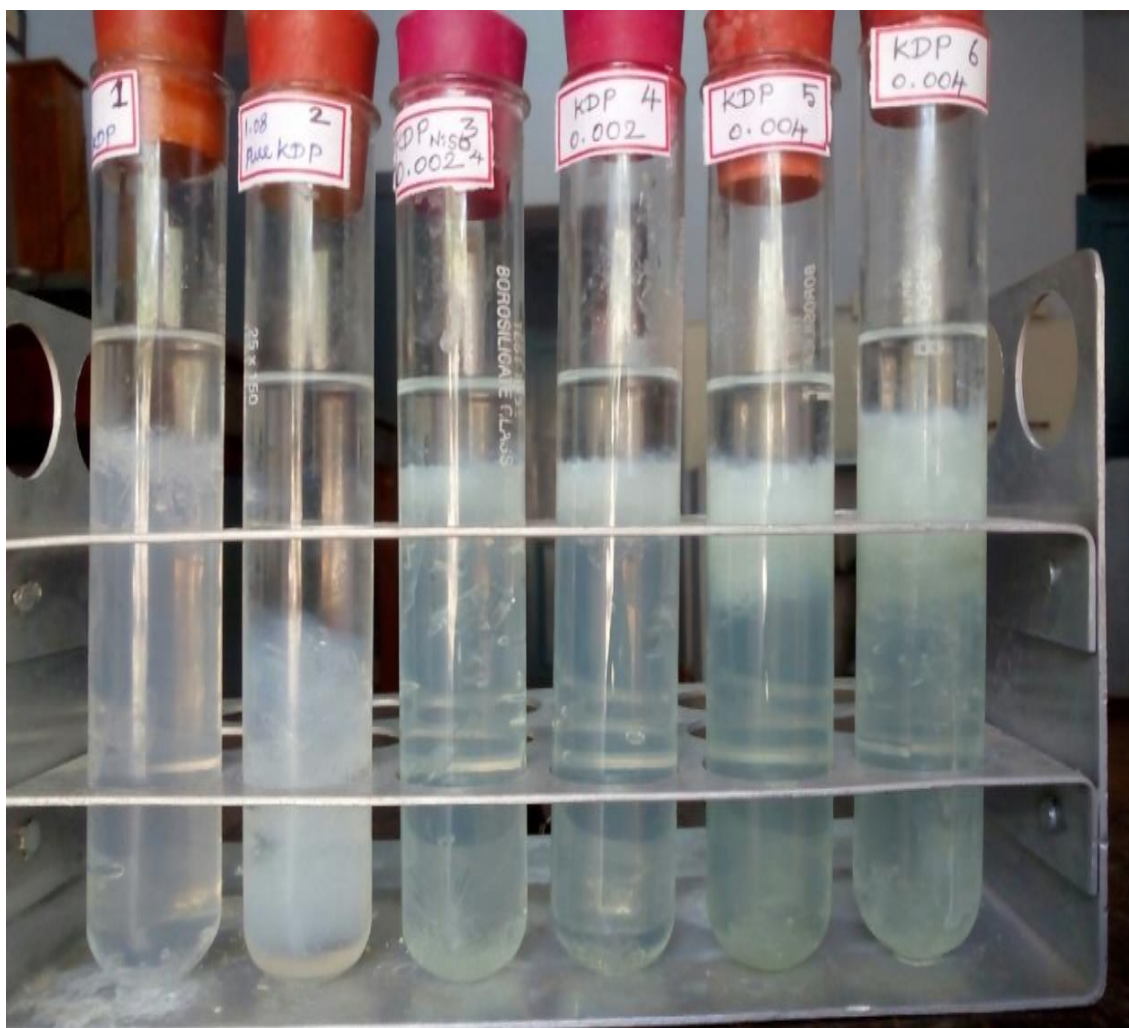
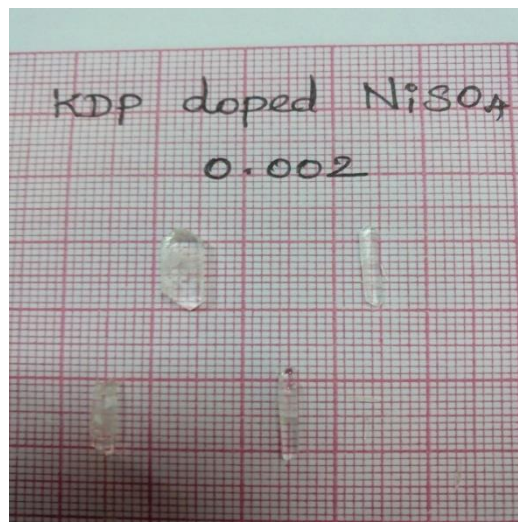
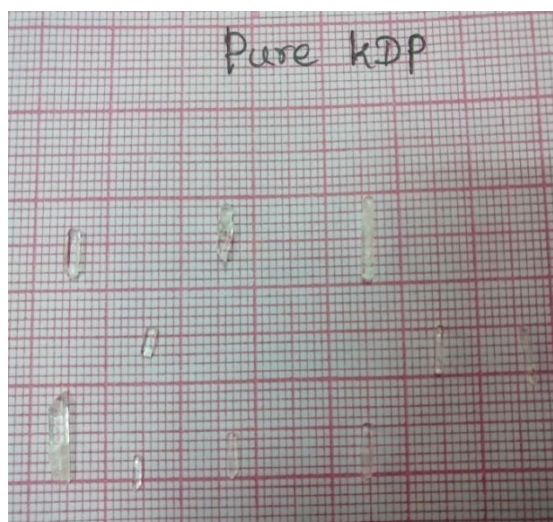


Figure.1 Growth of pure KDP doped with NiSO₄ with various concentrations



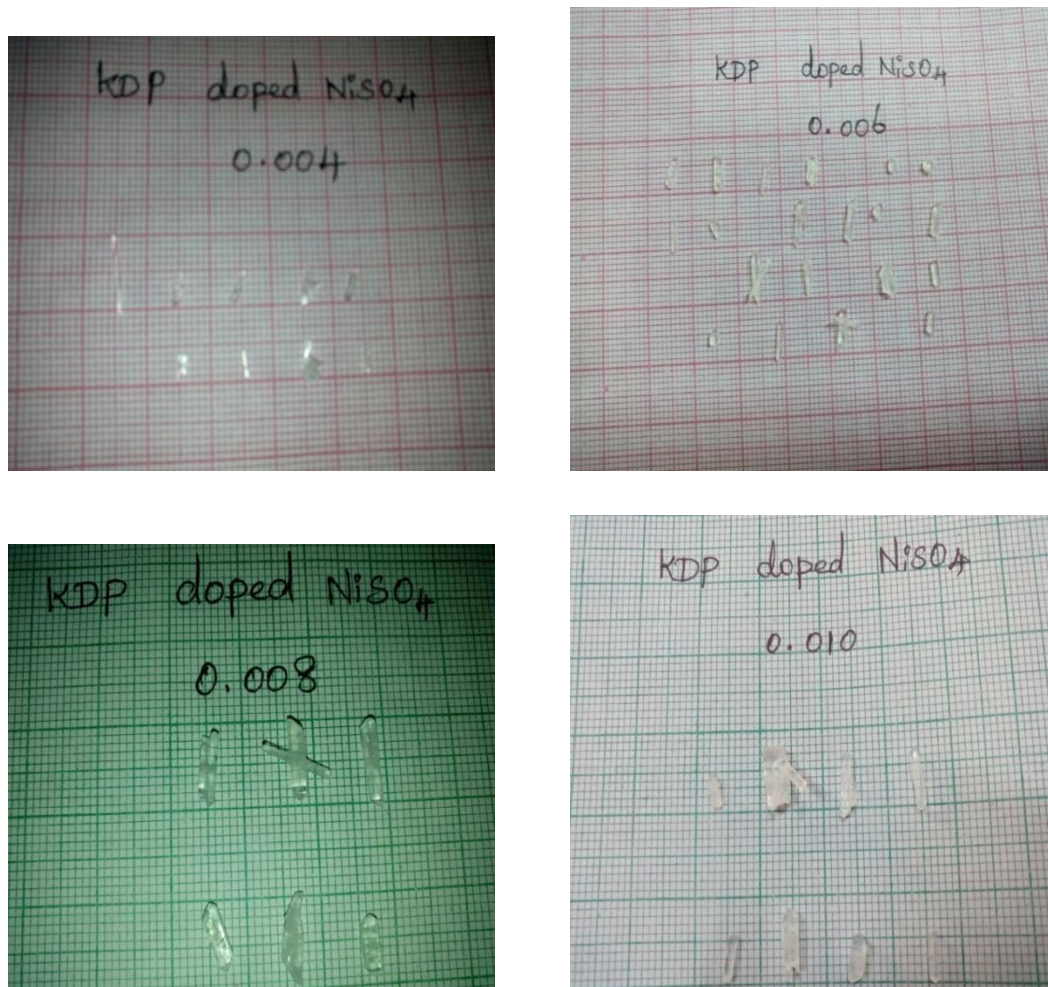


Fig. 2. Gel grown Pure KDP and NiSO₄ added KDP crystals

Doping

Doping means adding impurity to the known pure crystal. To prepare a doped crystal a required amount of dopant solute is also mixed along with the pure solute.

Table 1: Doping concentrations of impurities

Doping ratio	Mass of NiSO ₄ Added in gm
1 : 0.002	0.06571
1 : 0.004	0.13143
1 : 0.006	0.19714
1 : 0.008	0.26286
1 : 0.010	0.32857

An impurity can suppress, enhance or stop the growth of crystal completely. It usually acts on certain crystallographic faces. The effects depend on the impurity concentration, super saturation, temperature and pH of the solution.

Results and Discussions

Dielectric constant and electrical conductivity studies

Dielectric properties are correlated with electro- optic properties of the crystals particularly when they are non- conducting materials. Due to the incorporation of metal ions polarization increases and the electrical conductivity increases. (fig.5,6) The magnitude of dielectric constant depends on the degree of polarization, charge displacement in the crystal. The dielectric constant of materials is due to the contribution of electronic, ionic, dipolar and space charge polarizations which depends on the frequencies [5]. At low frequencies, all these, polarization are active lower frequencies and high temperatures [6], in KDP crystals, many reports are available about its dielectric behavior and in our present work the measured dielectric constant values are in good agreement with the reported results [7-8]. The temperature dependence of dielectric constant at frequency 100Hz to 1KHz is shown in fig. 4,5. Even though KDP has many reports on dielectric loss, the study clearly ensures the crystalline perfection of crystals in our present case; it is observed that the dielectric loss decreases with increasing frequency and low dielectric losses were observed for the gel method crystal compared to the solution growth. The lower value of dielectric constant is a suitable parameter for the enhancement of SHG signals. The measurement of dielectric constant and loss as a function of frequency at different temperatures give an idea about the electrical processes that are taking place in materials and these parameters were measured on the polished (010) face of the pure and metal doped KDP crystals. Frequency dependences of dielectric constant of these crystals at room temperature are observed from the figures and it is observed that dielectric constant of KDP and NiSO₄ doped KDP crystals are high at low frequencies and they decrease with increase in frequency. The very high value of ϵ_r at low frequencies may be due to the presence of all four polarizations namely space charge, orientation, electronic and ionic and its low values at higher frequencies may be due to the loss of significance of these polarizations gradually. The nature of decrease of ϵ_r frequency suggests that pure and NiSO₄ doped KDP crystals contain dipoles of continuously varying relaxation times.



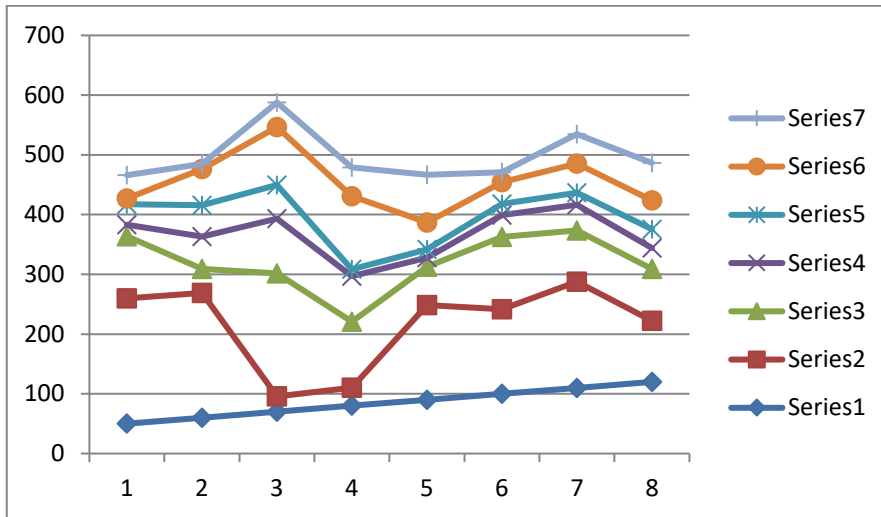


Fig.3. Variation of dielectric constant (ϵ_r) with temperature at frequency of 100Hz for pure and NiSO₄ doped KDP crystals

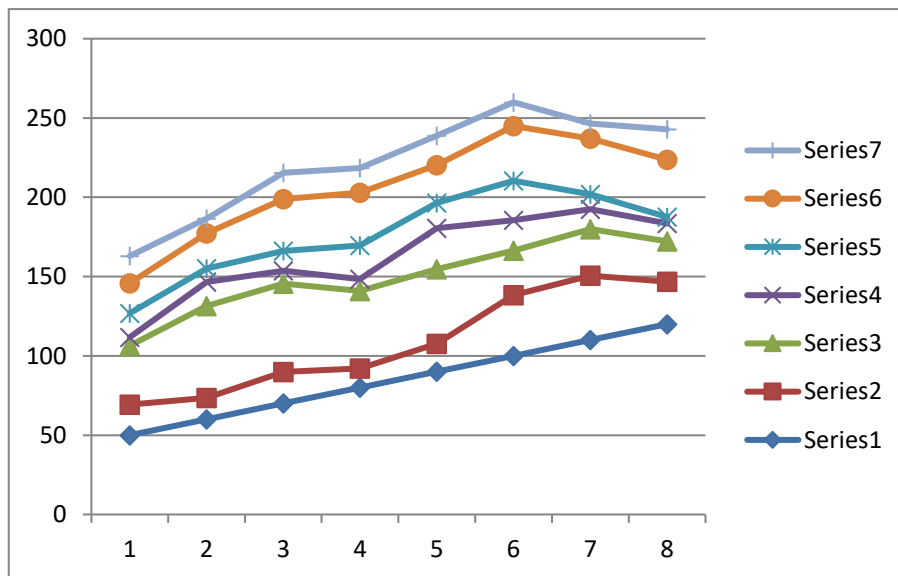


Fig.4. Variation of dielectric constant (ϵ_r) with temperature at frequency of 1KHz for pure and NiSO₄ doped KDP crystals

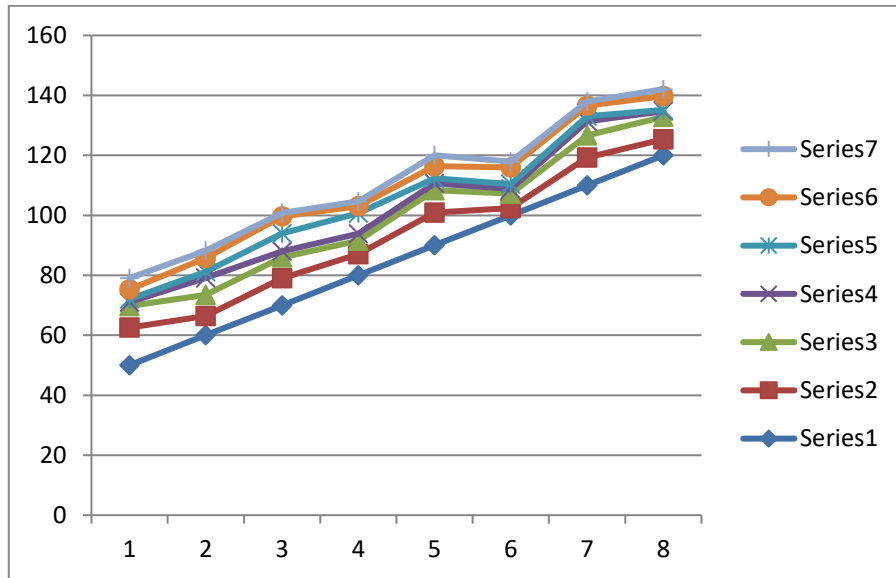


Fig.5. Variation of electrical conductivity (σ) with temperature at frequency of 100Hz for pure and NiSO₄ doped KDP crystals

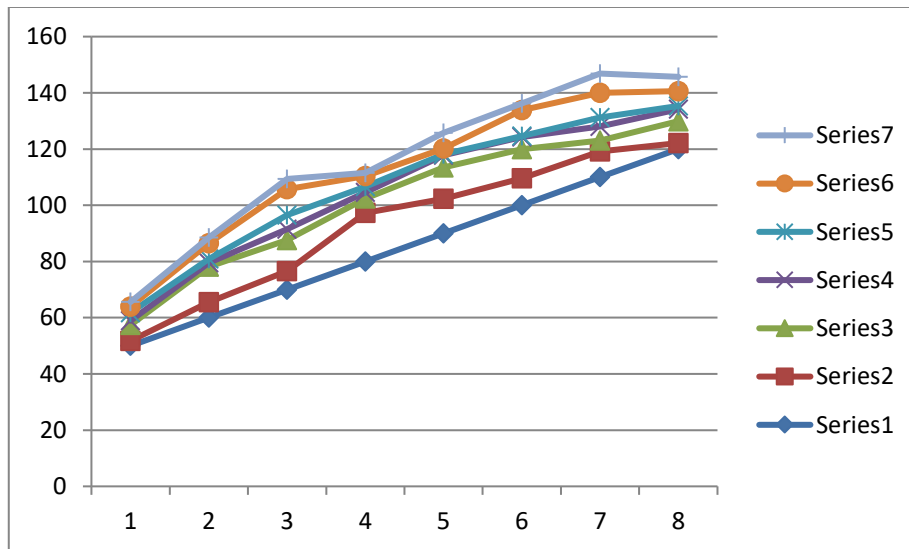


Fig.6. Variation of electrical conductivity (σ) with temperature at frequency of 1KHz for pure and NiSO₄ doped KDP crystals

Conclusion

Pure KDP crystals and metal doped KDP crystals are grown by gel method. In gel growth, due to the three dimensional structures, the crystals are free from microbes. The capacitance and dielectric constant and electrical conductivity were measured at different frequencies of pure and NiSO₄doped KDP crystals. The capacitance and dielectric constants of metal doped KDP crystals were slightly decreased compared to pure KDP crystals. The lower the value of dielectric constant more is the enhancement of SHG signals. The electrical conductivity (σ) of the pure KDP and NiSO₄ doped KDP crystals were found to be increase with increase of temperature and frequencies.

References

1. X.Sun, X. Xu, Z.Gao, Y.Fu, S.Wahg, H.Zong, Y.Li, *J.Cryst.Growth.*, **217**(2000) 404
2. N.Zaitseva, L.Carman, I.Smolsky, *J.Cryst.Growth.*, **241** (2002) 363.
3. Bo Wang. Chang –shuiFang.Sheng –lai Wang, Xun Sun, Quing-tianGu, Yi-ping Li, XinguangXu, JianqinZhang, BingLiu, with potassium carbonate as additives .*J.Cryst.Growth.*, **310**, (2008) 5341-5346.
4. N.Pattanaboonmee, P.Ramasamy, P.Manyumprocedia Engineering., **32** (2012) 1019-1025.
5. Dongli Xu, Dongfeng Xue. *J.Cryst. Growth.*, **310** (2008) 1385
6. Dogli Xu, Dongfeng Xue, *J.Alloys Compd.*, **449** (2008) 353
7. Dongli Xu, Dongfeng Xue. *J.Cryst. Growth.*, **310** (2008) 1385
8. S.Balamurugan, P.Ramasamy, *Spectrochimica Acta.*, Part A **71** (2009) 1979-1983



Systematical calculation of Alpha decay half-lives of heavy nuclei from ground state to ground and excited states of daughter

G. M. Carmel Vigila Bai¹ and R. Nithya Agnes^{2*}

¹Rani Anna Government College for women, Tirunelveli, India.

²St. John's College, Palayamkottai, India.

*Corresponding Author Email Id: rcalvinsamuel@gmail.com

Abstract

The alpha decay is one of the most important decay processes of the heavy and super heavy nuclei. Using Cubic Plus Yukawa Plus Exponential model, the alpha decay of even-even isotopes of Cm nuclei in the range $238 \leq A \leq 250$, Cf nuclei in the range $240 \leq A \leq 256$ and Fm nuclei in the range $246 \leq A \leq 256$ from ground state to ground state and ground state to excited states of daughter nuclei have been studied by including both quadrupole (β_2) and hexadecapole (β_4) deformations of parent and daughter nuclei as well as the spin-parity effects. The computed half-lives are compared with available data and are found in good agreement with each other. Hindrance factor and branching ratio have been calculated. The centrifugal barrier effect on decay rate is also investigated.

Keywords: Alpha decay, Q - value and fine structure

Introduction

Alpha decay can provide some reliable information on nuclear structure and nuclear reaction. The alpha decay theory was formulated by Gamow[1] and independently by Gurney and Condon on the basis of quantum tunnelling. The fine structure of alpha decay was formulated by Salomon Rosenblum [2] in 1929. In this paper we have studied the alpha decay of even-even nuclei from ground to ground and excited states of daughter nuclei using (CYEM) Cubic Plus Yukawa Plus Exponential model [3] by incorporating the ground state deformation β_2 and β_4 of the parent and daughter but treating the emitted cluster as a sphere. The details of our model are described in section 2. The results and discussion are given in section 3. Finally the conclusions are given in section 4.



Cubic plus Yukawa plus Exponential Model

In this work, the spins and the parities of parent and daughter nuclei are included; the daughter nucleus has a quadrupole deformation only and the emitted cluster is considered to be spherical. If the parent nuclei have deformations say quadrupole and hexadecapole and if the Q-value of the reaction is taken as the origin, the potential for the post - scission region as the function of the centre of mass distance 'r' of the fragment is given by

$$V(r) = V_c(r) + V_n(r) + \ell(\ell+1)\hbar^2/2\mu r^2 - V_{df}(r) - Q \quad (1)$$

Here V_c is the coulomb potential between a spheroid daughter and spherical emitted cluster. V_n is the nuclear interaction energy due to finite range effects of Krappe et al[4]; and V_{df} is the change in nuclear interaction energy due to quadrupole and hexadecapole deformations in the daughter nuclei, 'r' is the distance between fragment centers, 'ℓ' is the angular momentum, and 'μ' is the reduced mass. The angular momentum carried by the alpha particle in a ground state to ground state transition of even-even nucleus is zero. In odd-even or odd-odd nuclei, it could not be equal to zero. In this case, the centrifugal barrier term must be added with the Coulomb barrier. The values of natural angular momentum have been obtained from the usual nuclear spin and parity conservation law,

$$|J_i - J_j| \leq \ell \leq |J_i + J_j| \quad \text{and} \quad \pi_i \pi_j = (-1)^\ell \quad (2)$$

Where J_i, π_i and J_j, π_j are the spin and parity of parent and daughter nuclei respectively.

The effect of atomic electrons on the energy of alpha particle should also be taken into account.

The energy of alpha particle emitted from nucleus in alpha decay is

$$Q_i = Q_{g.s \rightarrow g.s} - E_i^* \quad (3)$$

Where $Q_{g.s \rightarrow g.s}$ is the Q- value for ground state to ground state transition and E_i^* is the excitation energy of daughter nucleus to the i th state. The ground state to ground state Q-value is given by

$$Q_{g.s \rightarrow g.s} = \Delta M_p - (\Delta M_d + \Delta M_\alpha) + [k_1(Z_p^{\beta_1} - Z_d^{\beta_1}) - k_2 Z_c^{\beta_2}] \quad (4)$$

Where M_p, M_d, M_α are the mass excess of parent, daughter and alpha nuclei as tabulated by Audi et al [5]. Where the terms in the brackets represent the effect of the screening to the nucleus caused by the surrounding electrons. The quantity kZ^β represents the total binding energy of the Z-electrons in the atom, where the values $k_1 = 8.7 \times 10^{-6}$ MeV and $\beta_1 = 2.517$ for nuclei of $Z \geq 60$ and $k_2 = 13.6 \times 10^{-6}$ MeV and $\beta_2 = 2.408$ for $Z < 60$ have been found from reported by Huang et al [6].



For a prolate spheroid daughter nucleus with longer axis along the fission direction, Pik - Pichak [7] obtained

$$V_c(r) = \frac{3}{2} \frac{Z_d Z_e e^2 \gamma}{r} \left[\frac{1-\gamma^2}{2} \ln \frac{\gamma+1}{\gamma-1} + \gamma \right] \quad (5)$$

and for an oblate spheroid daughter nucleus with shorter axis along the fission direction

$$V_c(r) = \frac{3}{2} \frac{Z_d Z_e e^2}{r} [\gamma (1 + \gamma^2) \arctan \gamma^{-1} - \gamma^2] \quad (6)$$

For the overlapping region, we approximate the potential barrier by a third order polynomial in (r) as suggested by Nix[8] having the form

$$V_c(r) = -E_v [V(r)_t + E_v] \left\{ S_d \left(\frac{r-r_i}{r_t-r_i} \right)^2 - S_e \left(\frac{r-r_i}{r_t-r_i} \right)^3 \right\} \quad (7)$$

$$r_i \leq r \leq r_t$$

Where $r_t = a_e + R_d$

Here a_e is the semi-major (or) minor axis of the spheroid cluster depending on the prolate (or) oblate shape of the emitted cluster; and r_i is the distance between the centers of mass of the daughters and the emitted particle portions in the spheroid parent nucleus.

If the nuclei have spheroid shape, the radius vector $R(\theta)$ making an angle θ with the axis of symmetry locating sharp surface of a deformed nuclei is given by ref [3]

$$R(\theta) = R_o \left[1 + \sum_{n=0}^{\infty} \sum_{m=-n}^{\infty} \beta_{nm} \gamma_{nm}(\theta) \right] \quad (8)$$

Here R_o is the radius of equivalent spherical nucleus.

If we consider spheroid deformation β_2 then

$$R(\theta) = R_o \left[1 + \beta_2 \left(\frac{5}{4\pi} \right)^{1/2} \left(\frac{3}{2} \cos^2 \theta - 1/2 \right) \right] \quad (9)$$

and if Nilsson hexadecapole deformation β_4 is also included in the deformation then eqn (6) becomes

$$R(\theta) = R_o \left[1 + \beta_2 \left(\frac{5}{4\pi} \right)^{1/2} \left(\frac{3}{2} \cos^2 \theta - 1/2 \right) + \beta_4 \left(\frac{9}{4\pi} \right)^{1/2} \frac{1}{8} (35 \cos^4 \theta - 30 \cos^2 \theta + 3) \right] \quad (10)$$

Expressing the energies in MeV, lengths in fm and time in seconds for calculating the life time of the decay system we use the formula,

$$T = \frac{1.433 \times 10^{-21}}{E_\nu} (1 + \exp(k)) \quad (11)$$

The action integral K is given by $K = K_L + K_R$

$$\text{Where } K_L = \frac{2}{h} \int_{r_a}^{r_t} [2B_r V(r)]^{1/2} dr \quad (12)$$

$$K_R = \frac{2}{h} \int_{r_t}^{r_b} [2B_r (r)V(r)]^{1/2} dr \quad (13)$$

The limits of integration r_a and r_b are the two appropriate zeros of the integrand which are found numerically.

Results and Discussion

We have made our calculations by including quadrupole and hexadecapole deformations of parent and daughter nuclei which are taken from the tables of Moller et al[9] and spin-parity effects. We have calculated alpha decay half lives for experimentally known even-even nuclei of Cm, Cf and Fm isotopes. The computed half-lives of alpha decay are compared with the available data. The calculated half-lives are in good agreement with the available data. Table.1 gives the Logarithmic half-lives for alpha decay of even-even isotopes of some actinide nuclei from ground state to ground state transition. Figure 1 gives the plot of logarithmic half lives vs. Q values. Some of the nuclei are found to have long half-lives which indicate the stability and magicity of corresponding parent nuclei and lower half –lives value indicates the same corresponding to daughter nuclei. Table.2 gives the Logarithmic half-lives for alpha decay of even-even isotopes of ^{244}Cm , ^{252}Cf and ^{254}Fm nuclei from ground state to excited state transition. All these transitions are taken from Ref[11]. The angular momentum carried by the even-even nuclei from ground state to excited state is not zero and hence the centrifugal potential is added to the potential energy $V(r)$. From table 2, it is found that, with the inclusion of centrifugal term the half life value gets increased. Because it increases height of the potential barrier. Figure2 gives alpha decay scheme for ^{254}Fm Parent nucleus to various levels of ^{250}Cf daughter nucleus. Fig.3 showing the Histogram for Branching ratio of ^{244}Cm , ^{252}Cf and ^{254}Fm nuclei.

The standard deviation is estimated using the following expression.

$$\sigma = \sqrt{\frac{1}{(n-1)} \sum_{i=1}^n [\log T_i^{\text{theor.}} - \log T_i^{\text{exp.}}]^2}$$



The estimated standard deviation for the half lives by our model is 0.2395 while the same calculated by Ref [10] is 0.21008. The hindrance Factor (HF) is calculated by the formula,

$$HF = \frac{T_{1/2}^{exp.}}{T_{1/2}^{thero.}}$$

The calculated HF is close to unity which shows better result. The branching ratios

of alpha decay to each state of the daughter nucleus have been evaluated with the help of the alpha decay width,

$$B = \Gamma(Q_i, \ell_i) \times 100\% / \sum(Q_n, \ell_n)$$

Where the sum n is going over all states, which can be populated during the alpha transition from the ground state of the parent nucleus. The Branching ratio value is found to be greater for all ground to ground transitions and is going on decreased for all other transitions.

Table1. Comparison of calculated values of logarithm of half life time for oven-even isotopes of some actinide nuclei from ground state to ground state transition.

Decay mode	Q(MeV)	LogT(s)			HF (cal.)
		Expt	Ref[10]	CYEM	
${}_{96}\text{Cm}^{238} \rightarrow {}_{94}\text{Pu}^{234} + {}_2\text{He}^4$	6.668	5.51	5.26	5.46	1.1220
${}_{96}\text{Cm}^{240} \rightarrow {}_{94}\text{Pu}^{236} + {}_2\text{He}^4$	6.440	6.52	6.29	6.48	1.0965
${}_{96}\text{Cm}^{242} \rightarrow {}_{94}\text{Pu}^{238} + {}_2\text{He}^4$	6.258	7.28	6.86	7.38	0.7943
${}_{96}\text{Cm}^{244} \rightarrow {}_{94}\text{Pu}^{240} + {}_2\text{He}^4$	5.945	8.87	8.57	8.97	0.7943
${}_{96}\text{Cm}^{246} \rightarrow {}_{94}\text{Pu}^{242} + {}_2\text{He}^4$	5.518	11.26	11.10	11.47	0.6166
${}_{96}\text{Cm}^{248} \rightarrow {}_{94}\text{Pu}^{244} + {}_2\text{He}^4$	5.204	13.16	13.14	13.51	0.6166
${}_{98}\text{Cf}^{240} \rightarrow {}_{96}\text{Cm}^{236} + {}_2\text{He}^4$	7.760	2.03	1.75	1.90	1.3489
${}_{98}\text{Cf}^{242} \rightarrow {}_{96}\text{Cm}^{238} + {}_2\text{He}^4$	7.560	2.41	2.52	2.61	0.6310
${}_{98}\text{Cf}^{244} \rightarrow {}_{96}\text{Cm}^{240} + {}_2\text{He}^4$	7.374	3.18	2.88	3.30	0.7586
${}_{98}\text{Cf}^{246} \rightarrow {}_{96}\text{Cm}^{242} + {}_2\text{He}^4$	6.907	5.21	5.19	5.29	0.8318
${}_{98}\text{Cf}^{248} \rightarrow {}_{96}\text{Cm}^{244} + {}_2\text{He}^4$	6.406	7.56	7.19	7.68	0.7586
${}_{98}\text{Cf}^{250} \rightarrow {}_{96}\text{Cm}^{246} + {}_2\text{He}^4$	6.174	8.69	8.45	8.86	0.6761
${}_{98}\text{Cf}^{252} \rightarrow {}_{96}\text{Cm}^{248} + {}_2\text{He}^4$	6.262	8.01	8.08	8.46	0.3548
${}_{98}\text{Cf}^{254} \rightarrow {}_{96}\text{Cm}^{250} + {}_2\text{He}^4$	5.972	9.31	9.99	10.05	0.1820
${}_{98}\text{Cf}^{256} \rightarrow {}_{96}\text{Cm}^{252} + {}_2\text{He}^4$	5.600	10.87	12.22	12.25	0.0417
${}_{100}\text{Fm}^{246} \rightarrow {}_{98}\text{Cf}^{242} + {}_2\text{He}^4$	8.421	0.17	0.31	0.39	0.6025
${}_{100}\text{Fm}^{248} \rightarrow {}_{98}\text{Cf}^{244} + {}_2\text{He}^4$	8.048	1.66	1.55	1.68	0.9549
${}_{100}\text{Fm}^{250} \rightarrow {}_{98}\text{Cf}^{246} + {}_2\text{He}^4$	7.604	3.38	3.26	3.36	1.0471
${}_{100}\text{Fm}^{252} \rightarrow {}_{98}\text{Cf}^{248} + {}_2\text{He}^4$	7.198	5.04	4.97	5.01	1.0715
${}_{100}\text{Fm}^{254} \rightarrow {}_{98}\text{Cf}^{250} + {}_2\text{He}^4$	7.354	4.14	4.08	4.42	0.5248
${}_{100}\text{Fm}^{256} \rightarrow {}_{98}\text{Cf}^{252} + {}_2\text{He}^4$	7.073	5.14	5.27	5.65	0.3090



Table2. Comparison of calculated values of logarithm of half life time for oven-even isotopes of some actinide nuclei from ground state to excited states of daughter nuclei

Transition	Q(MeV)	LogT(s) (Calculated)	B _{cal.}
²⁴⁴Cm→²⁴⁰Pu			
0 ⁺ →0 ⁺	5.945	8.97	83.88
0 ⁺ →2 ⁺	5.902	9.70	15.62
0 ⁺ →4 ⁺	5.803	11.20	0.494
0 ⁺ →6 ⁺	5.651	13.23	4.61e-3
0 ⁺ →8 ⁺	5.448	15.71	1.53e-5
²⁵²Cf→²⁴⁸Cm			
0 ⁺ →0 ⁺	6.262	8.46	86.04
0 ⁺ →2 ⁺	6.219	9.26	13.64
0 ⁺ →4 ⁺	6.118	10.89	0.320
0 ⁺ →6 ⁺	5.964	13.10	1.97e-3
0 ⁺ →8 ⁺	5.757	15.70	4.95e-6
²⁵⁴Fm→²⁵⁰Cf			
0 ⁺ →0 ⁺	7.354	4.43	85.12
0 ⁺ →2 ⁺	7.311	5.20	14.46
0 ⁺ →4 ⁺	7.212	6.76	0.398
0 ⁺ →6 ⁺	7.057	8.80	3.63e-3

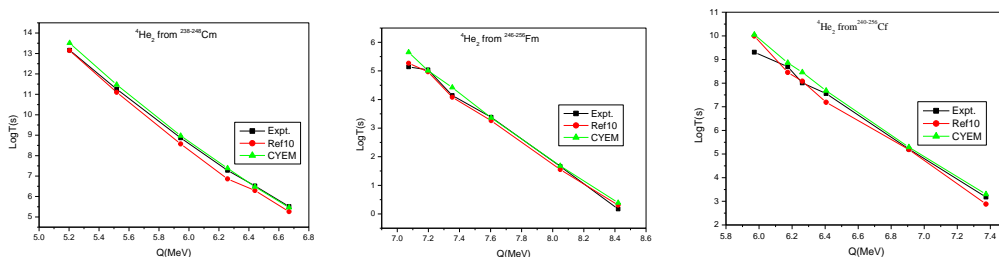


Fig.1. Logarithmic half lives of alpha decay Vs Q values including deformation effects.

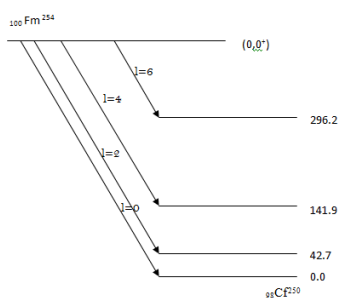


Fig.2.Schematic representation of alpha decay of ^{254}Fm parent nucleus to various levels of ^{250}Cf daughter nucleus.

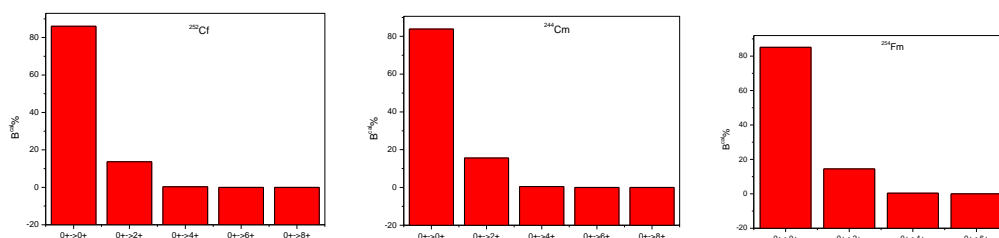


Fig.3. Histogram for Branching ratio of ^{244}Cm , ^{252}Cf and ^{254}Fm nuclei.

Conclusions

We have calculated alpha decay half –lives of even-even nuclei using CYEM model. The computed half-lives are compared with available data and are found in good agreement with each other. The calculated HF is found to be unity which shows better result. If the Hindrance Factor is between 1 and 4, the transition is called a ‘favoured transition’. Due to this effect, height of the potential barrier gets increased and it increases the half life value also. The Branching ratio value is found to be greater for all $0^+ \rightarrow 0^+$ transitions followed by $0^+ \rightarrow 2^+$ transitions while the same decreases as we move from ground to other excited state transitions. That means the alpha transmissions to the remaining excited states are strongly hindered.

References

- [1] G.Gamow, Z.Phys. 51,204 (1928)
- [2] Salomon Rosenblum, C.R.Acad. Sci.Paris 188 (1929) 1401

- [3] G.Shanmugam, G.M.CarmelVigilaBai and B.Kamalaharan, Phys. RevC51, 2616 (1995)
- [4] H.J.Krappe, J.R.Nix,andA.J.Sierk,Phys.Rev.C20, 992 (1979)
- [5] G. Audi, O.Bersillon, J.Blachot and A.H. Wapstra 2003 The NUBASE evaluation of nuclear and decay properties Nucl. Phys. A7293.
- [6] K.N.Huang, M.Aoyagi, M.H.Chen, B.Crasemaon and H.Mark 1976 Neutral-atom electron binding energies from relaxed-Orbital relativistic Hartree-Fock-Slater calculations $2 \leq Z \leq 106$ At.Data Nucl. Data Tables 18 243.
- [7] G.A. Pik – Pichak, Yad.Fiz.44,1421(1986) Sovt. J. Nucl. Phys. 44,923 (1986).
- [8]J.R.Nix,Ann.Phys.(N.Y.)41,52(1962)
- [9] P.Moller, J.R.Nix, W.D.Myers and W.J.Swiatecki Nuclear ground-state masses and deformations At. Data Nucl. Data Tables 59 185 – 381 (1995)..
- [10] V Yu Denisov and A A Khudenko, Phys. Rev.C80(2009)034603.
- [11]<http://www-nds.iaea.org/RIPL-2/>.



Synthesized and Characterization of cerium dioxide (ceria) nanoparticles by using a microwave oven

R.Anitha^{1a}, E.Kumar^{1*} and D. Muthuraj²

¹Department of Physics, Sri.S.Ramasamy Naidu Memorial College, Sattur, India.

Research Scholar, Bharathiyar University, Coimbatore, India.

^{1*}Department of Physics, School of Science, Tamil Nadu Open University, Chennai, India.

²Department of Physics, The MDT Hindu College, Tirunelveli, India.

Abstract

In this work, nanoparticles of cerium oxide (CeO₂) were synthesized by solution method using a microwave oven. The precursor used to prepare the nanoparticles of CeO₂ was ammonium ceric nitrate. The precursor was dissolved in de-ionized water and pH value of the solution was adjusted to be at 12 using sodium hydroxide. The prepared solution was kept in the microwave oven at a temperature of 70 °C for about 30 minutes. Then, the light yellow precipitates were thoroughly washed with de-ionized water, and dried at 95 °C for 8 h to form as prepared powder. Conventional thermal treatment of the as prepared powder at 200 °C for about 2 hours. The synthesized CeO₂ nanoparticles were subjected to various techniques like XRD, SEM, and FT-IR studies.

Keywords: CeO₂, nanoparticles,

Introduction

Conventional materials like metals, semiconductors, glass, ceramics, polymers, oxides etc can be converted into smart materials in nano-scale dimensions. Nanomaterials range from inorganic to organic, crystalline to amorphous, which can be found as single particles, aggregates, powders, nanowires, quantum dots, nanofilms, nanofibres, nanotubes. Nanomaterials have unique and interesting properties when compared to conventional materials [1]. Cerium oxide(CeO₂), Ceria, is one of the most important rare- earth oxides, finds wide applications in electrolyte materials of solid oxide fuel cells, ultraviolet blocking materials, in the field of catalysts, Chemical Mechanical Polishing (CMP) and oxygen gas sensors and so on [2-6]. It has a fluorite – like cubic structure in which each cerium site is



surrounded by eight oxygen sites in fcc arrangement and each oxygen site has a tetrahedron cerium site. Methods based on wet chemical routes like co-precipitation, hydrothermal, sol-gel method, microemulsion method etc have been employed to synthesize of CeO₂ nanoparticles by many researchers [7-14]. But the above methods seem to be tedious and expensive to obtain CeO₂ nanoparticles.

It is reported that nanoparticles can be prepared in an easy manner using a domestic microwave oven [15]. This method has been successfully applied for the preparation of nanosized inorganic materials [16-18]. Compared with conventional heating, microwave heating has an advantage of high efficiency and rapid formation of nanoparticles with a narrow size distribution. This work reports the studies of ceria nanoparticles synthesized by microwave-assisted solution method from an aqueous solution containing ammonium ceric nitrate and sodium hydroxide.

Experimental

All chemicals were analytical grade (AR) and used without further purification. In the synthesis of CeO₂ nanoparticles, the precursor ammonium Ce(IV) nitrate ((NH₄)₂Ce(NO₃)₆) was dissolved in deionized water and pH value was adjusted to be 10 using sodium hydroxide. A chemical reaction took place in the solvent and a pale yellow precipitate was formed. Then the prepared mixture solution was kept at a temperature of 70⁰C for about for 30 minutes in air in a domestic microwave oven (900 W, 2450 MHz., Onida, India). Pale yellow-coloured precipitate was formed in the solution after the microwave heating. Synthesized pale yellow precipitate was filtered and washed with de-ionized water and it was dried at 95⁰C for 8h to obtain as-prepared powder. Conventional thermal treatment of as-prepared powder at 200⁰C in air for 2 h resulted in the formation of CeO₂ nanoparticles.

The powder XRD pattern of the synthesized sample was taken using a powder X-ray diffractometer (Model:Ritz-170 with Nickel filtered CuK_α radiations (1.54056 Å, 35KV,10 mA). The particle size (d) of the sample can be estimated from XRD pattern by applying the full – width at half- maximum (β) to the Debye-Scherrer's relation $d = (0.98 \lambda) / (\beta \cos \theta)$ where λ is the X-ray wavelength and θ is the diffraction angle . The SEM image of the synthesized nanopowder of ceria was recorded using a Hitachi Scanning Electron Microscope.



Results and Dissusion

Figure 1 shows the XRD pattern of the sample. From this figure, the characteristic peaks located at $2\theta = 28.5, 33.1, 47.5, 56.2$ and 50.0° are corresponding to (111), (200), (220), (311) and (222) planes respectively. These match well with the peaks of cubic fluorite crystal structure.

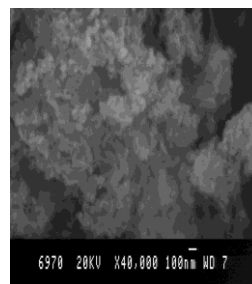
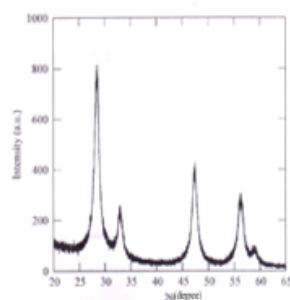


Fig.1: Powder XRD pattern of ceria nanoparticles & Fig.2: SEM image of ceria nanoparticles

For the various reflection peaks of the XRD pattern, the particle size was estimated using the Debye-Scherrer's relation and the average size of nanoparticles of the samples was found to be around 12 nm. The Scanning Electron Microscope (SEM) image of the sample was used to identify the morphology of the nanoparticles. The SEM image of the synthesized ceria nanoparticles is displayed in the figure 2. It is observed that most of the particles are agglomerated. Hence the shape of a single nanoparticle is not clear from the SEM image.

Fourier Transform Infrared (FTIR) spectrometer is the sophisticated instrument which can be used to identify the functional groups of samples of nanomaterials, crystals and other types of materials. When an infrared radiation is passed through a sample, certain percentage of intensity of the radiation would be absorbed by the sample and that will be indicated in the FTIR spectra. The absorption of IR radiation in the sample is due to stretching and bending vibrations. Depending on the material of the sample, absorption of IR radiation will occur at certain frequencies. An FTIR spectrum is recorded between percentages of transmittance (%T) and wave number of IR radiation. By observing the absorption bands or peaks in the wave number range 400 cm^{-1} to 4000 cm^{-1} of FTIR spectrum, one can ascertain the functional groups of the sample and hence the chemical formula and the sample can be identified.



The FTIR pattern of cerium dioxide nanoparticles is shown in the figure 3. The broad absorption band located around 3400 cm^{-1} corresponds to the O–H stretching vibration of residual water and hydroxyl groups, while the absorption band at 1630 cm^{-1} is due to the scissor bending mode of associated water. The complex bands observed at about 1518, 1350, 1053 cm^{-1} are due to unwanted residues in the sample. The band at 848 cm^{-1} corresponds to metal – oxygen bond. The assignments for the bands/peaks of FTIR pattern were the assignment for the various absorption peaks of the spectrum are provided in the table 1.

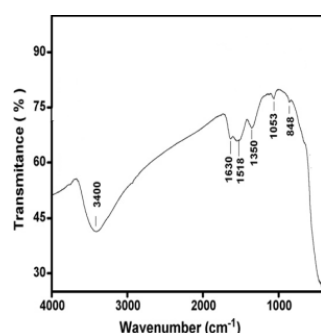


Fig.3: FTIR pattern of cerium dioxide nanoparticles

Table 1 : Assignments for absorption bands of FTIR spectrum of cerium dioxide nanoparticles

Bands (cm-1)	Assignments
3400	OH stretching
1630	OH bending
1518	CH ₂ bond
1350	CH ₂ bond
1053	-
848	Metal-O bond

Conclusion

Nanocrystalline CeO₂ (ceria) particles have been synthesized by microwave -assisted solution method using ammonium ceric nitrate as the precursor. Sodium hydroxide played an important role in forming nanoparticles of ceria. The average size of nanoparticles of the sample was

estimated by powder XRD studies. SEM image revealed the morphology of nanoparticles. By observing the absorption bands or peaks in the wave number range 400 cm^{-1} to 4000 cm^{-1} of FTIR spectrum, one can ascertain the functional groups of the sample and hence the chemical formula and the sample can be identified.

References

- [1] E.PerryMurray, T.Tsai, S.A.Barnett, Nature 400 (1999) 649.
- [2] R.X.Li, S.Yabe, M.Yamashita, S.Momose, S.Yoshida, S.Yin, T.Sato, SolidStateIonics. 151 (2002) 235
- [3] M.G. Sanchez, J.L. Gazquez, J. Catal. 104 (1987) 120
- [4] M. Jiang, N.O. Wood. R. Komanduri, Wear 220 (1998) 59
- [5] N. Izu, W. Shin, N. Murayarna, S. Kanzaki, Sensor Actuat. B 87(2002) 95
- [6] S. Yabe, T. sato, J. Solid state Chem 171(2003) 7
- [7] P.L. Chen, I.W. Chen, J.Am. Ceram. Soc. 76(1993)1577
- [8] B. Djuricic, S. Pickering, J.Euro. Ceram. Soc.19 (1999)1925
- [9] X.D. Zhou, W. Huebner. H.U.Anderson. Appl.Phys.Lett. 80(2002)3814
- [10] N. C. Wu, E. W. Shi, Y. Q. Zheng, W. J. Li, J. Am.Ceram. Soc.85(2002)2462.
- [11] M. Hirano, E. Kato, J. Mater. Sci. Lett. 15(1996)1249
- [12] L.P.Li, X.M.Lin, G.S.Li, H.Inomata, J.Mater.Res.16(2001)3207.
- [13]T.Masui, K.Fujiwara, K.I.Machida, G.Y.Adachi, T.Sakata, H.Mori, Chem.Mater. 9(1997) 2197
- [14] S.Komarneni,R.Rajha,Mater.Chem.Phys.61(1999)50.
- [15] M.Brightson, S.Meenakshi Sundar, T.H.Freeda, P.Selvarajan, Proceedings of Second Int. Conference on emerging adaptive systems and technologies(EAST-2007), Noorul Islam College of Engineering, Tamil Nadu, 25th to 27th, October, 2007.
- [16] X.H.Liao,J.J.Zhu,H.Y.Chen,Mater.Sci.Eng.B85(2001)85.
- [17] W.X.Tu,H.F.Liu,J.Mater.Chem.10(2000)2207.
- [18] H.Wang,J.Z.Xu,J.J.Zhu,H.Y.Chen,J.Cryst.Growth244(2002)88.



Studies on molecular interactions of Bromoform and Ethyl bromide with Benzene at four different temperatures

K. Umamakeshvari¹ and U. Sankar^{2*}

¹Assistant Professor, Department of Physics, St. Johns College, Palayamkottai, India.

²Associate Professor, Department of Physics, Sri KGS Arts College, Srivaikundam, India.

*Corresponding Author E-mail:ksusankar@gmail.com.

Abstract

Molecular interactions can be studied by dielectric measurements by virtue of the influence of local order and the overall dipole moment. The short range interaction between permanent dipoles could readily be described by the Kirkwood-Frolich correlation factor in dilute solutions of bromoform and ethyl bromide with inert solvent. The interactions between the solute species among themselves may be given by the modified form of the correlation factor g' by not taking into account of solvent-solvent interactions. The dielectric constants of the binary mixtures were measured at 303, 308, 313 and 318K. The results were interpreted in light of the theory. The nature of interactions was identified in both the systems.

Keywords: Dielectric constant, Kirkwood correlation factor, H-bond, Multimers

Introduction

Dielectric studies are of great help in the assignment of the molecular structures or configurations, particularly those of organic compounds. Although infrared (IR), ultrasonic and nuclear magnetic resonance (NMR) studies are the powerful tools for studying intermolecular H- bonds, dielectric studies provide very useful information about molecular association and intermolecular rotation. Determination of the modified Kirkwood correlation factor (g) provides the information about intermolecular association among the associating molecules (Purohit H D et al., 1991). Ethyl bromide is used as a solvent, as an anesthetic in medicine, as a refrigerant, as a fumigant. It is a ethylating agent in organic synthesis. It is possible to reconcile the data obtained

from dipole moment studies of complexes of alcohols with ethyl bromide (T. Indira *et al.*, 2009). They have found that the enhancement of the dipole moment value confirms hydrogen bonding between alcohol molecules and benzene with alcohol. The survey of literature shows that very little work on esters (L.Eberson *et al.*, (1969) has reviewed the various types of hydrogen bonding in carboxylic acids and esters. Bromoform was used as a solvent, sedative, and flame retardant, but now it is mainly used as a laboratory reagent. Its high density makes it useful for separation of minerals by density. Some work on ultrasonic studies of bromopropane with benzene mixture was reported (S S Yadava *et al.*, 2004). Benzene is a colorless liquid with sweet odor. Use benzene, to make other chemicals which are used to make plastics, resins, nylon and synthetic fibers. In this context, the variation of linear correlation factor was studied with composition and temperature for the binary systems (acetic acid+ benzene, methyl acetate + benzene and ethyl-methyl ketone+ benzene) carried out the dimeric state of acetic acid is due to self-association (Krishnan *et al.*, 1997). The following binary systems Bromoform in Benzene (I), Ethyl bromide in benzene (II), were studied based on Kirkwood-Frohlich model.

Materials and Methods

Ethyl Bromide (AR grade), Bromoform (AR grade) and Benzene (AR grade) were commercially obtained from S D Fine-chem. Limited (India) and used without further purification. Binary mixtures of Ethyl bromide, Bromoform and benzene were prepared at 5 different concentrations by volume fraction. Assuming ideal mixing behaviour the concentration was converted into the molefraction (Prajapati *et al.*, 2010). The dielectric constant was measured at 1 KHz using a Systronix Digital LCR meter 925. The scale of the instrument was calibrated using standard liquids like carbon tetrachloride, benzene, toluene and chlorobenzene.

The temperature was maintained at 298 ± 1 K using Sigma constant temperature bath. The refractive indices were measured using Abbe's refractometer. Densities were determined using a 10ml specific gravity bottle and a K-Roy microbalance. The uncertainties in the measurement of dielectric constants, refractive indices and densities were ± 0.0001 , ± 0.0002 and ± 0.0001 gm/cc respectively.

Theory

Attractive forces, dipole-dipole interactions and other slowly varying interactions play a

role in the structure of the liquids. The modern theories of liquids show that the repulsive intermolecular forces dominate the structure of the denser liquids. In the case of associated liquids it is almost impossible to account for their dielectric behavior in the continuum approach and one has to recourse to the theories based on the statistical mechanical approach of the dielectric constants. Theoretical interpretations of the measured dielectric constants of associated liquids were enhanced by the Kirkwood's theory of dielectric polarization (Kirkwood., 1939) which was later modified by Frohlich (Frohlich., 1958). The Kirkwood-Frohlich treatment takes care of short range correlations like hydrogen bonding through the introduction of the dimensionless correlation parameter g' .

The interactions between the polar solute and the non-polar solvent may be considered by a modification of the Kirkwood correlation factor, which takes into account the interactions between the solvent molecules among themselves. If g' is the linear correlation factor of dielectric polarization between the solute and the solvent species, one can write (Kirkwood.,1939).

$$g' = [B(T) - W_1 B_1(T)] \frac{27KM_2}{(n^2+2)^2 4\pi N_1 W_2 \langle \mu_2^2 \rangle} \quad \text{-----} \quad 1$$

$$B(T) = \frac{(\epsilon - n^2)(2\epsilon + n^2)T}{3\epsilon P} \quad \text{-----} \quad 2$$

$$B_1 = \frac{(\epsilon_1 - n_1^2)(2\epsilon_1 + n_1^2)T}{3\epsilon_1 \rho_1} \quad \text{-----} \quad 3$$

where ϵ, n and ρ represent the static dielectric constant, refractive index and the density of the solution respectively and the suffix 1 indicates the solvent, k is the Boltzmann constant, $\langle \mu_2^2 \rangle$ is the squared dipole moment of the polar species, w_1 and w_2 are the weight fractions of the solvent and solute, M_2 is the molecular weight of the polar solute and N_A is the Avogadro number. The value of g' can be determined for different concentrations by measuring the dielectric constant, refractive index and density of the solutions.

Results and Discussion

The variation of density, refractive index, dielectric constant and Kirkwood-Frohlich correlation factor g' with concentration of the liquids at different temperatures for the system I and II are given in Table 1 and 2. The value of g' is calculated using Eqn (1). The variation of g' with x_2 is graphically represented in Fig 1. From the Tables 1 and 2, the dielectric constant value increases with concentration of the solute and also decreases with the increase of temperature. In pure liquids, the solute molecules do not exist as clusters. On dilution, the solute molecule exists as clustered species with a little dipole moment larger than the gas phase moment. As more and more solvent is added, the clusters become very smaller, until reaches a non-hydrogen bond. The cluster sizes vary with the volume fraction. Therefore the dielectric constant increases with the increase of volume fraction (Kroeger *et al.*, 1987).

With the increase of temperature the dielectric constant value of all studied systems at various concentrations decreases. Due to the thermal agitation, the orientation of the molecules is disturbed. So the dielectric constant value decreases with the rise of temperature. Similar conclusions were reported by many researchers (Kroeger *et al.*, 1987 to Botcher *et al.*, 1973). The value of correlation factor g' decreases on increase of concentrations. For all the studied systems, for all temperatures, the g' value decreases with increase of concentrations. The deviation of g' value from unity is the measure of the molecular interactions. The value of g' greater than unity implies the parallel orientation of the dipoles. The value of g' less than unity implies the anti-parallel orientation of the dipoles. In the system I, g' greater than unity is obtained up to the concentration of 0.2050 at 308K, this implies the parallel orientation of the dipoles, formation of α -multimers and γ -multimers. The formation of linear multimers is favoured as proposed by Cole and Dannhauser (Cole *et al.*, 1955).

The rotation about the hydrogen bond is more restricted, the correlation between the dipoles in chain increases, leading for this type of molecules to higher values of g' . As dilution decreases, g' decreases. This may be explained as follows: with the decrease of dilution, more solute molecules may be available for the interaction with solute molecules. This may lead to the rupture of the H-bonds between the solute

molecules and the solute molecules may tend to interact with the solvent molecules through a weak H-bond. Afterward the value of g' less than unity are obtained. This implies the anti-parallel orientation of the dipoles, formation of β - multimers. Increase of dilution, the g' value decreases due to the self-association of solute molecules through H-bonding (Bordewijk *et al.*, 1973).

At high dilution, as temperature increases, solute-solute interaction may be less favoured due to hindrance of the solvent molecules. This results in favour of more solute-solute interactions. Increase of temperature at very high dilutions may increase the size of the molecules (linear multimers) favouring parallel orientation of the solute molecules, which may be the reason for the increase of g' values with the temperature. Large deviation of g' value from unity indicates the strong self-association among the solute molecules. The strength of the solute-solute interactions in bromoform with benzene mixture is higher than the ethyl bromide-benzene mixture. Hence it may be concluded at 303 and 308K for system I, parallel orientation among solute molecules exists. At 313 and 318K g' of system I varies about 10 to 17 percent. This indicates there is no self association between solute molecules through H-bonding. This shows the absence of short-range interaction between the solute molecules. The solute molecules may exist in monomeric state. Small deviation of g' values from unity may be due to dipole-dipole interaction (long-range) as well as π - π interaction between the solute and solvent.

There may be a weak π - π interaction between the π electron clouds of benzene with the oxygen atom of the esters. g' does not vary appreciably with x_2 as well as with temperature. Deviation of g' value from unity up to 20% can be taken as due to long-range interactions as well as the π - π interactions (Thenappan., Sankar., 2006). In system II at 0.0519 concentration g' value is above 1 indicating parallel orientation at all temperatures. For all other concentration and all temperatures g' value is less than 1 indicating antiparallel orientation.

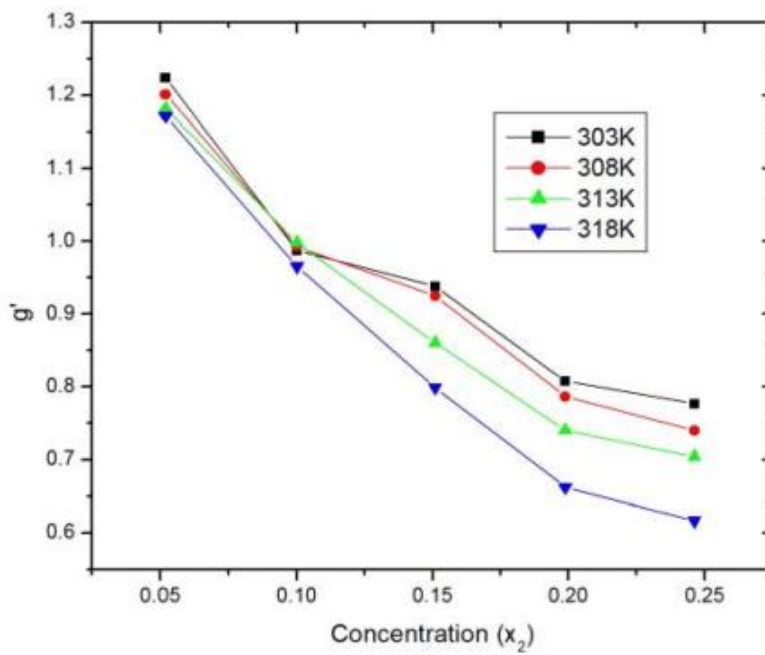
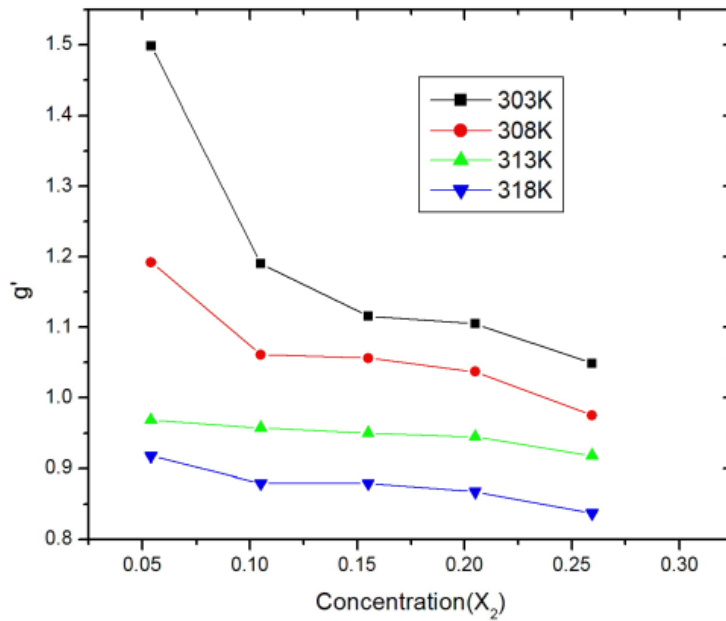


Fig.1- Variation of g' with concentration:
System I-Bromoform in benzene
System II-Ethyl bromide in benzene

Table 1 - Variation of density, refractive index, dielectric constant and g' with concentration at four different temperature of bromoform (X₂) + Benzene binary mixtures

Temperature (K)	X ₂	d gm/cc	n	ϵ_1	g'
303	0.0539	1.0491	1.5019	2.3576	1.4983
	0.1050	1.0787	1.5045	2.4447	1.1904
	0.1550	1.1785	1.5076	2.5215	1.1160
	0.2050	1.2777	1.5132	2.6151	1.1051
	0.2595	1.3911	1.5188	2.7000	1.0489
308	0.0539	1.0379	1.4942	2.3342	1.1922
	0.1050	1.0675	1.5012	2.4113	1.0611
	0.1550	1.1673	1.5062	2.4981	1.0564
	0.2050	1.2665	1.5114	2.5817	1.0369
	0.2595	1.3799	1.5164	2.6556	0.9753
313	0.0539	1.0283	1.4928	2.3108	0.9682
	0.1050	1.0579	1.4972	2.3810	0.9571
	0.1550	1.1578	1.5029	2.4607	0.9497
	0.2050	1.2569	1.5068	2.5349	0.9445
	0.2595	1.3704	1.5126	2.6151	0.9181
318	0.0539	1.0180	1.4902	2.2974	0.9174
	0.1050	1.0478	1.4939	2.3576	0.8796
	0.1550	1.1479	1.4983	2.4279	0.8796
	0.2050	1.2472	1.5035	2.4981	0.8674
	0.2595	1.3608	1.5090	2.5683	0.8372

Table 2- Variation of density, refractive index, dielectric constant and $g\phi$ with concentration at four different temperatures of Ethyl bromide(X2)+ Benzene (X1)binary mixtures.

Temperature (K)	X ₂	d gm/cc	n	ϵ_1	g'
303	0.0519	0.8954	1.4912	2.6151	1.2236
	0.1002	0.9208	1.4918	2.8492	0.9873
	0.151	0.9445	1.4882	3.1326	0.9379
	0.1989	0.9694	1.4864	3.2705	0.808
	0.2461	0.9904	1.4814	3.4812	0.7766
308	0.0519	0.8842	1.4895	2.5917	1.2008
	0.1002	0.9096	1.4889	2.8258	0.9925
	0.151	0.9333	1.4874	3.0896	0.9249
	0.1989	0.9582	1.4832	3.2003	0.7866
	0.2461	0.9792	1.4762	3.3641	0.7399
313	0.0519	0.8745	1.4872	2.5683	1.1809
	0.1002	0.9	1.4855	2.8024	0.998
	0.151	0.9237	1.4832	2.9896	0.8602
	0.1989	0.9486	1.4793	3.1003	0.7403
	0.2461	0.9697	1.4738	3.2641	0.704
318	0.0519	0.8643	1.4836	2.5449	1.1714
	0.1002	0.8899	1.4819	2.7556	0.9656
	0.151	0.9138	1.4784	2.896	0.7991
	0.1989	0.9389	1.4762	2.9662	0.6621
	0.2461	0.9601	1.4704	3.0833	0.6167

References

- Ajay Chaudhari, Anita Das, Garigipati Raju, Harish Chaudhari, Prakash Khirade, Navinkumar Narain and Suresh Mehrotra, *Proc. Natl. Counc. Roc (A)*, 25 (2001) 205-210.
- Ajay Chaudhari, Raju, G S., Anita Das., Harish Chaudhari, Narain and Suresh Mehrotra, *Indian J Pure & Appl Phys*, 39 (2001) 180.
- Bordewijk, P., Kunst, M, and Rip, A., *J Phys Chem*, 77 (1973) 548.
- Bottcher, C J F., Theory of Dielectric Polarization, Vol I, Elsevier, Amsterdam (1973),
Ebersson, L. Carboxylic Acids and Ester. Patai, *Interscience*, 1969.
- Frohlich H., *Theory of dielectrics*, (Clarendon Press, Oxford), 1958.
- Indira, T., Parthipan, G., Aswathaman, H., Thenappan, T, *J Mol. Liquids*, 150 (2009) 22-24.
Kirkwood J G, *J Chem Phys*, 7 (1939) 911.
- Krishnan, S., Kanagasabapathy, K, *Lett. Asian Chem*, 1(1) (1997) 37.
Kroeger, M K., *J Mol. Liquids*, 36 (1987) 101-108.
- Manda, H., Frood, D G., Habibullah, M., Humeniuk, L., & Walker, S. *J Chem Soc*, 85 (1989) 3145.
- Prajapati A N, Vyas A D, Rana V A & Bhatnagar S P, *Journal of Mol Liquids*, 151 (2010) 6.
Purohit H D & Sengwa R J, *J Polym Mater*, 8 (1991) 317.
- Sengwa, R J., & Purohit, H D., *Poym. Int.*, 29 (1992) 25.
Thenappan, T., Sankar, U., *J Mol Liquids.*, 126 (2006) 23-28.
- Vir Singh Rangra., & Sharma, D R., *Indian J Pure & Appl Phys*, 41 (2003) 630-633.
Vyas, A D., & Vashisth, V M., *J Mol Liquids*, 38 (1988) 11-22.
- Yadava, S S., Aniruddh Yadav, *Indian J Pure & Appl Phys*, 42 (2004) 338-340.





Volume: 2; Issue: 3 [Special Issue]; March-2016; pp 472-477. ISSN: 2454-5422

Z - Scan measurement and impedance analysis of L-alanine alaninium nitrate single crystals (LAAN)

R. Jothi mani^{1*}, P. Selvarajan² and C.Parvathiraja¹

¹Department of Physics, Sadakathullah Appa College, Tirunelveli, India.

²Department of Physics, Aditanar College of Arts and Science, Tiruchendur, India.

*Corresponding Author E-mail: mariajothi@gmail.com

Abstract

L-alanine alaninium nitrate (LAAN) crystal is a semi-organic nonlinear optical material. XRD analysis confirmed the monoclinic structure of LAAN crystal. SHG efficiency of the sample show good value. Third order nonlinear optical studies using z-scan technique is done to find open and closed aperture of LAAN crystal in order to estimate the nonlinear optical parameters. The impedance analysis was also carried out for the sample to find out various electrical properties as a function of frequency and temperature.

Keywords: Single crystal; XRD; Impedance; Third-order NLO; SHG

Introduction

Organic crystals with large second-order and third-order nonlinear susceptibilities are of great interest because of their potential use in optical parametric amplifier and oscillator in the infrared region. Among the amino acids the L-alanine is a well-known organic nonlinear optical material which has been examined by several researchers in the recent past on its crystal growth and properties. The Z-scan technique is a popular method for the measurement of optical nonlinearity of the material. It has the advantage of high sensitivity and simplicity and is used to measure the third order nonlinear optical parameters. Impedance spectroscopy is a powerful technique for the characterization of electrical behavior of optical material. This technique analyzes the ac response of a system to a sinusoidal perturbation and subsequent calculation of

the impedance as a function of frequency of the perturbation. The output response, when plotted in a complex plane, appears in the form of a succession of semicircle representing electrical phenomena due to bulk material, grain boundary effect and interfacial phenomena.

Nucleation kinetics parameters, solubility, growth, hardness parameters, XRD analysis, dielectric analysis, etching studies and nonlinear optical analysis of L-alanine alaninium nitrate single crystals grown by slow cooling technique is already reported for the first time by R.Jothi Mani, et al. In this work impedance analysis and Z scan measurements of LAAN sample is discussed for the first time.

Materials and Method

L-alanine and nitric acid was taken in 2:1 molar ratio to synthesis LAAN sample. Calculated amount of reactance was dissolved in double distilled water and stirred well to get homogeneous solution. Crystallization was allowed to take place in a constant temperature bath (accuracy ± 0.01 °C) by slow cooling method. It is observed that the grown crystals are transparent, colourless and it is well formed with sharp edges (figure 1).

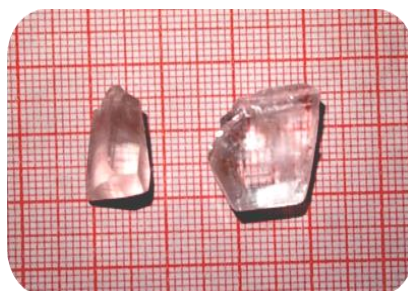


Figure 1: Harvested crystals of LAAN

Results and Discussions

Second Harmonic Generation analysis

The generation of second harmonics was confirmed as the LAAN crystal is found to produce green light of halved wavelength (532 nm) when it is irradiated by fundamental wavelength ($\lambda = 1064$ nm) of Nd:YAG laser. It is observed from this study that the relative SHG efficiency of grown sample is 2.1 times that of the reference KDP crystal.

Third Harmonic Generation analysis

Third-order NLO studies were carried out by Z-scan technique. It is a standard technique for determining the nonlinear index of refraction (n_2), nonlinear susceptibility ($\chi^{(3)}$) and nonlinear

absorption coefficient (β). This method depends on the position (Z) of the thin sample under the investigation along a focused Gaussian laser beam. Measurements of open and closed aperture of the normalized transmittance is made in order to estimate the intensity dependence of nonlinear absorption and nonlinear refraction process and the curves are shown in figure:2

This technique is also useful to find the sign of nonlinear refractive index (n_2). The negative nonlinear refractive index of the sample shows transmittance peak followed by transmittance valley, similarly the positive nonlinear refractive index shows the transmittance valley followed by transmittance peak.

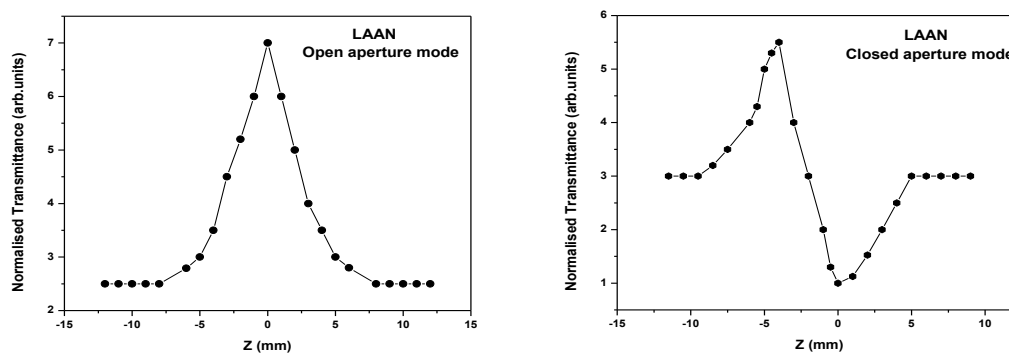


Figure 2 : Open and closed aperture mode of LAAN sample

The formulas for calculating nonlinear optical parameters are already explained in literature[8]. The nonlinear absorption (β) and nonlinear refractive index (n_2) of the crystal has been measured in open and closed aperture curves respectively. The negative sign values of nonlinear refractive index ($n_2 = 6.476 \times 10^{-10} \text{ cm}^2/\text{W}$) reveals the self-defocusing nature, the nonlinear absorption coefficient ($\beta = 10.60 \times 10^{-5} \text{ cm/W}$) value exhibits the two-photon saturation absorption process of sample. And third-order nonlinear susceptibility ($\chi^{(3)} = 4.489 \times 10^{-6} \text{ (esu)}$) is due to the π -electron cloud movement from the donor to the acceptor of the grown crystal. Z-scan data of LAAN shows that the sample has better third order nonlinear optical property and produces higher energy for optical applications.

Impedance Analysis

Impedance spectroscopy is a powerful technique for the characterization of electrical behavior of NLO material. The complex impedance of the sample demonstrated as the sum of the single RC circuit with parallel combination. Figure: 3 shows the real (Z') and imaginary (Z'') part of impedance (resistor and capacitor behavior) and both are decrease with rise in frequency and

temperature and gives indication of increasing conduction with temperature and frequency. The coincidence of the impedance (Z') at higher frequencies at all the temperatures indicates a possible release of space charge. A Nyquist plot (complex impedance spectrum) of LAAN at different temperatures shows (figure: 4) the transport response function. Characteristically, one semicircular arcs and spikes have been observed. The low frequency semicircle is considered due to the grain boundary (blocking core) whereas the higher frequency semicircle depicts the bulk effect. This bulk effect arises due to the parallel combination of bulk resistance (R_b) of LAAN material. The values of bulk resistance (R_b) and grain boundary resistance (R_{gb}) at different temperatures have been obtained from the intercept of the semicircular arc on the real axis (table 1).

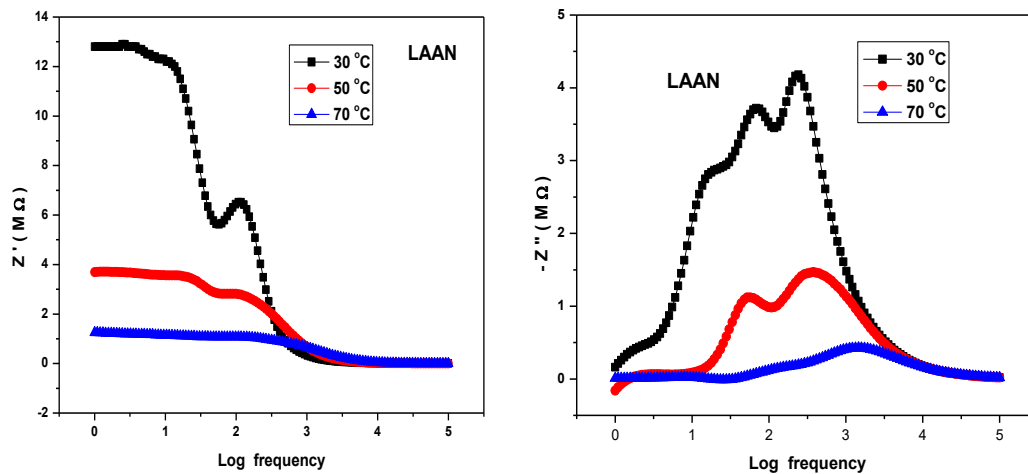


Figure 3: Variation of real and imaginary part of impedance (Z' and Z'') with frequency

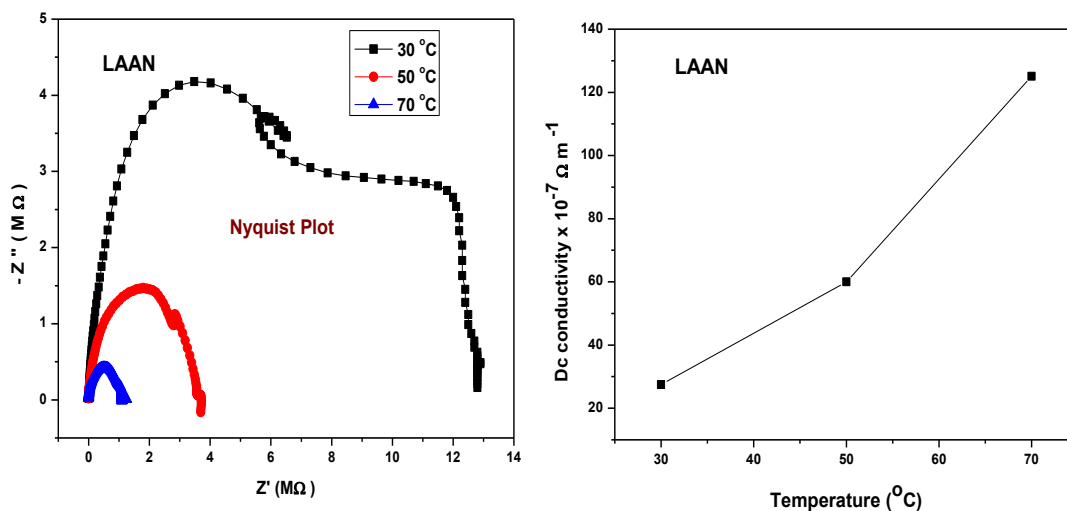


Figure 4: Nyquist plot and variations of Dc conductivity with temperature for LAAN sample

It is found that the values of R_b and R_{gb} decreases with rise in temperature. This shows the negative temperature coefficient of resistivity (LAAN) behavior like that of insulator.

Table: 1

Temperature $^{\circ}\text{C}$	Bulk resistance R_b (ohm)	Grain boundary resistance R_{gb} (ohm)
30	5.54×10^6	3.48×10^6
50	3.70×10^6	1.91×10^6
70	1.17×10^6	0.58×10^6

The dc conductivity values (figure: 4) found by the formula $DC = d/AR$ (ohm m^{-1}) show increase in conductivity with increasing temperature. The electrical relaxation process occurring in the material has been found to be temperature dependent

Conclusion

A nonlinear optical LAAN crystal was grown by slow cooling technique for the first time. SCXRD analysis confirmed the monoclinic structure with non-centrosymmetric space group of the sample. Nonlinear optical analysis was carried out by Kurtz powder technique and Z-scan measurements. Electrical properties were determined by Impedance analysis. All the above analyses shows that LAAN sample is promising NLO material for optoelectronic applications.

Acknowledgement

The authors are grateful to the Department of Science and Technology (DST), Government of India for the financial support (Major project approval No.SR/S2/LOP-0018/2010) to carry out this work. Also the authors are thankful to the management of Aditanar College of Arts and Science, Tiruchendur for the encouragement given to us to carry out the research work. PSN Engg college Tirunelveli, Crescent Engg College Chennai, SAIF cochin and VIT Vellore are gratefully acknowledged for their support.

Reference

S.X. Dou, D. Josse, J. Zyss, J. Opt. Soc. Am. B **10**, 1708 (1993).

Lydia Carolin et al, Materials Chemistry and Physics 114 (2009) 490.

Vimalan M., Ramanand A., Sagayaraj P., Cryst. Res. Tech. 42 (2007) 1091.

Lucia Rose S.J., Selvarajan P., Perumal S., Mater. Chem. Phys., 130 (2011) 950.



Sabari Girisun T.C, Dhanuskodi S., Cryst. Res. Technol. 44 (2009) 1297.

Bharath D., Kalainathan S., Spectrochimica Acta Part A: 120 (2014) 32.

Jothi Mani R., Selvarajan P. et al, Int. J. Adv. Sci. Tec.Res., 3 (2013) 2249.

Jothi Mani R., Selvarajan P. et al, Int.J. Sci. Engi. App. Special Issue, (2014) 83.

Banarji Behera et al, J. Alloys and Compounds 436 (2007) 226.

Arun K.J., Jayalekshmi S., J. Minerals & Materials Charac.Engi. 8 (2009) 635.





Studies on optical and mechanical properties of dl-malic acid doped ADP single crystals

I.Stella Jeya Christy¹, A. Effie Cordelia¹ and S. Perumal²

¹Department of Physics, Sarah Tucker College (Autonomous), Tirunelveli, India.

²Physics Research Centre, S. T. Hindu College, Nagercoil, India.

Abstract

Nonlinear optical single crystals of DL malic acid doped Ammonium Dihydrogen Phosphate were grown by slow evaporation solution growth method. The grown crystals were characterized using X-ray diffraction studies. The possible functional groups present were identified using Fourier Transform Infrared Spectroscopy. Optical parameters like transmittance, absorbance, reflectance, optical absorption co-efficient, refractive index, extinction co-efficient, band gap energy, optical conductivity, electrical conductivity, electrical susceptibility and real and imaginary parts of dielectric constant of the crystal were estimated from UV-Vis-NIR spectrum. SHG efficiency was checked using Kurtz-Perry powder technique. Third order nonlinear refractive index, nonlinear absorption co-efficient and third order susceptibility had been calculated from Z-scan technique. Mechanical parameters such as work hardening co-efficient, yield strength, elastic stiffness constant, fracture toughness and brittleness index were obtained using Vicker's microhardness studies.

Key Words: Solution growth, FTIR, UV-Vis-NIR spectrum, SHG, Z-scan technique, Vicker's micro hardness

Introduction

Ammonium Dihydrogen Phosphate, which is an important isomorph of Potassium Dihydrogen Phosphate crystal, has been widely used for frequency conversion in laser systems, optical switches and acousto optical devices. This hydrogen bonded compound also exhibits piezo electric activity and low temperature order-disorder phase transition. Below 148.5K, ADP is

ferroelectric and belongs to $P2_12_12_1$ space symmetry group while above this temperature, it paraelectric having $I4/2d$ symmetry [1]-[3]. This is also nonlinear optical material having applications in the field of photonics for frequency mixing, parametric amplification and electro optic modulation. DL-malic acid is an organic material which is chosen to be doped with ADP. Because of this attempt, the SHG efficiency of ADP is found to increase so that we arrive at better advantage of using these doped crystals in photonics and related fields.

Experimental Work

The commercially available AR grade chemicals ADP and DL-malic acid were purchased and 2mole% of DL-malic acid is dissolved in deionized water together with calculated amount of ADP. The solution is put in magnetic stirrer for about four hours to get highly homogenous mixture and filtered. After leaving it in dust free undisturbed atmosphere for three weeks, colourless transparent single crystals had been harvested. Out of these, fine crystals were selected and characterized. The photograph of the grown crystal is given in fig.1

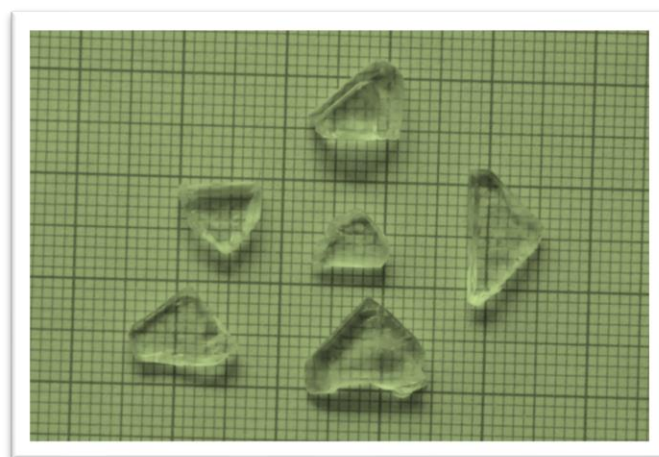


Figure 1. Photograph of the grown crystal

Results and Discussion

FTIR SPECTRAL ANALYSIS

BRUKER IFS 66V FTIR Spectrometer was used to record the FTIR spectrum of the grown crystal. The spectrum was given in fig.2 and the corresponding assignments [4],[5] are given in table1.

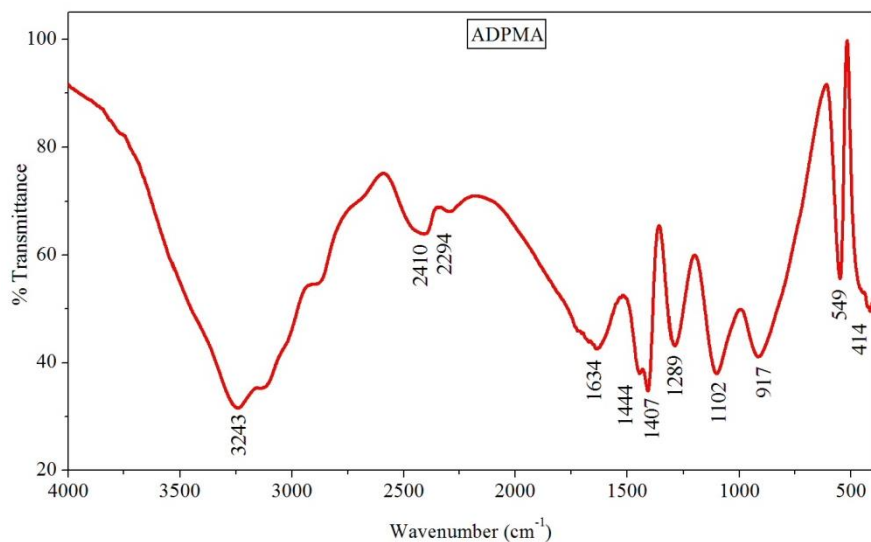


Fig. 2.FTIR Spectrum

Table 1-FTIR assignments

wavenumber in cm ⁻¹	FTIR assignments
3242	O-H stretching, P-O-H stretching , N-H vibrations of ammonium
2410	band due to hydrogen bond
2294	combination band
1634	O-H bending of water
1444	H-H bending of NH ₄
1407	bending vibrations of ammonium
1289	CH ₂ rocking vibration
1102	P-O-H vibrations
917	P-O-H vibrations
549	PO ₄ vibrations
414	PO ₄ vibrations



UV-VIS-NIR SPECTRAL STUDIES

Optical transmission spectrum of the crystal was recorded using Lambda 35 spectrophotometer in the wavelength region 400-1100nm and is shown in fig.3.

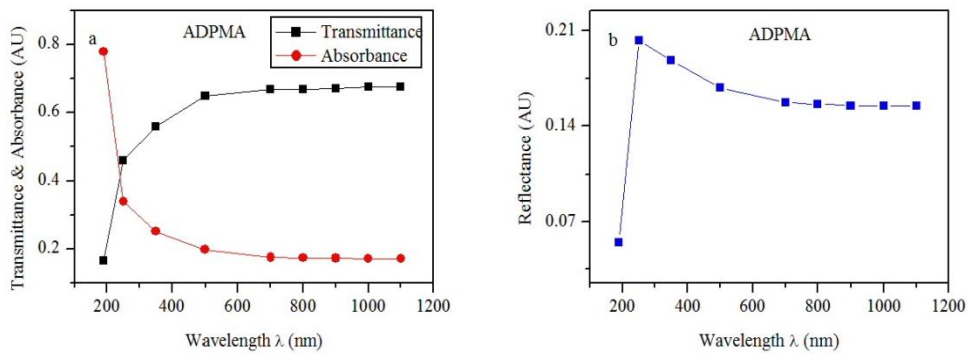


Fig.3.transmittance, absorbance and reflectance as function of wavelength

Good transmittance for a wider region of wavelength is the required condition for device fabrication and this is achieved here. The cut off wavelength in the UV region is found to be 280 nm. and the band gap energy from Tauc’s plot in fig.4 is 4.5 e V .[6],[7].The variation in the refractive index(n) of the crystal with wavelength is plotted in fig.5 .

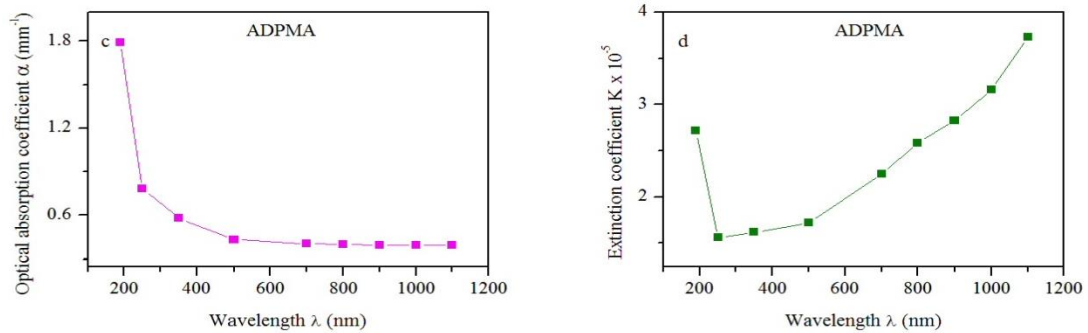


Fig.4.Optical absorption coefficient and extinction coefficient versus wavelength

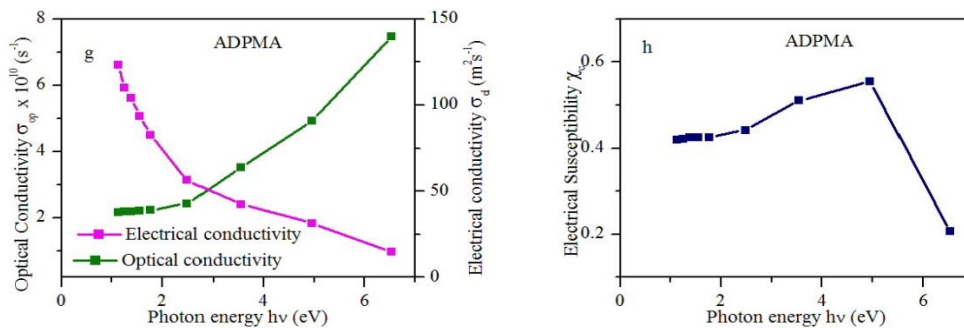


Fig.5.Variation of optical and electrical conductivities and electrical susceptibility with photon energy



The calculated values of extinction co-efficient (K), optical conductivity (σ_{op}), electrical conductivity (σ_{el}), electrical susceptibility (χ_c), real and imaginary parts of dielectric constant at $\lambda=700\text{nm}$ are estimated and tabulated as below in table 2.

Table 2 – Optical parameters of the crystal

Extinction co-efficient	2.241×10^{-5}
optical conductivity	$2.22 \times 10^{10} \text{s}^{-1}$
electrical conductivity	$82.74 \text{m}^2 \text{s}^{-1}$
Electrical susceptibility	0.4247
R.P.of dielectric constant	5.338
I.P.of dielectric constant	10.365×10^{-5}

Z- SCAN TECHNIQUE

When a third order material is translated along a focused Gaussian laser beam, its index of refraction changes causing focusing or defocusing of the beam. By properly monitoring the transmittance change through a small aperture at the far field position (closed aperture), one is able to determine the amplitude of the phase shift. By moving the sample through the focus and without placing an aperture at the detector (open aperture), one can determine the intensity dependant absorption of the sample.

He-Ne laser beam with wavelength 632.8nm was used and it was focused using a convex lens of focal length 18.5 cm. The optically polished 1mm thick crystal was translated along Z-axis. The input energy and energy transmitted by the sample were measured using a power meter. The normalized transmittance for the positioned sample was measured at different positions and was used to calculate the third nonlinear optical property of the materials [8],[9]. The Z- scan curves in both open and closed aperture modes are illustrated in fig.6 and fig.7 respectively. The calculated values of the third order parameters are,

nonlinear refractive index (n_2) = $2.6245 \times 10^{-11} \text{cm}^2/\text{W}$,

nonlinear absorption co-efficient(β) = $7.512 \times 10^{-6} \text{cm}/\text{W}$,

the real and imaginary parts of the third order susceptibility $\text{Re } \chi^3 = 3.601 \times 10^{-5} \text{esu}$,

$\text{Im } \chi^3 = 5.193 \times 10^{-3} \text{esu}$.

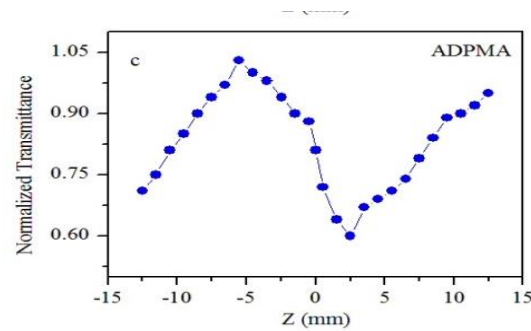
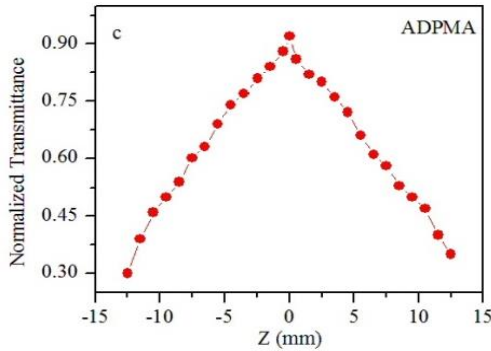


Fig.6 . Z-scan –open aperture

Fig.7. Z-scan- closed aperture

3.4. VICKER'S MICROHARDNESS TEST

Mechanical strength of the material plays a key role in the device fabrication. According to Jianghong Gong et al, during an indentation process, the external work applied by the indenter is converted to a strain energy component which is proportional to the volume of resultant impression. The hardness of a material is influenced by various parameters such as the lattice energy, Debye temperature, heat of formation and interatomic spacing.

The Vicker's hardness indentations were made on the cut and polished samples and load was varied as 25g, 50g and 100g and the corresponding diagonal length of the indentation mark was measured using Vicker's diamond indenter and attached to an incident light microscope. The indentation time was kept at 5s for all loads. The Vicker's hardness number was calculated using the relation

$$H_v = 1.8544 P/d^2 \text{ Kg}/\text{mm}^2$$

Where H_v is Vicker's microhardness number, P is the applied load in Kg., d is the diagonal length of the indentation in mm. The variation of H_v with load P is shown in fig.8.

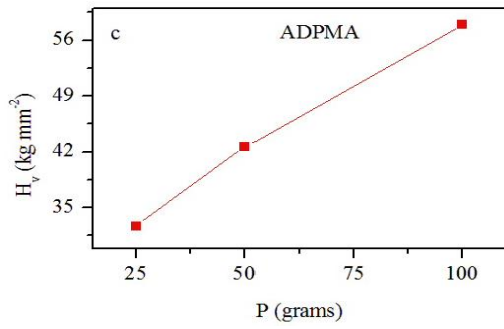


Fig.8. Dependence of H_v with load

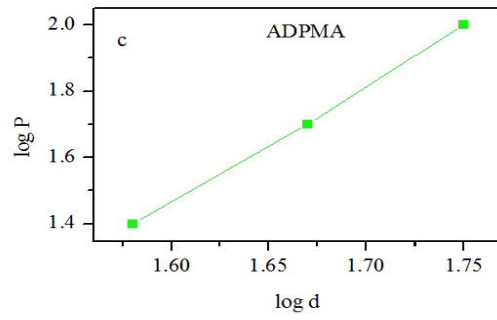


Fig.9. Relation between $\log P$ and $\log d$

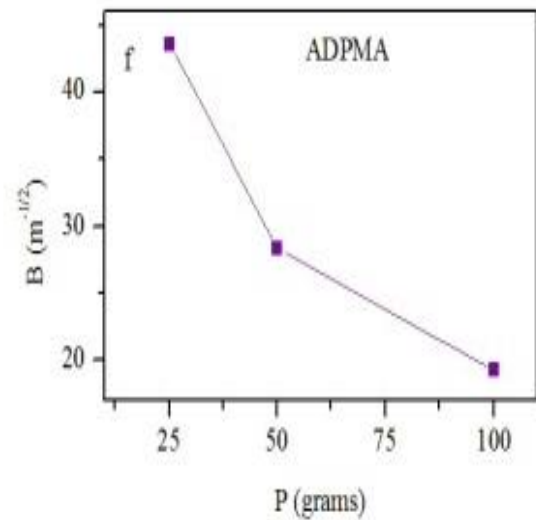
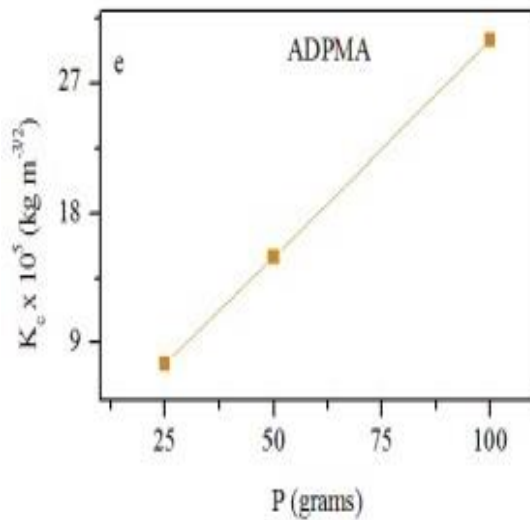
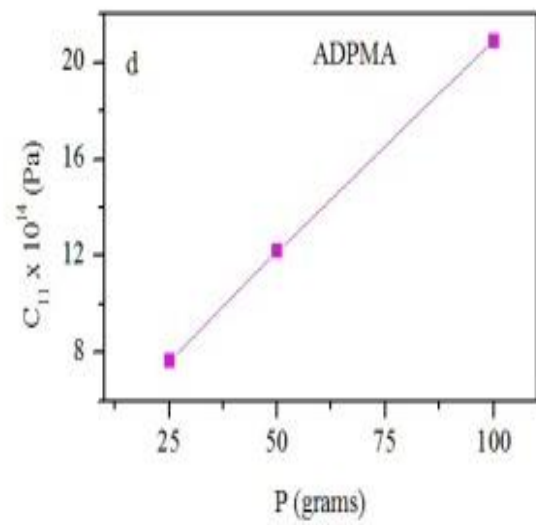
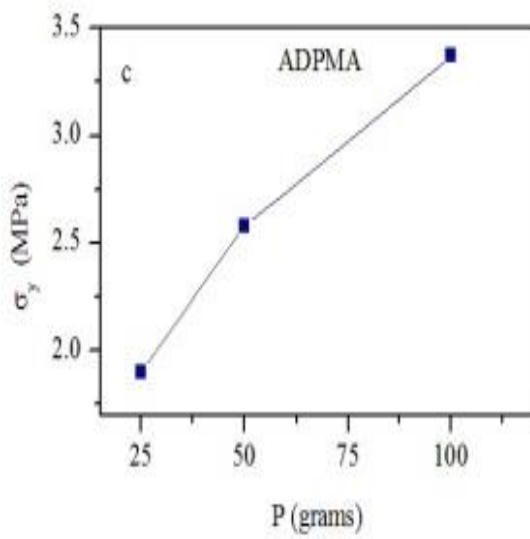


Fig.10 . Dependence of various mechanical parameters with load

It is evident from the plot that the hardness of the sample increases with load. The plot between $\log P$ and $\log d$ is a straight line and the slope of the line gives the work hardening index which is found to be $n = 3.75$ [10]. Fig.9. Hence this crystal belongs to the category of soft materials.

The yield strength (σ_y), elastic stiffness constant (C_{11}), fracture toughness (K_c) and brittleness Constant (B) are calculated and given in table 3 as below.

Table 3. Mechanical Parameters of the grown crystal

Load (P) g	Yield strength (σ_y) MPa	Elastic stiffness constant (C_{11}) 10^{14} Pa	Fracture toughness coefficient (K_c) 10^5 $\text{kgm}^{-3/2}$	Brittleness index (B) $\text{m}^{-1/2}$
25	1.9	7.675	7.502	43.588
50	2.475	12.193	15.003	28.394
100	3.366	20.892	30.006	19.313

SHG ANALYSIS

Nonlinear optical property of the grown crystal was analyzed with Kurtz-Perry powder method and its efficiency was compared with KDP and urea. Second harmonic radiation generated by the randomly oriented micro crystals was focused by a lens and detected by a photomultiplier tube after filtration of the incident radiation of wavelength 1064 nm. The doubling of frequency was confirmed by the emission of the green colour output radiation whose characteristic wavelength is 532 nm. The relative measured output from the specimen with respect to KDP crystals shows that the SHG efficiency of the crystal is 1.032 times higher than that of KDP crystals.

Conclusion

DL-malic acid doped ADP single crystals were successfully grown using slow evaporation solution growth method. The functional groups present in the grown crystals were elucidated using FTIR spectroscopy. The wider bandgap of the material, significant transmittance and uniformity of refractive index in the entire visible region make the candidate ideal for device



fabrication. Moreover, the crystal has self focusing nature and two photon absorption process as inferred from Z- scan technique. The mechanical strength of the crystal is also sufficient to withstand the processes involved in device fabrication.

Acknowledgement

The authors are grateful to Prof. Sastikumar, NIT, Trichy for Z-scan analysis, Dr.P.K.Dhas, IISc, Bangalore for NLO-SHG studies and St.Joseph's College, Trichy for microhardness studies.

Reference

1. M.E. Lines, A.M. Glass, *Principles and applications of Ferroelectrics and related materials*, Clarendon Press,Oxford,1977
2. N.G. Parsonage, L.A.K. Stavelly, *Disorder in Crystals*, Clarendon Press,1978
3. L. Tenzer,B.C. Frazer, R. Pepinsky, *A neutron structure analysis of tetragonal NH₄ H₂PO₄ single crystals*, Acta Crys.11(1958)505
4. P. Rajesh, P. Ramasamy, *Growth of DL-malic acid doped ADP crystals and its characterization*, Jour.Crys,Grow.311,(2009)3491-3497
5. Briyan C.Smith, *IR spectral interpretation, A systematic approach*-CRC Press (1999) New York
6. Dhanaraj et al, *Effect of amino acid additives on crystal growth parameters and properties of ADP crystals*,Mate.Chem.Phy,112,(2008)490
7. M. Senthil Pandian et al, *Growth of TGS single crystals by conventional and SR method and its analysis on the basis of mechanical, thermal, optical and etching studies*,Mat.Lett.62(2008)3830
8. R. DeSalvo, N. Sheik-Bahae et al, *Z-scan measurements of the anisotropy of nonlinear refraction and absorption in crystals*, Optics Letters,Vol.18,no.3,194-196
9. M. Krishnakumar et al, *Studies on the structural and third order nonlinear optical properties of solution grown 4-hydroxy-3 methoxy-4'-N'-methylstilbazolium tosylate monohydrate crystals*, Optical materials,Vol.36,no.5,988-995,2014
10. E.M.Onitch, *The present status of testing hardness of materials*, Microscope, 95, 12-14, 1950





THERMAL AND DIELECTRIC PROPERTIES OF DL-MALIC ACID DOPED ADP NLO SINGLE CRYSTALS

A.Roselin¹, A. Sumathi¹, A. Effie Cordelia¹ and S. Perumal²

¹Department of Physics, Sarah Tucker College, Tirunelveli, India

²Physics Research Centre, Nagercoil, Tamilnadu, India

Abstract

DL-malic acid doped ADP nonlinear optic single crystals were grown by solution method. The thermal stability and the dielectric properties of the crystals were studied. Good thermal stability and low dielectric loss of the crystals enable them as better candidates for opto electronic device fabrication.

Keywords: Slow evaporation solution growth method, TG-DTA, AC conductivity, activation energy

Introduction

Ammonium Dihydrogen Phosphate, which is an important isomorph of Potassium Dihydrogen Phosphate crystal, has been widely used for frequency conversion in laser systems, optical switches and acousto-optical devices. This hydrogen bonded compound also exhibits piezoelectric activity and low temperature order-disorder phase transition. Below 148.5 K, ADP is ferroelectric and belongs to $P2_12_12_1$ space symmetry group while above this temperature, it is paraelectric having $I4/2d$ symmetry. This is also nonlinear optical material having applications in the field of photonics for frequency mixing, parametric amplification and electro optic modulation. DL-malic acid is a dicarboxylic acid which is chosen to be doped with ADP. Because of this attempt, the SHG efficiency of ADP is found to increase so that we arrive at better advantage of using these doped crystals ADPMA in photonics and related fields. These newly grown single crystals are found to possess second harmonic generation efficiency greater

than ADP. To avail the maximum usage of these crystals, the thermal and dielectric properties of these crystals were analyzed by the corresponding characterization tools and presented in this paper.

Method of crystal growth

Analar Reagent (AR) grade chemicals Ammonium Dihydrogen Orthophosphate (ADP) and DL-malic acid were purchased commercially. To obtain DL-malic acid doped ADP single crystal ADPMA, 2 mole % of DL-malic acid along with the calculated amount of ADP were dissolved in double distilled water. The solution was stirred well using a magnetic stirrer for three hours and filtered. The solution was kept undisturbed in dust free atmosphere till transparent colourless nonlinear optical single crystals ADPMA were harvested. The photographs of the crystals are shown in fig 1.

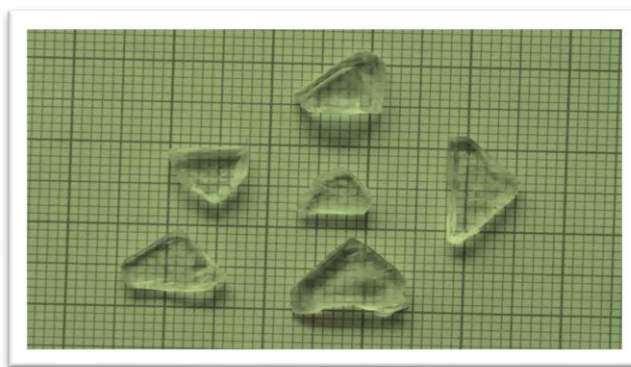


Fig.1. Photograph of the grown crystal ADPMA

Results and Discussion

Single crystal X-ray diffraction analysis

The unit cell parameters and crystalline system of these three crystals ADPMA were found out using BRUKER- NONIUS MACH3 /CAD4 single crystal X-ray diffractometer and tabulated in table 1.

Table 1 Cell parameter values of ADPMA single crystals

Sample	System	a(Å)	b(Å)	c(Å)	V(Å) ³
ADPMA	Tetragonal	7.525	7.525	7.573	429

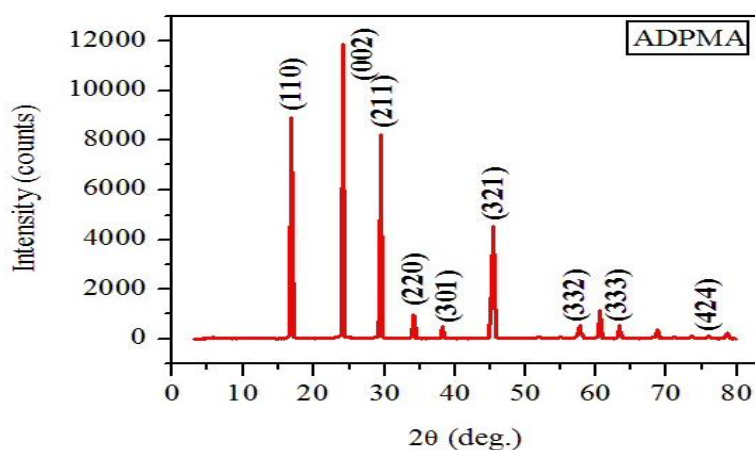


In ADPMA, the system in which the material crystallizes remains the same which is tetragonal. The lattice parameters vary a little and there is a small change noticed in the volume of the unit cell.

Powder X-ray diffraction analysis

The harvested crystals ADPMA were ground into fine powder and the powder X-ray diffractions were recorded using X-ray diffractometer using BRUKER AXS D8 advance diffractometer with $\text{CuK}\alpha$ ($\lambda=1.5418 \text{ \AA}$) radiation. The sample was scanned over the range $0-80^\circ$ at the rate of 2 per minute. The crystalline phase structure of the samples was identified from the crystallographic parameters such as 2θ , d-spacing, relative intensity and hkl values.

From the patterns 2θ values were read directly and the relative intensity of the diffraction peaks can be estimated. The d-spacings corresponding to different peak positions were calculated using Bragg's law $2d\sin\theta = n\lambda$ where d is the interplanar spacing, θ is the angle of diffraction, n is the order of diffraction and λ is the wavelength of X-rays used. The peaks were indexed using the procedures of Lipson and Steeple. The powder X-ray diffraction spectra for the crystals ADPMA are plotted in fig. 2.



FTIR spectral analysis

The Fourier Transform Infrared spectral analysis has been carried out to understand the chemical bonding and it provides useful information regarding the molecular structure of the compound. The spectrum was recorded with Perkin Elmer FTIR spectrometer in $400-4000 \text{ cm}^{-1}$ range using KBr pellet technique. Infrared absorption studies involve examination of stretching, bending, twisting, rotating and vibrational modes of atoms in a molecule and hence to identified

the functional groups of the samples. FTIR spectrum is interpreted using known group frequencies and thus it is easier to characterize the substance.

The FTIR Spectra of the crystals ADPMA are given in fig.3 and the corresponding spectral assignments are displayed in table 2.

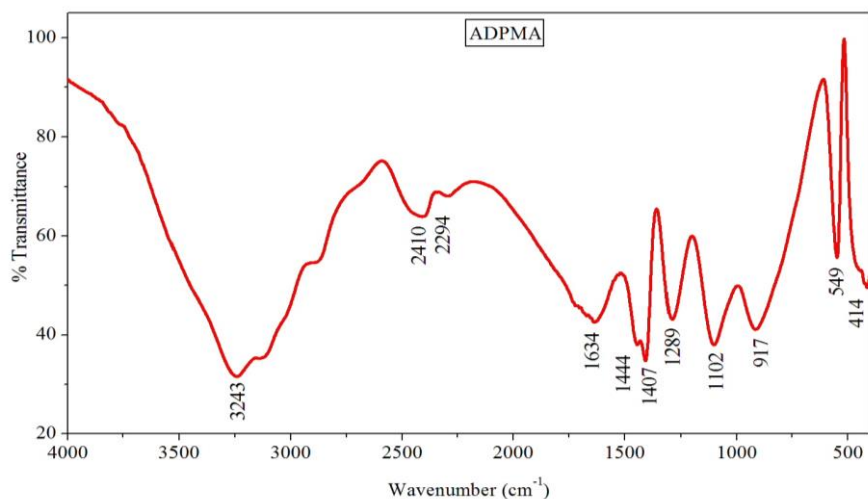


Fig.3.FTIR spectrum of ADPMA

Table 2 Spectral assignments for ADPMA

ADPMA	
Wave number cm^{-1}	Assignments
3243	O-H stretching, P-O-H stretching , N-H vibrations of ammonium
2410	band due to hydrogen bond
2294	combination band
1634	O-H bending of water
1444	H-H bending of NH_4
1407	bending vibrations of ammonium
1289	CH_2 rocking vibration
1102	P-O-H vibrations
917	P-O-H vibrations
549	PO_4 vibrations
414	PO_4 vibrations

Thermal analysis

Studies of thermogravimetric and differential thermal analysis (TG-DTA) were carried out to check the thermal stability and to identify various endothermic and exothermic transitions. The thermal curves of the grown crystals ADPMA are given in fig.4.

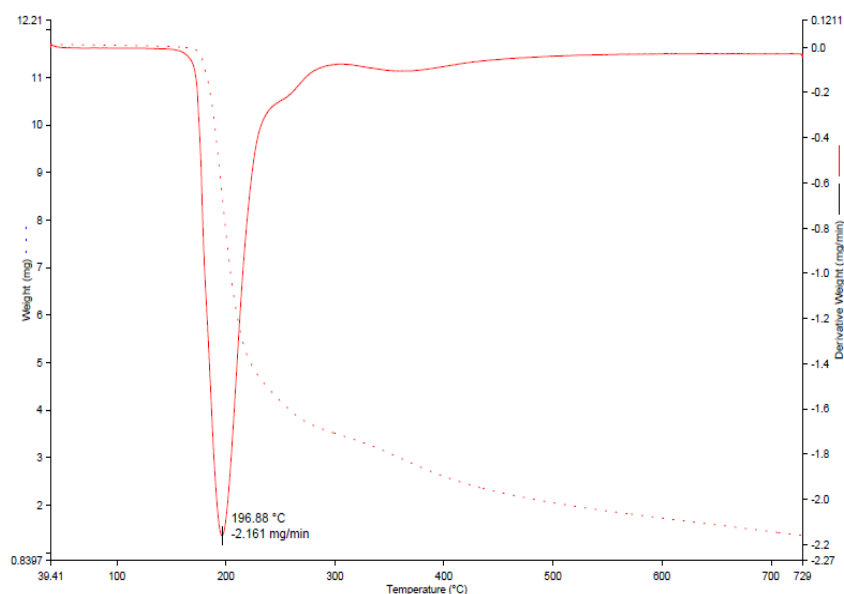


Fig.4. TG-DTA thermogram for the crystal ADPMA

In ADPMA, the crystal is found to be thermally stable upto 196.88 °C and the crystal melts at 196.88 °C. No other endothermic and exothermic peak seen from DTA curve of the crystal. In TGA, there is weight loss of 51.3 % of the sample between 180 °C and 230 °C. In between 280 °C and 600 °C, a weight loss of 33.3 % is observed.

Dielectric studies

The dielectric properties of the crystals ADPMA were determined using Agilent (4284A) Precision LCR meter. The experiment was conducted at various temperatures from 40 °C to 140 °C over a frequency range 100 Hz to 1 MHz. The variation of dielectric constant with frequency at different temperatures is shown in fig. 5. The variation of dielectric loss with frequency at different temperatures is shown in fig.6. Similarly these two dielectric parameters have the variation with temperature at different frequencies and these are plotted in fig. 7 and fig.8. All these crystals have similar behavior in which dielectric constant decreases with frequency and

increases with temperature. As the crystals have low dielectric loss at high frequencies, they are found to possess enhanced optical quality with less defects. This is a required vital parameter for the NLO materials in the fields of various applications.

It is observed that AC conductivity of the crystals increases with temperature and activation energies are calculated at frequency 1 kHz for all the three crystals. The values are tabulated in table 5.

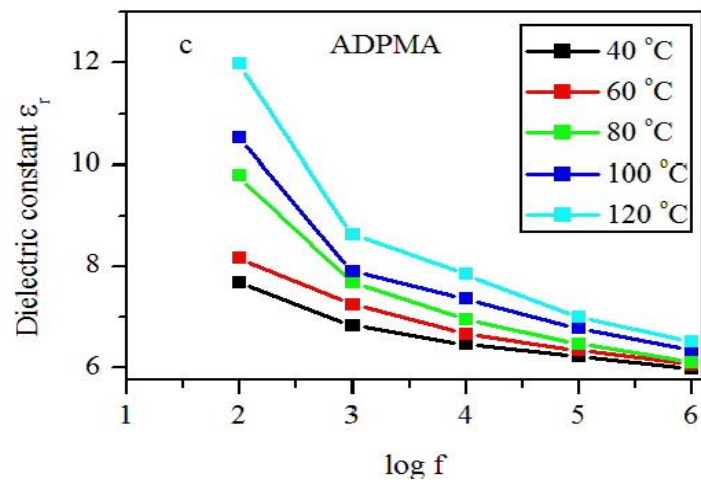


Fig.5. Dielectric constant versus frequency of the applied field at different temperatures

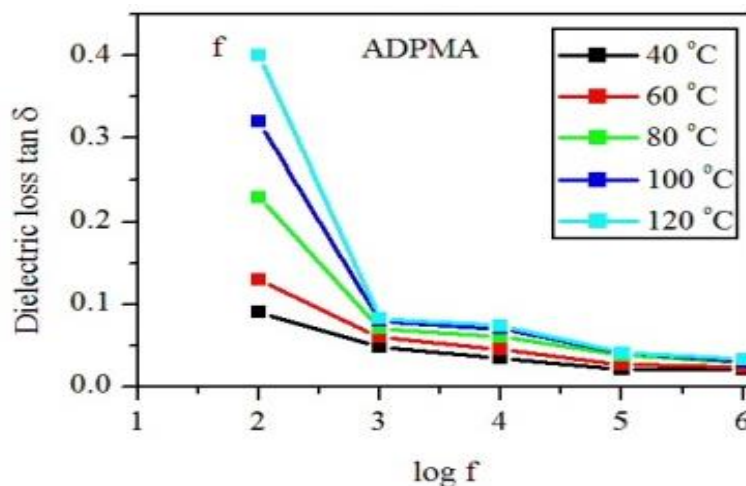


Fig.6. Dielectric loss versus frequency of the applied field at different temperatures

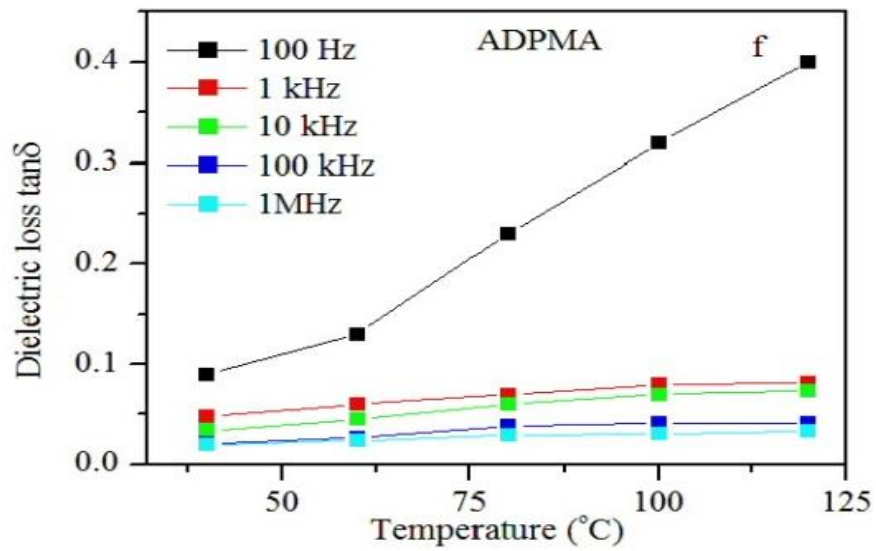


Fig.7. Dielectric constant versus temperature at different frequencies

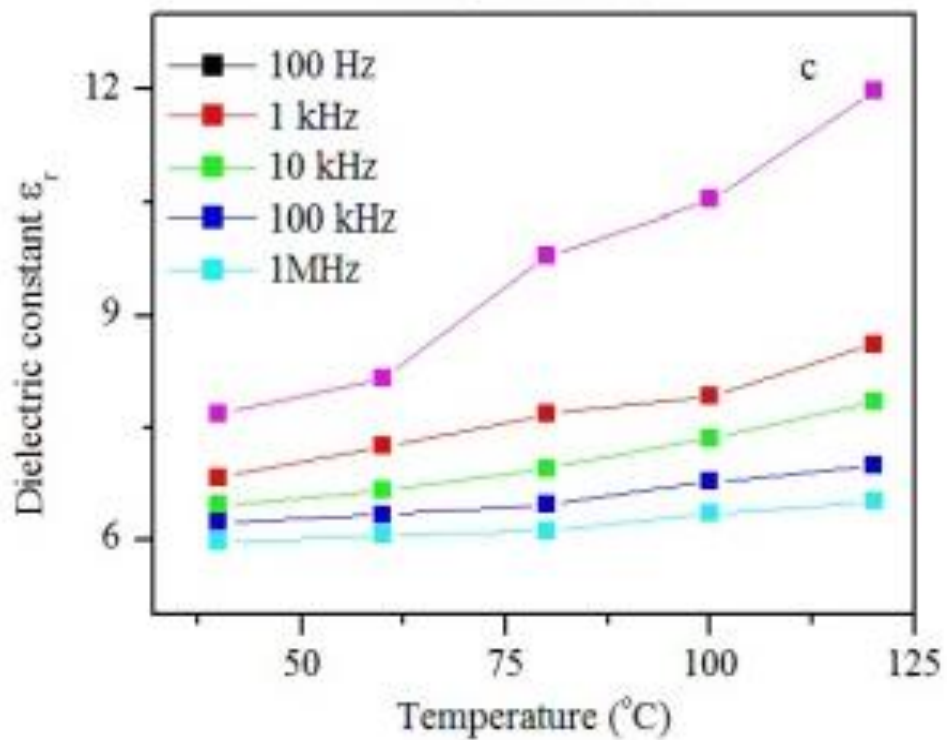


Fig.8. Dielectric loss versus temperature at different frequencies

Table 3 Dielectric parameters of ADPMA crystals

Sample	Frequency Hz	Dielectric Constant ϵ_r					Dielectric Loss $\tan\delta$				
		40°C	60°C	80°C	100°C	120°C	40°C	60°C	80°C	100°C	120°C
ADPMA	10 ²	7.68	8.16	9.79	10.53	11.98	0.09	0.13	0.23	0.32	0.4
	10 ³	6.83	7.25	7.68	7.91	8.62	0.048	0.06	0.07	0.08	0.082
	10 ⁴	6.46	6.66	6.95	7.36	7.84	0.034	0.045	0.06	0.07	0.074
	10 ⁵	6.23	6.34	6.47	6.77	6.99	0.021	0.027	0.038	0.041	0.041
	10 ⁶	5.97	6.06	6.11	6.35	6.51	0.02	0.024	0.029	0.031	0.033

The values of AC conductivity of the crystals ADPMA were calculated at different frequencies and temperatures and listed in table 3. The corresponding curves are plotted in fig. 9. Activation energy for the three grown crystals at frequency 1 kHz is calculated using fig.10 and shown in table 5.

Table 4 Variation of ac conductivity of the crystals ADPMA with frequency and temperature

Sample	Frequency (Hz)	$\sigma_{ac} \times 10^{-6} (\Omega m)^{-1}$				
		40° C	60° C	80° C	100° C	120° C
ADPMA	10 ²	0.00384	0.006	0.0125	0.0187	0.027
	10 ³	0.0182	0.024	0.03	0.0352	0.0393
	10 ⁴	0.022	0.246	0.0332	0.0286	0.0422
	10 ⁵	0.727	0.951	1.366	1.543	1.593
	10 ⁶	6.636	8.083	9.848	10.941	11.94

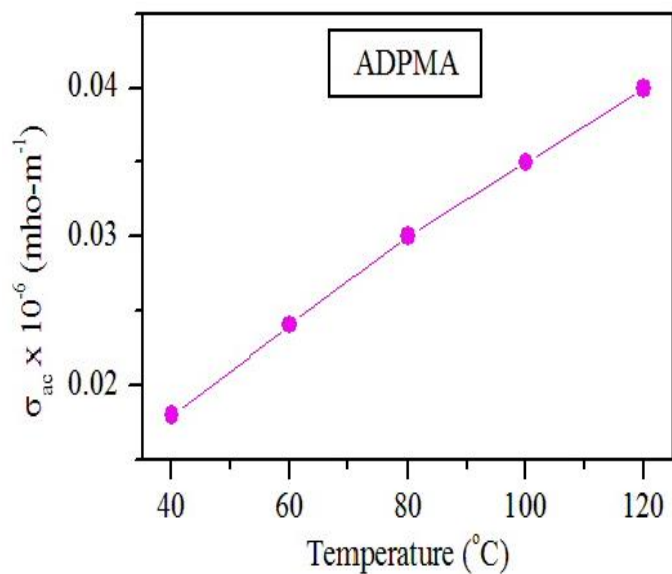


Fig. 9 Variation of AC conductivity with temperature

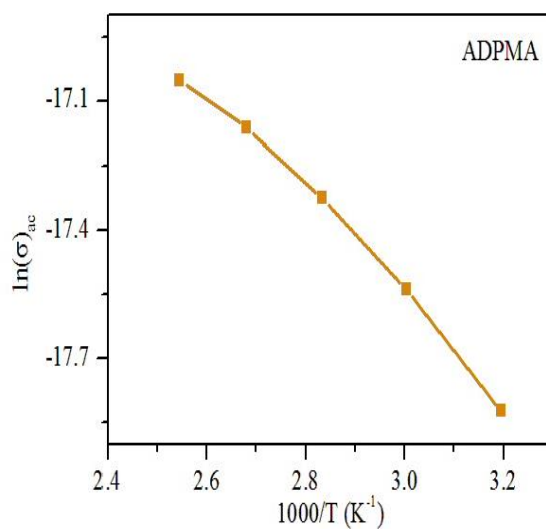


Fig.10 Graph drawn to calculate activation energy of the crystals

Table 5 Activation energy of the crystals at frequency 1 kHz

Sample	E _{ac} eV
ADPMA	0.1032

Conclusion

Novel NLO single crystal ADPMA were grown successfully using slow evaporation solution growth method. The crystalline nature and lattice parameters were found out using single crystal XRD analysis. Powder XRD pattern of the crystals were obtained and the reflecting planes were indexed. The possible functional groups present in the crystals were determined from FTIR spectra. The hardness studies revealed the mechanical strength of the crystals. Thermal stability of the sample was checked using TG-DTA analysis. Dielectric parameters were calculated and AC conductivity and activation energy of the crystals were estimated from dielectric studies.

Reference

1. M.E. Lines, A.M. Glass, *Principles and applications of Ferroelectrics and related materials*, Clarendon Press, Oxford, 1977
2. N.G. Parsonage, L.A.K. Stavelly, *Disorder in Crystals*, Clarendon Press, 1978
3. L. Tenzer, B.C. Frazer, R. Pepinsky, *A neutron structure analysis of tetragonal $NH_4 H_2PO_4$ single crystals*, Acta Crys.11 (1958) 505
4. P. Rajesh, P. Ramasamy, *Growth of DL-malic acid doped ADP crystals and its characterization*, Jour.Crys. Grow.311, (2009) 3491-3497
5. Briyan C. Smith, *IR spectral interpretation, A systematic approach* - CRC Press (1999) New York
6. Dhanaraj et al, *Effect of amino acid additives on crystal growth parameters and properties of ADP crystals*, Mate.Chem.Phy .112, (2008) 490
7. M. Senthil Pandian et al, *Growth of TGS single crystals by conventional and SR method and its analysis on the basis of mechanical, thermal, optical and etching studies*, Mat.Lett. 62 (2008) 3830
8. M. Krishnakumar et al, *Studies on the structural and third order nonlinear optical properties of solution grown 4-hydroxy-3 methoxy-4'-N'-methylstilbazolium tosylate monohydrate crystals*, Optical materials, .36(5), 988-995, 2014



Volume: 2; Issue: 3 [Special Issue]; March-2016; pp 497-502. ISSN: 2454-5422

Solvothermal Synthesis and Characterization of Manganese Doped Copper Oxide Flower Like Nanostructures

A.Suganthi*¹, S.John Kennady Vethanathan², S.Perumal³, D.Priscilla Koilpillai⁴ and S.Karpagavalli⁵

*^{1&5}Govindammal Adithanar College for Women, Tiruchendur, India.

^{2&4} St. John's College, Palayamkottai, India.

³ Principal, S.T.Hindu college, Nagercoil, India.

Abstract

Manganese doped Copper oxide nanoparticles are synthesized by a microwave assisted solvothermal method using Copper acetate as precursor. This gives a large scale production of Copper oxide nanoparticles. X-ray diffraction pattern reveals cubic structure. The morphology of the sample is examined by Scanning electron microscopy technique. The functional group and other impurities present in the material are interpreted by FTIR. The optical property of manganese doped copper oxide nanoparticles are analyzed by UV-Visible spectroscopy.

Key words: Solvothermal, Nanoparticles

Introduction

In recent years, controlled synthesis of inorganic materials with well defined morphologies has attracted considerable interest since the morphological diversity of inorganic materials has a significant impact on their functional diversification and potential applications. Copper oxide is a P-type semiconductor oxide that is being widely studied due to its interesting properties and applications. It has potential applications in solar cells, Catalysis, electrode material, magnetic storage media and lithium ion batteries. Copper oxide nanoparticles have been prepared by several methods ranging from thermal reduction, sonochemical method and solid state reaction to gas phase process. Among those, solvothermal process has been shown to be a powerful technique for generating novel materials with interesting properties particularly the solvothermal technique provides the alternative approach that allows the economical



synthesis of fundamentally important cell defined nanometer sized materials at mild conditions. The present work is focused on the synthesis and characterization of nano meter sized manganese doped copper oxide nanoparticle by a simple microwave assisted solvothermal method.

Materials and Methods

Copper (II) acetate monohydrate, urea, ethylene glycol (solvent), Manganese (II) acetate tetra hydrate are used as precursors. Copper acetate and urea are taken in the molecular ratio 1:3 and dissolved in 100ml ethylene glycol as individually. Manganese acetate is also dissolved in ethylene glycol. The solutions are mixed together. The solution is kept in a domestic microwave oven. Microwave irradiation is carried out for 20 minutes till the solvent is evaporated completely. Colloidal precipitate is obtained. The precipitate is washed several times with distilled water and acetone to remove organic impurities. The prepared sample is dried in atmospheric air.

Results

XRD analysis

The XRD pattern which is obtained in the present study for Mn doped Copper oxide nanoparticles is shown in fig.1. All diffraction peaks can be indexed in the Cu₂O cubic structure, Which was confirmed from the JCPDS 78-2076. The planes (110), (111), (200), (220), (311) and (222) are corresponding to Cu₂O. The planes (002), (100), (101), (004) and (110) are corresponding to Mn. No peaks of impurities are found in XRD pattern.

The average crystallite size was estimated using Debye Scherrer's equation ;

$$D = k \lambda / \beta \cos \theta, \text{ where } K - \text{Scherrer constant, } \lambda - \text{Wavelength of the X-ray source (1.5406 \text{ \AA}^0)$$

and β –

Full width half maximum (FWHM) of a diffraction peak

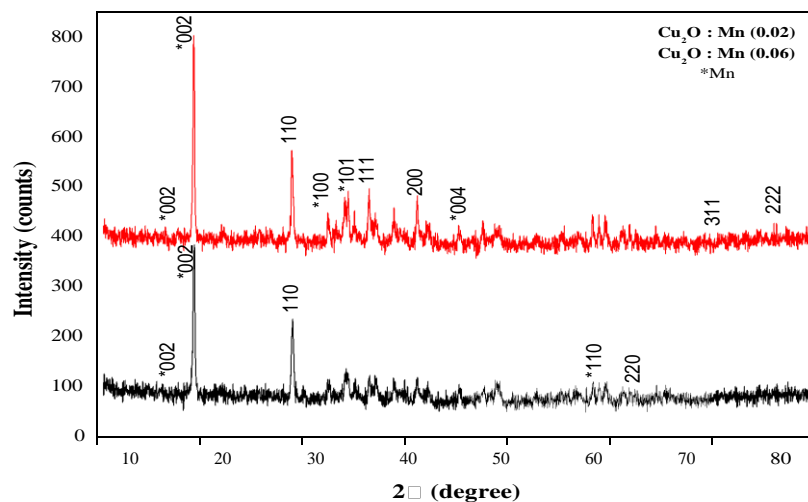


Fig 1: XRD spectrum of Mn doped Cu₂O nanoparticle

FTIR analysis

The FTIR analysis is performed by SHIMADZU MODEL-IRAFFINITY-1. The peak at 3500 cm^{-1} and 1624 cm^{-1} represents (O-H) water tensional tremble. The peak at 2362 cm^{-1} is attributed to C-H tensional .The peak at 1458 cm^{-1} and 1384 cm^{-1} represents (N-O) and (C-O) tremble respectively. The peak at 986 cm^{-1} represents (O-C-O) tensional tremble and 608 cm^{-1} reveals the dopant Mn-O tremble respectively.

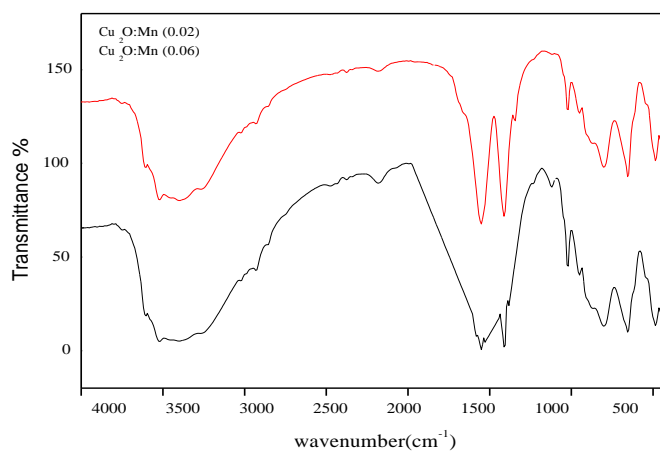


Fig 2: FTIR spectra of Mn doped Cu₂O nanoparticles

SEM Analysis

In order to obtain insight information about surface morphology and particle size of the samples, SEM analyses were performed.

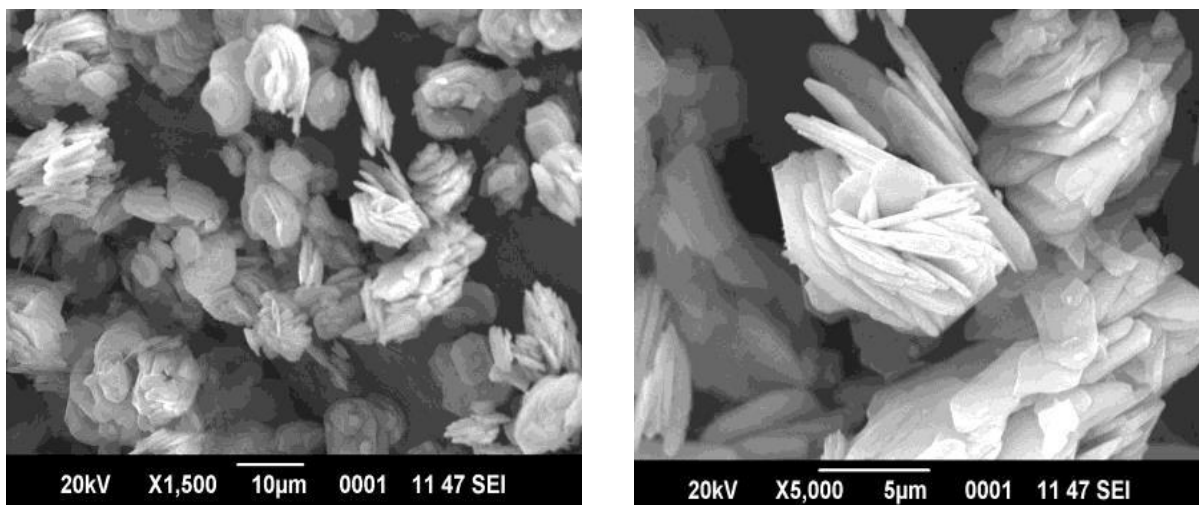


Fig.3. SEM image Cu₂O: Mn (0.02g)

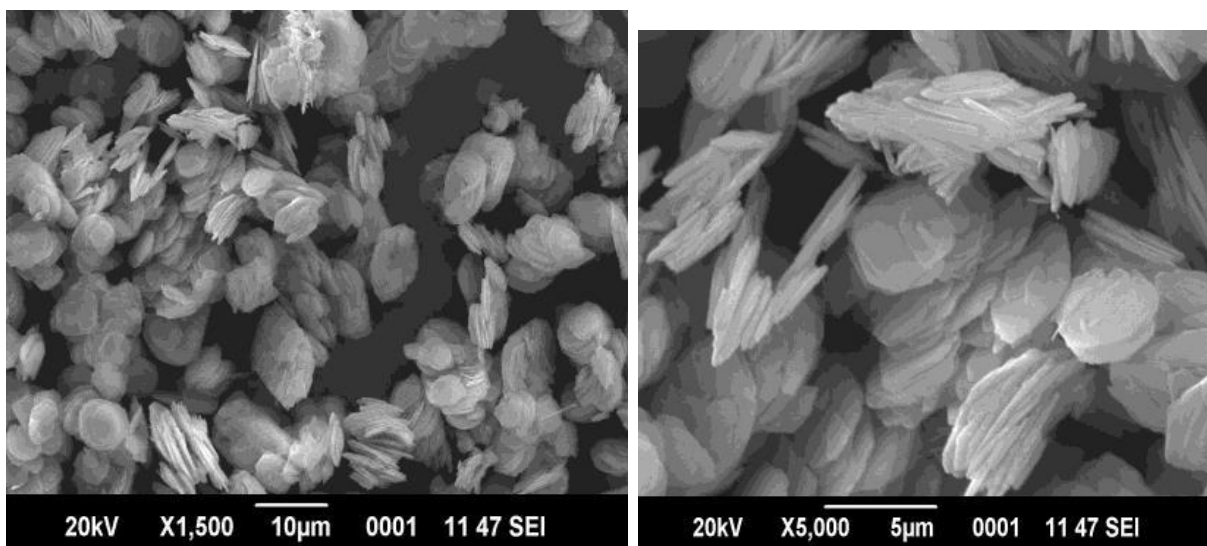


Fig 4 SEM image Cu₂O: Mn (0.06g)

SEM image reveals that Mn doped Copper oxide nanoparticles exhibit rose flower like structure and the average size of the image is found out using Image J software.

UV –Visible analysis

UV-Visible absorption spectroscopy has been used to investigate the optical properties of Mn doped copper oxide nanoparticles. The absorption spectra of Mn doped Cu₂O nanoparticles is shown in Fig.5. It has been observed that the samples exhibit an absorption edge around 294nm & 283nm respectively. The energy band gaps are 4.23eV & 4.39eV.

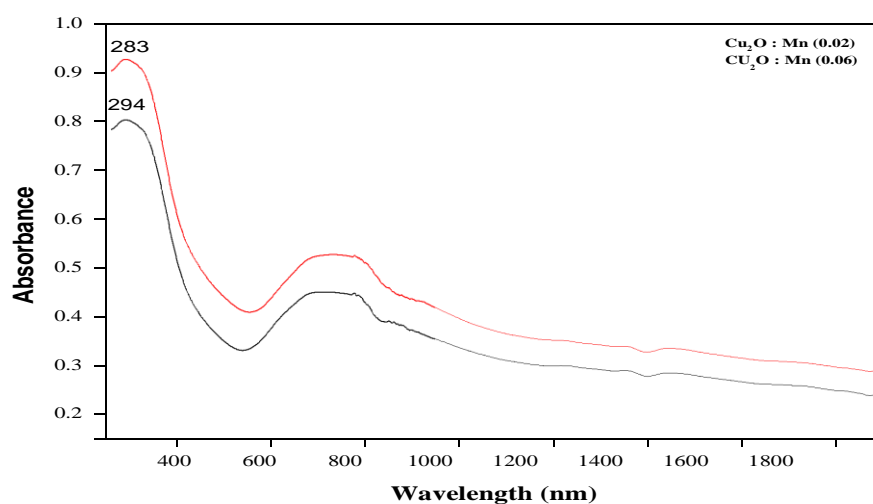


Fig.5. Absorbance spectra of Mn doped Cu₂O nanoparticles

Discussion

Mn doped Cu₂O nanoparticles are synthesized by microwave assisted solvothermal method. The XRD result gives a cubic structure with lattice parameters $a=b=c=4.267 \text{ \AA}$. The average size of Mn (2 wt% & 6wt %) doped Cu₂O nanoparticles are found to be 39nm and 33nm respectively. The average crystallite size from XRD is very agreed with SEM confirmation. FTIR spectrum analysis gives the brief investigation of functional groups. UV-VISIBLE absorbance spectrum reveals blue shift in case of higher Mn doping concentration. This shift towards lower wavelength could be attributed to the quantum confinement effect of nanoparticles.

Acknowledgement



I state my deep sense of devotion to my guide Dr.S.John Kennady Vethanathan for his precious ideas, outstanding guidance and constant source of inspiration at every stage of this work. I thank my family members and friends who rendered direct and indirect help.

References

K. Sanfra, C.K. Sarkar, M.K. Mukherjee, B. Cosh, *Thin Solid Films* 213 (1992) 226. D.M. Fernandes, R. Silva, A.A.W. Hechenleitner, E. Radovanovic, M.A.C. Melo, E.A.G. Pineda, *Mater. Chem. Phys.* 115 (2009) 110-115.

S.C. Ray, *Sol. Energy Mater. Sol. Cells* 68(2001) 307.

Z. Zhong, V. Ng, J. Luo, S.P. Teh, J. Teo and A. Gedanken, *Langmuir* 23 (2007) 5971.

M. Arumugam, N. Selvaraj, S. Kumar, P. Selvam and A. Sambandam, *Sci. Adv. Mater.* 2 (2010) 51.

J.F. Deng, Q. Sun, Y.L. Zhang, S.Y. Chen and D. Wu, *Appl. Catal. A* 139 (1996) 75.

M. Frietsch, F. Zudock, J. Goschnick and M. Bruns, *Sensors Actuators B* 65 (2002) 379.

P. Poizot, S. Laruelle, S. Grugeon, L. Supont and J.M. Taracon, *Nature* 407 (2000) 496.

D.P. Singh and N. Ali, *Sci. Adv. Mater.* 2 (2010) 295.

C. B. McAuley, Y. Du, G. G. Wildgoose and R.G. Compton, *Sensors Actuators B* 135 (2008)230.





OPTICAL AND STRUCTURAL CHARACTERIZATION OF COBALT DOPED MANGANESE OXIDE NANOPARTICLES

S. Karpagavalli*¹, S. John Kennady Vethanathan², S. Perumal³, D. Priscilla Koilpillai⁴
and A. Suganthi⁵

*¹Govindammal Adithanar College for Women, Tiruchendur, India.

^{2&4} St. John's College, Palayamkottai, India.

³Principal, S.T.Hindu College, Nagercoil, India.

⁵Govindammal Adithanar College for Women, Tiruchendur, India.

*Corresponding Author Email Id: karthikabharthi@gmail.com

ABSTRACT Cobalt doped manganese oxide nano particles have been synthesized by solvothermal route. The structural properties were analyzed by X-ray diffraction (XRD). The particle size was calculated from XRD data by using Scherrer equation and is confirmed by Scanning electron microscope (SEM) analysis. The SEM image shows that the nanoclusters having spherical geometry. The optical properties were analyzed by Ultraviolet–Visible (UV-Vis) spectroscopy. UV-Vis spectra illustrates that Cobalt doped Manganese oxide nano particles acquire blue shift from the bulk value (2.5 eV). The functional groups present in the material were interpreted by Fourier transform infrared (FTIR) spectral analysis. Manganese oxide nano particles have many applications in the near future by virtue of its magnetic properties and catalytic properties. Manganese oxide is environmental friendly in nature. Due to good electro mechanical performance, it is a good electrode material for super capacitors and batteries.

Keywords: Cobalt doped MnO₂ nanoparticles, Solvothermal route, XRD, SEM and UV-Vis

Introduction: A nano structured material is defined as a solid material characterized by at least one dimension in the nanometer range. The inorganic nano materials such as quantum dots,



nanowires and nano rods are made from metals, semiconductors or oxides are of particular interest for their mechanical, magnetic, optical, chemical and other properties. It is widely used as catalyst. Compared to bulk active electrode materials, the corresponding nanomaterials possess higher capacities, larger surface area, and lower current densities. Solvothermal synthesis is relatively new and interesting technique for the synthesis of oxide materials. Various nanomaterials have been synthesized in remarkably short time under microwave irradiation. Microwave techniques eliminate the use of high temperature calcination for extended periods of time and allow for fast, reproducible synthesis of crystalline metal oxide nano particles.

In the present investigation we report the synthesis of Cobalt doped Manganese oxide nanoparticles by microwave-assisted solvothermal method and characterized by powder X-ray diffraction, morphology is examined by Scanning electron microscope, the functional groups and other impurities present in the material were interpreted by Fourier transform infrared spectral analysis and the optical properties were analyzed by ultraviolet - visible spectroscopy.

Materials and Methods: AR grade Manganese II acetate tetra hydrate $(\text{CH}_3\text{COO})_2\text{Mn}\cdot 4\text{H}_2\text{O}$, Urea NH_2CONH_2 (catalyst) and Cobalt II acetate tetra hydrate $(\text{CH}_3\text{COO})_2\text{Co}\cdot 4\text{H}_2\text{O}$ were used as starting materials. The calculated amounts of Manganese II acetate tetra hydrate and urea were taken in the molecular ratio 1:3 and dissolved in 100ml ethylene glycol separately. Cobalt II acetate tetra hydrate (2wt% and 6wt %) were taken along with the precursors. The solution was stirred well and the completely dissolved solution was kept in a microwave oven. The microwave irradiation was carried out till solvent evaporated completely. The prepared samples were washed several times with double distilled water and then with acetone (to remove organic impurities) the washed samples were dried in atmospheric air and were used for characterization studies.

Results: X-Ray diffraction analysis: The crystal structure and phase purity of the samples are analyzed by Bruker AXS D8 Advance model diffractometer. Fig 1 shows the X-ray diffraction pattern of Cobalt doped MnO_2 nano system with different dopant concentration (2% and 6%). All the diffraction peaks are well indexed to the orthorhombic structure with lattice constants of $a = 9.3720 \text{ \AA}$, $b = 2.8508 \text{ \AA}$, $c = 4.4706 \text{ \AA}$ and $\alpha = \beta = \gamma = 90^\circ$.

The crystallite size was estimated using Debye Scherrer's equation; $D = k\lambda / \beta \cos\theta$ (m) Where, K – Shape factor ≈ 0.9 , λ – Wavelength of the X-ray source (1.5406 \AA) and β – Full width half



maximum (FWHM) of adiffractionpeak.The crystallite size and lattice parameters are given in table1.

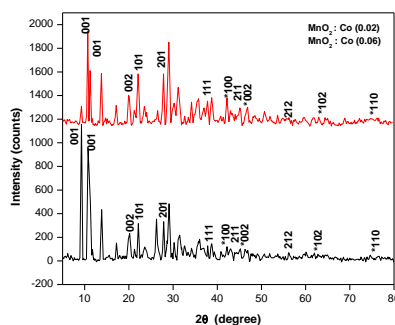


Fig1: XRD pattern of MnO₂:Co nanosystem

Table1: Lattice parameters of MnO₂: Co (0.02 & 0.06) nano particles

Sample	Crystallite size (nm)	Lattice parameter (Å ⁰)		
		a	b	c
MnO ₂ :Co(0.02)	40.0007	9.3720	2.8508	4.4706
MnO ₂ :Co(0.06)	34.2709			

Scanning electron microscope analysis: The morphology of the as-prepared sample was examined by JEOL Model JSM - 6390LV Scanning electron microscope. The SEM images of Cobalt doped MnO₂nanosystem with different dopant concentrations (2% and 6%) are shown in Fig 2a and Fig 2b.

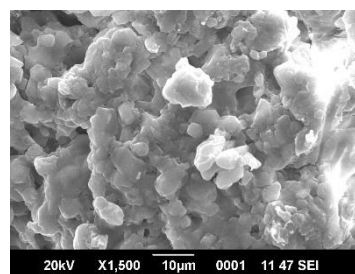
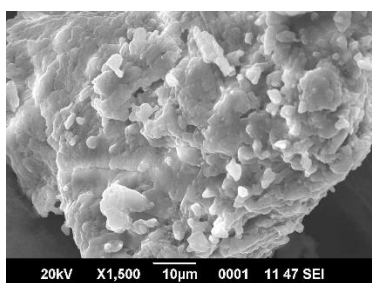


Fig: 2a SEM image MnO₂: Co (0.02)

Fig:2bSEM image MnO₂: Co (0.06)

Fourier transforminfrared spectral analysis: The functional groups and other impurities present in the material were interpreted by SHIMADZU MODEL –IR AFFINITY -1. FTIR spectrum for Cobalt doped MnO₂nano system with dopant concentration (2% and 6%) is presented in Fig3.

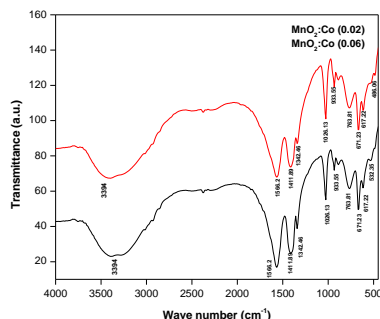


Fig: 3 FTIR spectra of Cobalt doped MnO₂ nano particle

UV-Vis spectroscopy: The optical properties were analyzed by Model Varian, Cary 5000 Ultraviolet –Visible spectrometer. Fig 4 shows the Ultraviolet –Visible absorbance spectra of Cobalt doped MnO₂ nano system with different dopant concentration (2% and 6%). The Ultraviolet –Visible absorption shows peak at 273nm due to Cobalt doped MnO₂ nano particles.

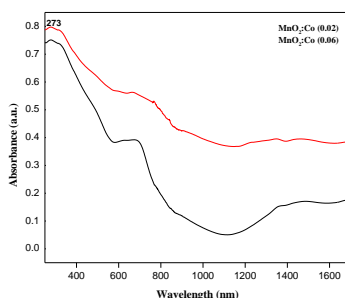


Fig: 4 UV-Vis spectrum of Cobalt doped MnO₂ nano particles

Discussions: The particle size reduces with increase of dopant concentration. The Bragg reflections from (101), (201), (111), (211), (212), (001) and (002) planes which corresponds to MnO₂ (JCPDS 44-0142) and (100), (002), (102), (110) planes represents to Cobalt (JCPDS 05-0727). The crystallite size 30nm to 40nm is very agreed with the SEM by Image J software. The SEM image confirmed the shows that the nanoclusters having spherical geometry. It consists of irregular particles with a variety of pores due to the evolution large amount of gases that are formed as by product during synthesis. Highly porous nature of cobalt doped manganese oxide nano particles enhances the adsorption characteristics. The broad band at 3394.72 cm⁻¹ is associated with the stretching vibrations of hydrogen bonded surface water molecules and hydroxyl groups. 763.81cm⁻¹

¹, 671.23cm⁻¹, 617.22cm⁻¹ represents MnO₂ stretching, bending and wagging vibrations. The band located at 532.35 cm⁻¹ & 401.19cm⁻¹ can be ascribed to the Co-O stretching and wagging. UV-Vis spectra illustrates that Cobalt doped Manganese oxide nano particles acquire blue shift from the bulk of MnO₂ nano particles (ie) 2.5 eV. Energy band gap increases with Cobalt concentration due to the effect of quantum confinement.

Acknowledgement: I would like to express my special thanks of gratitude to my guide Dr.S John Kennedy Vethanathan who gave me the golden opportunity to do this wonderful work on the topic Optical and Structural characterization of Cobalt doped Manganese oxide nanoparticles which also helped me in doing a lot of research. I would also like to thank my family members and friends who helped me a lot in finalizing this paper within the limited time frame.

References:

Toupin M, Brousse T, Belanger D. charge storage mechanism of MnO₂ electrode used in aqueous electro chemical capacitor. *Chem Mater* 2004, **16**: 3184-3190

Belanger D, Brousse T, Long JW. Manganese oxides Battery materials make the leap to electro chemical capacitors. *Electro chem Soc Interface* 2008, **Spring**: 49-52

SONG Rui, WANG Hong-jun and FENG Shou-hua “Solvothermal Preparation of Mn₃O₄ Nano particles and Effect of Temperature on Particle Size” *CHEM.RES.CHINESE UNIVERSITIES* 2012, 28(4), 577-580

Huachunzeng supplementary material (ESI) for journals of Materials chemistry (2010)

BM Pradeepkumar, Sriram Karikkat, R Hari Krishna, TH Udayashankara, KH Shivaprasad and BM Nagabhushana “Synthesis and Characterization of Nano MnO₂ and its adsorption characteristics over an AzoDye. *RES. & REVIEWS: J. MATERIAL SCIENCES* (2013) Volume 2

Harish Kumar, Manisha and Poonam Sangwan “Synthesis and Characterization of MnO₂ nanoparticles using Co-precipitation Technique” *International journal of Chemistry and Chemical Engineering* ISSN 2248-9924 Volume 3, Number 3 (2013), pp.155-160

K.S.Pugazhvadivu, K.Ramachandran and K.Tamilarasan “Synthesis and Characterization of Cobalt doped Manganese oxide nanoparticles by chemical route” *Physics procedia* 49 (2013) 205-216.

